

120

Electronic Structure and Transport Properties of Quantum Dots

Alev Devrim Güçlü
Centre for the Physics of Materials
Department of Physics
McGill University
Montréal, Québec
Canada

A Thesis submitted to the
Faculty of Graduate Studies and Research
in partial fulfillment of the requirements for the degree of
Doctor of Philosophy

© Alev Devrim Güçlü, 2003

150

1 20032

Contents

Acknowledgments	xii
1 Introduction	1
2 Theoretical Foundations	13
2.1 Introduction	13
2.2 Systems of interacting electrons	14
2.2.1 Antisymmetrization of wave functions	15
2.2.2 Second quantization	16
2.3 Exact diagonalization	17
2.3.1 Calculation of two-body interaction terms	18
2.3.2 Calculation of many-body matrix elements	19
2.3.3 Diagonalization	20
2.3.4 Calculation of electronic density	22
2.4 Hartree-Fock approximation	22
2.4.1 Restricted and unrestricted Hartree-Fock	24
2.5 Variational Monte Carlo	25
2.5.1 Metropolis algorithm	26
2.6 Diffusion Monte Carlo	27
2.6.1 Importance sampling and fixed-phase approximation	30
2.6.2 Calculation of expectation values	33
2.6.3 Spin	35
2.6.4 DQMC algorithm	36
2.7 Quantum transport	37
2.7.1 Keldysh Green's function formalism	37
2.7.2 Calculation of current	39
2.7.3 Transport through a N -body system	40
2.7.4 Calculation of spectral function	42
2.7.5 Detailed balance equations	43
2.8 Summary	44
3 Perfectly Parabolic Quantum Dots	47
3.1 Introduction	47
3.2 Fock-Darwin basis set	47
3.3 Results	49
3.3.1 Addition spectrum	49
3.3.2 Spectral function and current-voltage characteristics	51
3.4 Summary	56

4	Ring-Shaped Quantum Dots	57
4.1	Introduction	57
4.2	Model and method	58
4.3	Results	61
4.3.1	Weakly distorted dot	61
4.3.2	Strongly distorted dot	64
4.4	Summary	71
5	Effect of Impurities in Parabolic Quantum Dots	73
5.1	Model and Method	74
5.2	Results and Discussion	77
5.2.1	Energy and addition spectra	77
5.2.2	Hund's rule at zero magnetic field	81
5.2.3	Many-body densities	83
5.3	Summary	85
6	Kondo Effect in a Quantum Dot Molecule	89
6.1	Introduction	89
6.2	Model and method	91
6.3	Calculation of Green's functions	93
6.4	Results	96
6.5	Summary	101
7	Conclusion	103
	Appendices	107
A.1	Two-body interaction terms in Fock-Darwin basis set	107
A.2	Drift velocity and local energy in fixed-phase DQMC	109
A.3	Matrix elements for a Gaussian perturbation in Fock-Darwin basis set	111
A.4	Description of exact diagonalization code	112
A.5	Description of quantum Monte Carlo code	114
A.6	Publications	116
	References	117

List of Figures

1.1	Schematic diagram of a QD located between two capacitor plate. . . .	2
1.2	Schematic diagram of a QD in a gated transport spectroscopy experiment.	3
1.3	Schematic energy diagram of a QD as a function of applied gate voltage.	4
1.4	Addition spectrum of a circular QD, up to 18 electrons, taken from Ref.[10]. Vertical axis represents the chemical potential for a given number of electrons. ν is the filling factor defined as the number of flux lines per electron.	6
2.1	A many-body Hamiltonian with good quantum numbers L and S_z . . .	21
2.2	Schematized Hartree-Fock procedure.	24
2.3	Schematic representation of DQMC process. Density of walkers which are shown by vertical lines, represent the state of the system. Each walker moves according to the Green's function $G(\mathbf{R}\mathbf{R}', \tau)$. Starting from an arbitrary initial state, the result converges to the ground state. Note that \mathbf{R} is a $3N$ dimensional vector.	29
2.4	Comparison of many-body density for a 4 electron QD, $(L, 2S_z) = (3, 2)$, obtained by DQMC and exact diagonalization.	34
2.5	Schematic diagram of the experimental transport configuration. . . .	37
3.1	Fock-Darwin energy spectrum as a function of magnetic field. Different line styles correspond to different Landau levels. Confinement potential strength $\hbar\omega_0$ is fixed to 5 meV.	49
3.2	Addition spectra up to 4 electrons as calculated by exact diagonalization. Confinement potential parabolicity is $\hbar\omega_0 = 5.4$ meV. Numbers in parenthesis represent total angular momentum and total spin, $(L, 2S_z)$. Many-body transitions are shown by arrows.	50
3.3	Schematic representation of magnetic field induced orbital and spin transitions.	51
3.4	Spectral function calculated by exact diagonalization as a function of magnetic field, up to 5 electrons.	52
3.5	Three dimensional plot of tunnelling current I_N (arb. units) as a function of magnetic field B and gate potential V_g , for perfect quantum dot without confining potential distortion. The height of the Coulomb peaks indicate relative magnitude of the current. (a). Coulomb peaks of transitions in 2,3,4 and 5-electron QD's at bias potential $\Delta\mu = 0.05$ meV and temperature $T = 0.2$ K. (b). Emphasizing the MDD-LDD transition for $N = 3$. The effect of increasing $\Delta\mu$ to 0.2 meV and T to 1K is shown in (c) and (d) respectively.	53

3.6	For a perfect dot with asymmetrical couplings to the two leads, this figure shows the tunnelling current as a function of gate voltage V_g for $N = 1$ to 5 . Solid lines represent positive bias and dashed lines negative bias.	55
4.1	Single particle density for a few lowest single particle states. (a) Density as a function of radial coordinate r , at $B = 1$ tesla and $B = 8$ tesla. Inset: the confining potential as a function of radial distance for the quantum dot. The confining potential is distorted from a perfect parabolic shape by a barrier that separates the dot into a core and a peripheral region. (b) Single-particle energy levels as a function of angular momentum m for quantum number $n = 0$, for the QD potential in the inset of (a).	59
4.2	Spectral function for the ground state transitions as a function of magnetic field B , for the weakly distorted QD. The empty regions are blockaded due to spin blockade or geometrical blockade.	62
4.3	Many-body ground state density function for 5 electrons versus radial coordinate r for the weakly distorted dot. Solid line is for $B = 4$ tesla, dashed line for $B = 6$ tesla, and dash-dotted line for $B = 8$ tesla. Localization of electrons in the core and in the peripheral regions is apparent.	63
4.4	Many-body ground states up to 5 electrons as a function of B , for a strongly distorted QD. The QD is schematized by an inner disc representing the core region and an outer ring representing the peripheral potential minimum. Thick lines represent blockaded regions during a transport measurement. The arrows indicate spin configuration of the electrons. For simplicity, only those states with equivalent localization-spin configuration representing more than 95% contributions to the exact ground state for $B < 3$ tesla, and more than 99.9% contributions for $B > 3$ tesla, are shown. For this QD, the transition from $N = 3$ to $N = 4$ between $B \approx 3.2$ tesla to 6.8 tesla, and the transition from $N = 4$ to $N = 5$ between $B \approx 6.8$ tesla to 9 tesla are geometrically blockaded.	64
4.5	Many-body ground state density function versus position r up to $N = 5$ at $B = 6$ tesla, for the strongly distorted QD. Solid lines are for the total radial charge distribution; dotted lines with solid squares are for spin-up contribution; dashed lines with empty squares are for spin-down contribution.	66
4.6	The addition spectra (chemical potential) of a strongly distorted QD as a function of B . The charging energy is substantially reduced after $N = 3$ due to spatial localization of electrons.	69
4.7	3D plot of tunnelling current (arb.units) as a function of B and V_g for a strongly distorted QD. (a) For $T = 0.2$ K and (b) for $T = 1$ K. Bias voltage and the asymmetry parameter λ are fixed at 0.05 meV and 0.01 respectively. The blockaded regions are clearly seen, and raising temperature may increase tunnelling current in the blockaded regime.	70

5.1	Single particle energy for different random disorder configurations used in DQMC calculations. Disorder number 0 corresponds to the clean QD case.	75
5.2	Many-body ground state energy as a function of magnetic field for (a) 4 electrons, (b) 6 electrons, (c) 9 electrons, and (d) 10 electrons. DQMC results are shown by solid lines (clean QD) and filled circles (disordered QD); UHF results are shown by dashed lines (clean QD) and open circles (disordered QD). For 4 electrons QD, exact results are also shown. The inset represents the confining potential of the first disordered QD (see Fig.1) and walker positions for $B = 0.9 \tau$ and $N = 4$	77
5.3	Addition spectrum as a function of magnetic field up to 10 electrons, for clean QD (solid lines) and the first disordered QD. Dotted and dashed lines represent left border of the MDD region for disordered and clean QD's respectively.	80
5.4	Addition energy at $B = 0$ up to 13 electrons for clean QD (the lowest line) and 8 different disorder configuration following the order represented in Fig.1 (2nd line and up). The numbers represent $2 \times S_z$, and they are shown for disordered QD's only if they differ from the clean QD results. Vertical scale is shifted by a constant amount in order to make the interpretation easier.	81
5.5	Superimposed many-body densities for spin up electrons, obtained by DQMC (dashed lines) and UHF (solid lines), for (a) clean QD, and (b) disordered QD. Only highest values are plotted in order to enhance the difference between DQMC and UHF results.	84
5.6	Superimposed many-body densities (a) obtained by UHF for spin up (solid lines) and spin down (dashed lines) electrons, (b) obtained by UHF (solid lines) and DQMC (dashed lines) for spin up electrons.	86
6.1	Energetic diagram of a QD in Kondo regime.	90
6.2	Schematic representation of the QD molecule. The bigger dot (QD ₁) where the electron-electron interactions are neglected is coupled to the leads. Smaller dot (QD ₂) acts as a Kondo impurity and is coupled to QD ₁	91
6.3	Conductance as a function of QD ₂ energy level for different temperatures. G_0 is the conductance for $\epsilon_d \rightarrow \infty$. Inset shows the average occupation number n_σ of QD ₂ . All the energy scale is renormalized in unit of Γ in this figure and in subsequent figures.	97
6.4	Local density of states inside QD ₁ at different QD ₂ energy levels. A narrow Kondo dip appears for small values of ϵ_d	98
6.5	Conductance as a function of ϵ_d of a 5 channel QD ₁ for different energy separation of the channels. Inset shows the average occupation number in QD ₂ , as a function of ϵ_d	99
6.6	Local density of states in QD ₂ . Kondo peak is enhanced as ϵ_d is decreased.	100

6.7	Conductance as a function of QD ₂ energy level ϵ_d , for different gate voltages applied to QD ₁ . When a transport channel inside QD ₁ is not aligned with the Fermi level of the leads, decreasing ϵ_d may lead to an increasing in conductance.	100
6.8	Conductance as a function of gate voltage V_g applied to QD ₁ , for different ϵ_d	101
A.1	Input/output flow chart of exact diagonalization calculations. The main codes are Intpot (calculation of two-body interaction potential elements), XDN (construction of different many-body Hamiltonian subspaces and diagonalization), and Lanczos (diagonalization). Input and output files are shown in ellipses.	113
A.2	Input/output flow chart of quantum Monte Carlo calculations. The main codes are HF (Hartree-Fock calculation of trial states), QMC (variational and diffusion quantum Monte Carlo calculations), and DenCal (density calculation). Input and output files are shown in ellipses.	115

Abstract

In this Ph.D thesis, electronic structure and transport properties of quantum dots are studied using advanced numerical techniques based on fundamental many-body theory. In fact, in such nanostructures, correlation and quantization effects dominate motion of electrons like in real atoms, hence an exact treatment is often necessary to understand and predict their electronic properties. Moreover, experimental realization of quantum dots in the presence of magnetic field gives rise to several new many-body physics that are inaccessible in real atoms, and they provide a crucial testing ground for important concepts of mesoscopic and nanoscopic phenomena.

The many-body tools used in this work include exact diagonalization, quantum Monte Carlo, Hartree-Fock, and Keldysh Nonequilibrium Green's function analysis. Each of these methods have their advantages and inconveniences. For studying closed systems with small number of electrons, exact diagonalization is the best choice, since it provides complete information about the total energy, wave functions and correlations for not only the ground state but also for excited states. We used exact diagonalization method to study in detail circular parabolic and ring shaped quantum dots containing up to 8 electrons, and we have found that spatial localization of electrons inside the dot gives rise to interesting new physics. On the other hand, for studying disordered quantum dots exact diagonalization method becomes powerless due to the broken spatial symmetry. Thus, we developed a fixed-phase quantum Monte Carlo algorithm combined with Hartree-Fock solutions, which allowed us to investigate the effect of impurities on electronic properties inside parabolic dots containing up to 13 electrons. To investigate open systems and transport properties, we have expanded exact diagonalization solutions in terms of Keldysh Green's functions which allowed us to discover a new transport blockade regime. Finally, again using Keldysh Green's function formalism, we have studied a double quantum dot system in the presence of Kondo resonance, and we have shown that multi-channel transport gives rise to particularly interesting competition effects between resonant tunneling and Kondo effect.

Résumé

Dans cette thèse de doctorat, la structure électronique et les propriétés de transport des points quantiques sont étudiées en se servant des techniques numériques basées sur la théorie fondamentale des systèmes à N -corps. En effet, dans ces nanostructures, tout comme dans les atomes réels, les effets de corrélation et de quantification dominent le mouvement des électrons. Un traitement exacte est donc souvent nécessaire pour être en mesure de mieux comprendre et de prédire leurs propriétés électroniques. De plus, la réalisation expérimentale des points quantiques en présence de champ magnétique donne lieu à des phénomènes physiques qui sont inaccessibles dans les atomes réels, en plus de fournir un champ d'essai pour des concepts importants en physiques nanoscopique et mésoscopique.

Les outils théoriques dont nous nous sommes servis dans ce travail incluent la diagonalisation exacte, la méthode Monte Carlo quantique, Hartree-Fock, et les fonctions de Green de Keldysh hors-équilibre. Chacune de ces méthodes ont leurs avantages et leurs inconvénients. Pour l'étude des systèmes ayant un petit nombre d'électrons, la diagonalisation est le meilleur choix, car elle fournit l'information complète sur l'énergie totale, les fonctions d'ondes et les corrélations, non seulement pour le niveau fondamental mais aussi pour les états excités. En utilisant cette méthode pour notre étude des points quantiques circulaires harmoniques et en forme d'anneau, nous avons montré que la localisation spatiale des électrons confinés donne lieu à de nouveaux phénomènes physiques fortement intéressants. Mais, pour l'étude des points quantiques en présence de désordre, la diagonalisation exacte devient impuissant à cause de la symétrie spatiale brisée. Alors, nous avons développé un algorithme Monte Carlo quantique à phase-fixe, combiné avec les solutions de Hartree-Fock, qui nous a permis d'étudier les effets des impuretés sur les propriétés électroniques dans les points quantiques paraboliques contenant jusqu'à 13 électrons. Afin d'étudier les propriétés de transport des systèmes ouverts, nous avons effectué une expansion des solutions de la diagonalisation exacte en terme de fonctions de Green, ce qui nous a permis de découvrir un nouveau régime de blockage de transport. Finalement, en se servant de nouveau du formalisme de fonctions de Green, nous avons étudié un système à points quantiques double en présence de résonance de Kondo, et nous avons montré que le transport à multi-niveaux donne lieu à une compétition particulièrement intéressante entre l'effet tunnel résonant et l'effet Kondo.

Statement of Originality

In this thesis, several numerical many-body techniques are developed, combined and used to study strongly correlated quantum dot nanostructures for which simpler semi-classical or mean-field approaches do not give correct physics. The applications of the techniques that we have elaborated concentrated on elucidating complex many-body phenomena arising from electron-electron interactions, geometrical factors, magnetic field, and transport properties of quantum dot systems. My original contributions to this study include:

- I developed an exact diagonalization code to calculate electronic properties of arbitrarily shaped circular three-dimensional quantum dots.
- I calculated many-body states using exact diagonalization algorithm and investigated energetic competition due to interaction, spin, magnetic field, and geometrical factors.
- By combining the Keldysh nonequilibrium Green's function (NEGF) formalism with exact diagonalization, I investigated charge transport in these quantum dots and discovered a new "Geometric blockade" phenomenon.
- I contributed to the development of quantum Monte Carlo and Hartree-Fock algorithms, and implemented a fixed-phase approximation allowing to investigate impurities under magnetic field. I applied this technique to study correlation effects in a completely disordered quantum dot, for the first time in the literature.
- I investigated by analytical and numerical analysis a double quantum dot system which allowed me to study Kondo resonance between quantized transport channels and a spin impurity.

Acknowledgments

First, I wish to thank my supervisor, Prof. Hong Guo, for giving me the opportunity to work in a really exciting field of research. With his constant dynamism, encouragement, guidance, and stimulation of creative abilities, I have learned many wonderful physics tools that I enjoyed playing with.

I am grateful to Prof. J.-S. Wang. His invaluable help in quantum Monte Carlo code allowed me to finish an important part of this thesis. I would also like to thank Prof. R. Harris for several discussions which helped me to organize my incoherent and chaotic thoughts. Thanks a lot to Dr. Q. F. Sun for the incredible patience that he showed to answer and reanswer to all my questions. I have learned a lot from his expertise in quantum transport theory.

I would like to thank all the group members for stimulating and fun physics discussions. Thanks especially to Brian, Hatem and Tiago. All your help and your friendship were greatly appreciated.

With its very friendly and enjoyable atmosphere, McGill physics department is a great place for working. Thanks to everybody who made my life in the department so pleasant, and of course to Red Shift Band for their amazing performance in department BBQ's!

I am very grateful for the financial support of my supervisor Hong Guo, and for the fellowships that I received from McGill and FCAR of Quebec.

Finally, I would like to thank my family. I could not have done my thesis without their invaluable support.

Introduction

During the last 20 years, advances in semiconductor processing techniques have made it possible to create small artificial structures with linear dimension of ~ 100 nm, containing only a small number of electrons. Such electronic systems, sometimes called *artificial atoms* [1, 2, 3, 4], have a discrete spectrum of energy levels (like natural atoms), and their “effective nuclear charge” can be controlled by metallic electrodes. These artificial atoms have been also given other names reflecting their different properties: *zero-dimensional electron gases*, referring to their confinement in all three spatial dimensions; *Coulomb islands*, due to dominant effects of Coulomb interactions; *single-electron transistors*, due to their transport properties which can vary by many orders of magnitude when its charge is changed by a single electron. In this work, we will call them *quantum dots* (QD’s), which is the mostly found terminology in the literature.

Why QD’s have attracted much attention experimentally and theoretically in recent years? First of all, needless to say that QD’s are a result of the advances in the miniaturization and control of semiconductor structures. This makes them a natural choice for the extension of shrinking electronic devices. Of course, building electronic circuits using QD’s that have reproducible and desired properties is and will be an immense challenge. Nevertheless, QD’s are one of the serious candidates for the technology needed to radically replace today’s microelectronic devices that are reaching their size and speed limits. On the other hand, QD’s are also very important from fundamental physics point of view, because their realization gives access to quantum effects in finite low-dimensional systems that were largely unexplored, by controlling

the electrostatic gates, dot geometry, or by an applied magnetic field. For instance, by applying a field of only a few Tesla to a QD-helium (that is a QD with 2 electrons), it is possible to observe correlation effects that would require several hundreds of thousands of Tesla in a real helium atom.

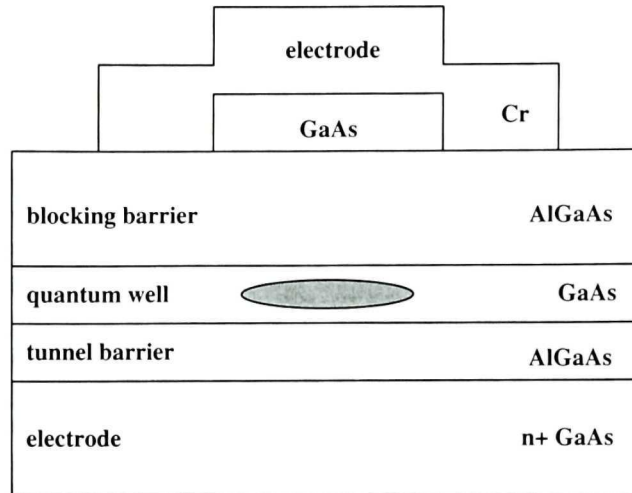


Figure 1.1: Schematic diagram of a QD located between two capacitor plate.

Regarding the observation of energy quantization, Reed *et al.* (1988) [5] performed pioneering experimental studies on etched heterostructure pillars, by measuring the current-voltage characteristics. Later, Ashoori *et al.* [6, 7] used a technique called *single-electron capacitance spectroscopy* (SECS), which allowed them to precisely control the number of electrons one by one from a completely depleted *single* microscopic region. Fig.1.1 is a schematic diagram of one of their samples[2]. The QD is located in the 10 nm thick *GaAs* quantum well between two capacitor plates. It is close enough to one of the plates to allow single electrons to tunnel through a 10 nm thick *AlGaAs* barrier, between the QD and the nearby plate. The blocking barrier is thick enough to prevent tunneling to the top electrode (gate). By increasing the gate voltage, electrons are attracted towards to QD. Since each time an electron tunnels inside the dot, the net Coulombic repulsion of confined electrons will be higher, it is necessary to increase further the gate voltage in order to allow one more electron to tunnel. Thus, by measuring the capacitance signal at specific gate voltages for which electrons can tunnel in or out, it is possible to study the electronic structure of the dot as a function

of an external magnetic field.

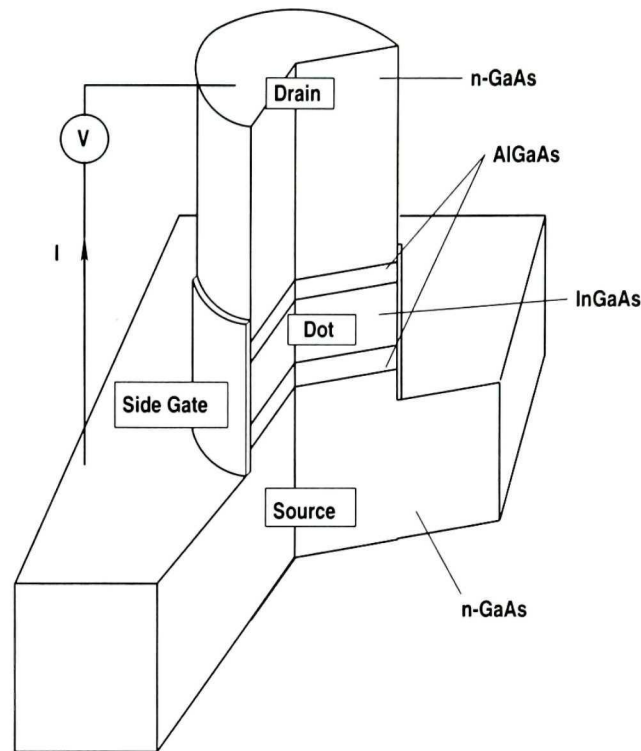


Figure 1.2: Schematic diagram of a QD in a gated transport spectroscopy experiment.

A more common experimental method known as *gated transport spectroscopy* (GTS) [8, 9, 10, 11] allowed Tarucha *et al.* (1996) to observe, for the first time, very clear experimental evidence for an atomic-like shell structure. Their experimental setup is schematized in Fig.1.2. QD is created in a 12 nm thick *InGaAs* layer between two 7.5 nm and 9 nm thick *AlGaAs* barriers. These barriers are thin enough to let electrons tunnel through. It is then possible to apply a bias voltage to measure a net current, and apply a gate voltage to control the attractive radial force in the QD to study its electronic structure and transport properties. To understand how, it is helpful to look at the schematic energy diagram of the system as a function of gate voltage, as shown in Fig.1.3. Let's assume that for a given gate voltage there is only one electron in the QD. If the chemical potential of the source is higher than the electron's energy, this confined electron cannot tunnel out. On the other hand, electrons in the drain cannot tunnel into the dot, because of the Coulombic repulsion U due to the electron already inside; the current is *Coulomb blocked*. This Coulomb blockade phenomenon is at the heart of the SECS and GTS experiments,

and is perhaps the most important property of QD's. Now, if we increase the gate voltage by $\sim U$ in order to lower the energy of the discretized dot states with respect to leads Fermi energy, a new channel becomes available for electrons to tunnel in and out, and current is non-zero. At a higher gate voltage, a second electron would be trapped in the dot and the current would again be blocked.

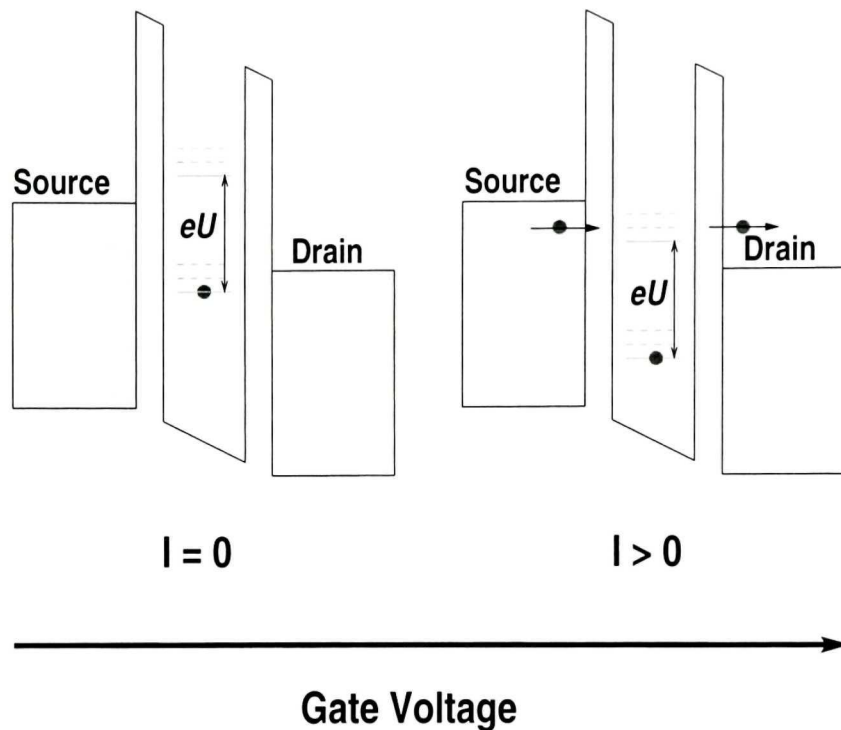


Figure 1.3: Schematic energy diagram of a QD as a function of applied gate voltage.

It is important to note that the above discussion, based on a single electron language, is very simplistic. In fact, the Coulomb repulsion U , also called addition energy, must be replaced by the difference in *total energy* of a N -electron state and a $(N + 1)$ -electron state, which contains very important information such as quantum dot geometry, exchange energy, correlation energy, spin, magnetic field etc[11]. Fig.(1.4), perhaps the most impressive experimental spectrum on clean QD's, shows the addition energy for a $N = 1$ up to 18 electron QD, as a function of magnetic field[10]. Without going into details for now, it is worth giving a feeling of some of the physics that can be studied by such addition spectrum. In the absence of magnetic field, the shell structure is reflected by an unusually large addition energy at electron numbers $N = 2, 6,$ and 12 . The dotted line and circles represent transitions

between different many-body states such as spin flips and charge redistributions induced by magnetic field, as obtained by analyzing “kinks” in the energy curves. For instance, at $N = 2$, the filled dot corresponds to the transition from a singlet state to a triplet state, showing that it is possible to precisely control the spin state of a single conduction electron in a sea of billions of valence electrons. It is also possible to study excited states by applying a finite bias[9].

Clearly, the precise values of magnetic field for which various many-body transitions occur, as well as the shell structure properties are complicated functions of electron number N , confinement potential strength, geometry, and electron-electron interactions. Thus, advanced quantum many-body techniques such as density-functional theory (DFT), Hartree-Fock (HF), quantum Monte Carlo (QMC), or even exact diagonalization, are necessary for a deeper understanding. These methods have already proven their utility in solid-state physics and quantum chemistry. For the study of QD's having less than 20 electrons, these theoretical methods became more and more popular, especially following the experimental success of SECS and GTS in studying correlation effects. For QD's having larger number of electrons, statistical approaches are used. These approaches include semi-classical method, based on an expansion of the Green's function in terms of classical trajectories, and random-matrix theories, which assume maximal ignorance regarding the system's Hamiltonian except that it must be consistent with the underlying symmetries. These methods are particularly useful for studying statistical properties and chaotic electron dynamics of QD's containing high number of electrons. However, the theoretical approach taken in this work is mostly concentrated on quantum many-body methods, with some flavor of statistical physics when necessary. Readers interested in statistical theories of QD's are referred to the review paper by Alhassid[4].

The most direct way to attack a correlated many-body problem is to apply exact diagonalization[12] method. By including enough number of configurations, *i.e.* Slater determinants made up from the single-particle basis states in the calculations, the solution converges to the exact result, and both ground and low-lying excited

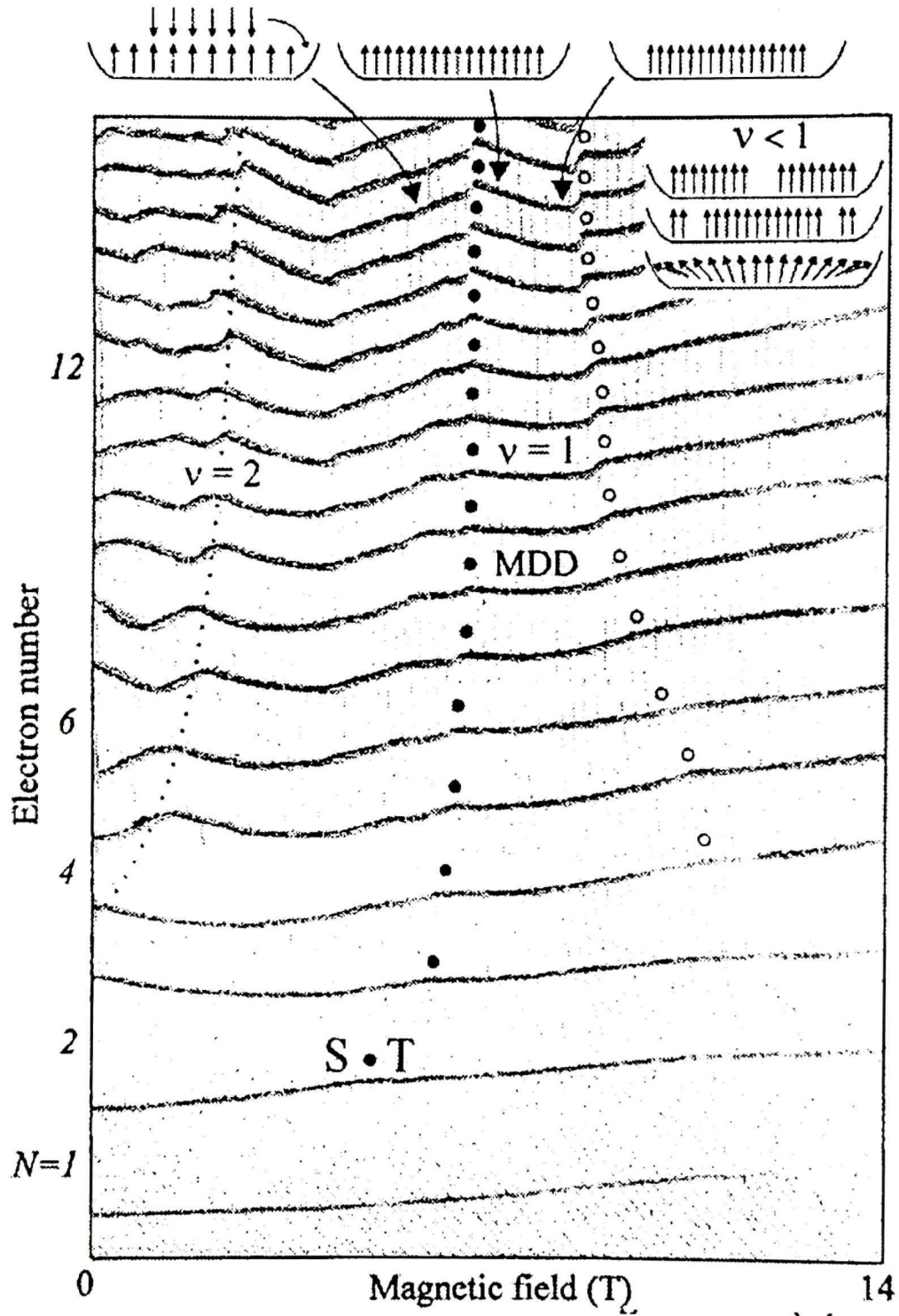


Figure 1.4: Addition spectrum of a circular QD, up to 18 electrons, taken from Ref.[10]. Vertical axis represents the chemical potential for a given number of electrons. ν is the filling factor defined as the number of flux lines per electron.

states are obtained. Applied to QD's for the first time by Maksym and Chakraborty [13], then later by Merkt *et al.* [14], and Johnson and Payne [15], exact diagonalization method has the advantage that, in addition to the ground-state energy and wave function, all low-lying excitations are computed with a good accuracy. However, since computational cost grows exponentially with the electron number N , exact diagonalization is so far limited to highly symmetric QD systems with small number of electrons ($N < 7$), [16, 17, 18, 19, 20, 21, 22, 23] unless additional approximations such as tight-binding models[24, 25] are done. Indeed, conservation of total angular momentum and total spin makes possible to reduce the many-body Hamiltonian of a circular QD system into smaller matrices. That is why exact diagonalization was found to be particularly useful for describing SECS and GTS experiments in which the system is *vertical*, with good circular symmetry properties. For *lateral* QD structures [26, 27], the coupling of the confinement region to the electrostatic gates breaks the symmetry of the system, making the exact diagonalization very difficult if not impossible[28].

Another very accurate method is the QMC technique[29] which allows the study correlations effect exactly while keeping the amount of computation to rise as $\sim O(N^3)$. The term "quantum Monte Carlo" covers several different techniques based on random sampling. The simplest of these, variational quantum Monte Carlo (VQMC), uses a stochastic integration method to evaluate expectation values for a chosen trial wave function. A more sophisticated version known as diffusion quantum Monte Carlo (DQMC), uses a projection technique to enhance the ground-state component of a starting trial wave function. Although there are other useful QMC methods such as auxiliary-field Monte Carlo[30], and path-integral Monte Carlo[31] (PIMC) which are in principal capable of simulating interacting electronic states at finite temperature, in this thesis we concentrate on the zero temperature VQMC and DQMC methods which have already proved their worth in solid-state physics. Regarding the QD structures, most of QMC calculations are done for circular parabolic systems using DQMC[32, 33, 34], VQMC[35, 36, 37, 38, 39], and PIMC[40, 41, 42]. However, one of

the great advantages of QMC over exact diagonalization method is the possibility to study systems which do not have a particular symmetry[43]. So far, this advantage has not been exploited much except the work by Wan *et al.* (1997)[44], and Lee *et al.* (1998)[45] on 2 electron QD systems containing a single impurity.

Other approaches to a description of finite quantum systems of interacting particles are based on the idea that the interactions, together with an external confinement, create an average “mean field”, which can be approximated by an effective potential in which particles are assumed to move independently. This mean field approximation forms the basis of Hartree-Fock[12] and practical density-functional theories[46] (DFT). It is recognized that in strongly correlated systems, these approximations can give substantial errors in energy and many-body wave function. Nevertheless, for a qualitative understanding of some properties of QD’s, Hartree-Fock[47, 48, 49, 50, 51, 52, 53, 54, 55, 56] and DFT[57, 58, 59, 60, 61, 62, 63] are used for their simplicity. Moreover, they are particularly useful for QMC methods since, Hartree-Fock and DFT wave functions can be used as trial states in VQMC and DQMC calculations. In this thesis, as we will see in chapter 5, we use Hartree-Fock solutions in our QMC calculations.

So far, the theoretical tools that we have considered help us to deal with closed systems. However, in a real experimental situation, especially in GTS experiments, the system interacts with leads, and one is also concerned with the transport properties. Moreover, coupling to the leads can give rise to very interesting many-body physics such as Kondo[64, 65, 66] and spin blockade[67, 68, 69, 45] effects. Theoretical study of transport through a strongly interacting region is a formidable problem, and no complete and practical theory exists so far. Even for non-interacting systems, quantum transport problem remains a big challenge[70, 71]. Most of the work on quantum transport including strong interactions is based on non-equilibrium Green’s function analysis[72, 73, 74, 75, 76] of a Hubbard Hamiltonian where the interacting region has only one channel for spin up and spin down electrons. To study QD’s with an arbitrary number of electrons, additional approximations, such as weak coupling

to the leads, must be done[77, 78, 79]. While this approximation gives very useful insight of many-body physics in the interacting region, higher order effects due to the coupling to the leads such as Kondo phenomenon, are completely neglected.

Despite many experimental and theoretical contributions so far, electron interaction effects, ground and excited state properties, of QD's remains an active subject of study. Many experimental investigations [80, 81, 82, 83, 84, 8, 26] have provided clear indications that the confining potential landscape can play an essential role to the many-body states and transport properties of the QD's. Several theoretical analysis have been reported in order to elucidate geometrical effects in strongly interacting regions, coming from random disorder[24, 25, 49, 52, 53, 62, 63], chaotic dots[50, 55], QD molecules[19, 51, 38], non-circular dots[60, 61], impurities[44, 45], and ring-shaped dots[85, 86, 87, 88]. It is the purpose of this thesis to report our investigation of geometrical factors, magnetic field, electron-electron interactions in few-electron QD's using theoretical quantum many-body tools. The organization of chapters is as follows.

In chapter 2, we review the basic theory behind the methods used in this work: Exact diagonalization, Hartree-Fock, QMC, and Keldysh Green's function transport formalism.

In chapter 3, we begin our study of QD's by recovering first the well known basic physics of the mostly studied QD system, a cylindrically symmetric parabolic confinement potential containing up to 5 electrons. This comes as a bridge towards largely unexplored quantum transport properties, as well as other geometrical effects which will be studied in following chapters. We perform exact diagonalization to calculate the eigenstates of the system, and combine the results with the Keldysh Green's function formalism. We show that the current is strongly dependent on many-body correlation effects at finite magnetic field, and the shell structure in the absence of magnetic field gives rise to very interesting current-voltage characteristics, directly reflecting the degeneracy of the many-body states.

In chapter 4, we study competition effects due to the existence of two potential

minima, on the electronic structure and transport properties of a QD system. We consider a ring-shaped QD having a peripheral potential region and a core region, and by taking advantage of circular symmetry, we use the same strategy as in the previous chapter, *i.e.* exactly diagonalizing the many-body Hamiltonian up to 5 electrons, and combining the results with the Keldysh Green's function technique. Our main results are: (i) Due to localization effects provided by the two local potential minima, there is an *abrupt* redistribution of electrons between the two potential minima in the QD as the magnetic field is varied; the electron density in the core potential minimum is suddenly changed at specific field strength. (ii) We have discovered a geometry induced blockade effect due to a spatial separation of electrons in the dot, which results in a suppression of conductance peaks at low temperature that should be testable experimentally. (iii) We have found that the addition spectra of the distorted QD show new behavior as electrons go into different spatial regions.

The goal of chapter 5, is to study the effect of random disorder in a parabolic confinement potential on the electronic structure up to 13 electrons. For this, we apply QMC methods since exact diagonalization becomes practically impossible to use to study such big systems with broken rotational symmetry. We first show that DQMC gives excellent total energy and spin configuration for clean-QD's as compared with exact diagonalization. Compared with the HF technique, we found that DQMC gives superior advantages in total energy accuracy, especially for low magnetic field regime. DQMC also reduces the problem of artificial density modulation in HF[56]. We found that disorder has a very significant effect to the total energy of QD. In particular, the energetic transitions (the kinks in energy) between many-body states are made much less clear due to disorder, and the required magnetic field to induce such transitions can be rather different than that of clean-QD. We also found that the Hund's rule for closed shells is robust against even strong disorder, but less so for open shells.

In chapter 6, we extend our study of quantum dots to "quantum dot molecules", *i.e.* 2 coupled quantum dots, and we concentrate on transport properties, notably

Kondo effect. To do this, we take a different approach as compared to previous chapters. Instead of solving the problem of closed system exactly, we start from a simpler Hubbard Hamiltonian, and expand it directly in terms of Green's functions, under mean field slave-boson approximation (infinite U -term). In particular, we concentrate on the effect of having several transport channels in one quantum dot, which are coupled to a second quantum dot treated as a Kondo impurity. Our results show that the competition between resonant transport and Kondo resonance gives rise to very interesting current-voltage oscillations.

In the last chapter, we summarize the main results of this thesis and suggest future developments in the direction we have taken. Finally, several pieces of technical details are summarized in the Appendices.

Theoretical Foundations

2.1 Introduction

In this chapter, we present theoretical tools which allow us to study electronic structure and transport properties of quantum dots. Since we are interested in strongly correlated systems, where single electron picture breaks down, many-body formalism becomes necessary to fully take into account interactions. In section 2.1, after introducing the general problem of interacting electrons in solids, we briefly review some of the basic notions in many-body physics with a focus on fermionic properties, such as antisymmetrization of wave functions, Slater determinants, second quantized formalism. Subsequent sections are devoted to the explanation of numerical techniques that we have developed to study electronic structure of closed systems, as well as the powerful quantum transport formalism based on Keldysh Green's functions that we use to study transport properties of open systems. In section 2.3, we introduce exact diagonalization technique for studying closed systems, by expanding the wave functions in terms of Slater determinants of non-interacting states. Hartree-Fock approximation, which serves us as a starting point for quantum Monte Carlo calculations, is explained in section 2.4. Quantum Monte Carlo technique, based on first quantized formalism in contrast with other methods, is presented in section 2.5. In particular, we explain in detail the *fixed-phase* approximation in diffusion quantum Monte Carlo method, necessary to study systems under external magnetic fields. Finally, in section 2.6, we give a brief introduction to Keldysh Green's function formalism, and we explain how it is applied to quantum transport problems when strong correlations are present.

2.2 Systems of interacting electrons

One of the greatest challenges of condensed-matter physics is to obtain accurate approximate solutions of the many-body Schrödinger equation. This, in general, includes the motion of electrons, nucleus and the electrostatic interactions between them (electron-electron, electron-nucleus, nucleus-nucleus). However, since the mass of an electron is much smaller compared to that of a nucleus, their dynamics can, to a good approximation, be decoupled. Within this approximation, known as Born-Oppenheimer or adiabatic approximation[89, 90], to the electrons ions are essentially stationary and many-electron wave function may be obtained by solving a time-independent Schrödinger equation given by the following Hamiltonian:

$$\hat{H} = -\frac{\hbar^2}{2m_e} \sum_i^N \nabla_i^2 - \sum_{i\alpha}^N \frac{Z_\alpha e^2}{|\mathbf{r}_i - \mathbf{d}_\alpha|} + \sum_i^N \sum_{j<i}^N \frac{e^2}{|\mathbf{r}_i - \mathbf{r}_j|}. \quad (2.1)$$

where \mathbf{r}_i is the position of the i^{th} electron, \mathbf{d}_α are the nucleus positions, and Z_α are the nuclear charges.

For semiconductor structures, which are our point of interest in this thesis, a very common approach is to use the *effective mass approximation*[89]: The electrons near the bottom of the conduction band which is assumed to be decoupled from the valence band, can be viewed as if they were moving in free space but with a mass given by some appropriately defined effective mass m^* . When these free electrons are “artificially confined” in nanostructures, their Hamiltonian becomes essentially similar to Eq.(2.1):

$$\hat{H} = -\frac{\hbar^2}{2m^*} \sum_i^N \nabla_i^2 + \sum_i^N V_{conf}(\mathbf{r}_i) + \frac{1}{\epsilon} \sum_i^N \sum_{j<i}^N \frac{e^2}{|\mathbf{r}_i - \mathbf{r}_j|}, \quad (2.2)$$

where V_{conf} represent the artificial confinement potential. It must be noted that the screening of electron-electron interactions due to the polarizability of the crystal within the effective mass approximation is taken into account through the phenomenological zero-frequency dielectric constant ϵ [90, 89].

2.2.1 Antisymmetrization of wave functions

Both Eqs.(2.1) and (2.2) form systems of identical particles. Since in quantum mechanics, identical particles must be indistinguishable (expectation values of operators must not change when the coordinates of two particles are interchanged in the wave function), their wave function must have permutation symmetry. For fermions, the wave function must be *antisymmetric* in order to ensure that two particles do not have the same set of quantum numbers and that Pauli exclusion principle is satisfied, so that

$$\Psi(\dots, x_i, \dots, x_j, \dots) = -\Psi(\dots, x_j, \dots, x_i, \dots), \quad (2.3)$$

where $x_i = (\mathbf{r}_i, \sigma_i)$ represents the space and spin coordinates of an electron.

As an example, let's first consider a system of N non-interacting electrons, $\hat{H}_0 = \sum_i^N \hat{h}_i$, for which the one-particle problem is assumed to be solved:

$$\hat{h}\psi_\alpha(x) = \epsilon_\alpha\phi_\alpha(x). \quad (2.4)$$

We can then construct antisymmetric solutions by using *Slater determinants* [91]:

$$\Phi_{NJ}(X) = \frac{1}{\sqrt{N!}} \begin{vmatrix} \phi_{\alpha_1}(x_1) & \dots & \phi_{\alpha_1}(x_N) \\ \vdots & & \vdots \\ \phi_{\alpha_N}(x_1) & \dots & \phi_{\alpha_N}(x_N) \end{vmatrix}, \quad (2.5)$$

where $X = (x_1, x_2, \dots, x_N)$. It can be verified that Φ_{NJ} 's defined this way are eigenfunctions of the Hamiltonian \hat{H}_0 with eigenenergies $\sum_i \epsilon_{\alpha_i}$. It is important to note that Slater determinant is only unambiguously defined by a given ordered N -tuple $(\alpha_1 < \alpha_2 < \alpha_3 < \dots)$, where α represents a set of quantum numbers such as $(n_\alpha, m_\alpha, \sigma_\alpha)$.

Now, if we turn on the electron-electron interaction term \hat{v} , Φ_{NJ} 's will not be eigenfunctions of $\hat{H} = \hat{H}_0 + \hat{v}$. Nevertheless, they can still be used as a basis set to construct a Hamiltonian matrix, which can then be diagonalized to find the eigenfunctions. This process is called exact diagonalization which is studied more in detail in section 2.3.

Few words about notation. Like in single particle quantum mechanics, many-body wave functions are often characterized by the following Dirac representation:

$$\langle X|N, J\rangle = \Phi_{NJ}(X), \quad (2.6)$$

where $|N, J\rangle$ is in general a linear combination of Slater determinants

$$|N, J\rangle = \sum_{\alpha} c_{\alpha} |\alpha_1 \alpha_2 \dots \alpha_N\rangle, \quad (2.7)$$

which should not be mistaken for tensor product that we will denote with a curved bracket:

$$|\alpha_1 \alpha_2 \dots \alpha_N\rangle \equiv |\alpha_1\rangle |\alpha_2\rangle \dots |\alpha_N\rangle. \quad (2.8)$$

2.2.2 Second quantization

Second quantization is an alternative formulation of quantum mechanics. It allows to study systems in which particles can be created or annihilated. To do this, we define annihilation and creation operators, \hat{a}_k and \hat{a}_k^{\dagger} , which allows us to map between different the N -particle Hilbert spaces. They can also be regarded as operators on a more general space, so-called *Fock space*, which is a product of all N -particle Hilbert spaces.

The action of \hat{a}_k^{\dagger} can be defined as $\hat{a}_k^{\dagger} |\alpha_1 \alpha_2 \dots \alpha_N\rangle = |k \alpha_1 \alpha_2 \dots \alpha_N\rangle$. Taking into account that for fermions indices must be ordered and no two electrons can occupy the same state, this gives

$$\hat{a}_k^{\dagger} |\alpha_1 \alpha_2 \dots \alpha_N\rangle = \begin{cases} (-1)^{j-1} |\alpha_1 \dots \alpha_{j-1} k \alpha_j \dots\rangle & \text{if } \alpha_{j-1} < k < \alpha_j \\ 0 & \text{if } k \in \{\alpha_1 \alpha_2 \dots \alpha_N\} \end{cases}, \quad (2.9)$$

where the phase $(-1)^{j-1}$ arises from rearrangement of terms in the determinant (each permutation gives rise to a -1 factor). Similarly we have, for the annihilation operator,

$$\hat{a}_k |\alpha_1 \alpha_2 \dots \alpha_N\rangle = \begin{cases} (-1)^{j-1} |\alpha_1 \dots \alpha_{j-1} \alpha_{j+1} \dots\rangle & \text{if there is a } j \text{ with } k = \alpha_j \\ 0 & \text{otherwise} \end{cases}. \quad (2.10)$$

Using these definitions, we can show that [91], annihilation and creation operators for fermions have following properties:

(i) Fermion creation and annihilation operators obey the anticommutation relations given by

$$\begin{aligned}\{\hat{a}_l, \hat{a}_k\} &= 0 \\ \{\hat{a}_l^\dagger, \hat{a}_k^\dagger\} &= 0 \\ \{\hat{a}_l^\dagger, \hat{a}_k\} &= \delta_{l,k}.\end{aligned}\tag{2.11}$$

(ii) Hamiltonians which contain single and two-particle operators, *i.e.*

$$\hat{H} = \sum_i^N \hat{h}(x_i) + \sum_{ij}^N \hat{v}(x_i, x_j),\tag{2.12}$$

as in equations 2.1 and 2.2, can be expressed in terms of creation and annihilation operators as

$$\hat{H} = \sum_{ij}^{\infty} \langle i|\hat{h}|j\rangle \hat{a}_i^\dagger \hat{a}_j + \frac{1}{2} \sum_{ijkl}^{\infty} (ij|\hat{v}|kl) \hat{a}_i^\dagger \hat{a}_j^\dagger \hat{a}_l \hat{a}_k.\tag{2.13}$$

The first term is diagonal if $\{\hat{a}_i\}$ correspond to non-interacting states. In solid state physics, most of the interesting many-body effects arise from the two-particle term in equation 2.13, and it will be discussed in detail in the section 2.3.1.

2.3 Exact diagonalization

Exact diagonalization method is the most direct and robust way to attack a many-body problem for a finite quantum system. It consists of diagonalizing the Hamiltonian of the equation (2.13), usually by using some of the eigenfunctions of the non-interacting part as a basis set. Then it is possible to obtain very accurate wave function and energy of the ground and excited states, hoping that the result will converge by increasing the size of the basis set before reaching the limits of given computational resources.

Assuming that single particle problem has been solved, the remaining major steps in exact diagonalization can be summarized as follow:

- Construction of two-body interaction terms $(ij|\hat{v}|kl)$

- Calculation of matrix elements of \hat{H}
- Diagonalization of \hat{H} .

In the following, we will give more details concerning these three steps.

2.3.1 Calculation of two-body interaction terms

A critical step in the numerical calculations is construction of the two-body interaction terms $(ij|\hat{v}|kl)$. They contain most of the interesting many-body physics, such as correlation and exchange interactions (in addition to the direct Coulomb interaction). They also reflect the symmetry of the system under investigation, which is important especially from numerical point of view, since the symmetry can be used to make diagonalization of larger systems possible.

The operator $(ij|\hat{v}|kl)$ can be separated into its spin and spatial parts:

$$\begin{aligned} (ij|\hat{v}|kl) &= \delta_{\sigma_i\sigma_k} \delta_{\sigma_j\sigma_l} \int d\mathbf{r}_1 d\mathbf{r}_2 \phi_i^*(\mathbf{r}_1) \phi_j^*(\mathbf{r}_2) v(\mathbf{r}_1, \mathbf{r}_2) \phi_k^*(\mathbf{r}_1) \phi_l^*(\mathbf{r}_2) \\ &\equiv \delta_{\sigma_i\sigma_k} \delta_{\sigma_j\sigma_l} v_{ijkl} \end{aligned} \quad (2.14)$$

where we define v_{ijkl} as the spatial part of $(ij|\hat{v}|kl)$. We note that terms like v_{ijij} represent the direct Coulomb interaction, whereas terms like v_{ijji} are so-called exchange terms, responsible for the magnetic phenomena[92] by favoring parallel spin alignment. The other terms are correlation terms, and they are responsible for mixing Slater determinants with different spatial distribution. One common characteristic of exchange and correlation terms is that, they are due to the overlap between wave functions: two electrons which are a part from each other are said to be uncorrelated. and there is no exchange force between them.

In order to calculate v_{ijkl} , it is convenient to expand the interaction term $v(\mathbf{r}_1, \mathbf{r}_2) = \frac{1}{|\mathbf{r}_1 - \mathbf{r}_2|}$ in a coordinate system which favor the symmetry of the system under investigation. For instance, for real atoms, one can use spherical harmonics. In our case, however, we mostly deal with systems having cylindrical symmetry, and following expansion in terms of Bessel functions is useful[93, 94]:

$$\frac{1}{|\mathbf{r}_1 - \mathbf{r}_2|} = \sum_{m=-\infty}^{\infty} \int_0^{\infty} dk k e^{im(\theta_1 - \theta_2)} J_m(k\rho_1) J_m(k\rho_2) e^{-k|z_1 - z_2|}. \quad (2.15)$$

The wave functions in a cylindrical system can be written as:

$$\phi_i(\mathbf{r}) = e^{-im_i\theta} R_i(\rho) Z_i(z). \quad (2.16)$$

Using equations (2.15) and (2.16), it is straightforward to show that

$$\begin{aligned} v_{ijkl} = & 4\pi^2 \delta_{m_i+m_j, m_k+m_l} \int dk \int dz_1 dz_2 \int d\rho_1 d\rho_2 \rho_1 \rho_2 \\ & \times J_{m_k-m_l}(k\rho_1) J_{m_j-m_l}(k\rho_2) R_i(\rho_1) R_k(\rho_1) R_j(\rho_2) R_l(\rho_2) \\ & \times e^{-k(z_1-z_2)} Z_i(z_1) Z_k(z_1) Z_j(z_2) Z_l(z_2) \end{aligned} \quad (2.17)$$

which essentially consists of double integrals. The particular form of this integral for a cylindrical parabolic confinement is given in appendix A.1.

It is important to note that this electron-electron scattering term conserves the total angular momentum $m_i + m_j$ as we can see from the delta function in equation (2.17). Since, in an N -body system, the angular momentum of all the electron couples will be conserved, the overall total angular momentum $L \equiv \sum_i^N m_{\alpha_i}$, will be a good quantum number, in addition to total spin S and its projection S_z .

2.3.2 Calculation of many-body matrix elements

Once all the v_{ijkl} 's are precalculated and tabulated, in principle it is possible to let the computer construct the many-body Hamiltonian \hat{H} , by directly using equation (2.13). However, it is convenient to take one more step before doing the numerical calculations. To construct \hat{H} , We need to calculate interaction matrix elements:

$$\langle \alpha'_1 \dots \alpha'_N | \hat{V} | \alpha_1 \dots \alpha_N \rangle = \frac{1}{2} \sum_{ijkl}^{\infty} (ij|\hat{v}|kl) \langle \alpha'_1 \dots \alpha'_N | \hat{a}_i^\dagger \hat{a}_j^\dagger \hat{a}_l \hat{a}_k | \alpha_1 \dots \alpha_N \rangle. \quad (2.18)$$

Using the following notation

$$\begin{cases} |\{\alpha_N\}\rangle \equiv |\alpha_1 \dots \alpha_N\rangle \\ |\{\alpha_N\} \bar{\alpha}_i\rangle \equiv \text{state } \{\alpha_N\} \text{ in which } \alpha_i \text{ is removed} \\ |\{\alpha_N\} \bar{\alpha}_i \bar{\alpha}_j\rangle \equiv \text{state } \{\alpha_N\} \text{ in which } \alpha_i \text{ and } \alpha_j \text{ are removed, with } i < j, \end{cases} \quad (2.19)$$

and applying the definition of annihilation operator giving in equation (2.9), we obtain:

$$\sum_{kl}^{\infty} |kl\rangle \hat{a}_l \hat{a}_k |\{\alpha_N\}\rangle = \sum_{l < k}^N (-1)^{k+l} (|\alpha_k \alpha_l\rangle - |\alpha_l \alpha_k\rangle) |\{\alpha_N\} \bar{\alpha}_l \bar{\alpha}_k\rangle. \quad (2.20)$$

A similar relation is obtained for the bra states. Note that in equation (2.20), summation in the left term is over the single particle states, while in the right term it is over the electrons. Finally, equation(2.18) gives

$$\begin{aligned} \langle \alpha'_1 \dots \alpha'_N | \hat{V} | \alpha_1 \dots \alpha_N \rangle &= \sum_{l < k}^N \sum_{j < i}^N (-1)^{i+j+k+l} ((\alpha'_i \alpha'_j | \hat{v} | \alpha_k \alpha_l) - (\alpha'_i \alpha'_j | \hat{v} | \alpha_l \alpha_k)) \\ &\times \langle \{\alpha'_N\} \bar{\alpha}'_j \bar{\alpha}'_i | \{\alpha_N\} \bar{\alpha}_l \bar{\alpha}_k \rangle. \end{aligned} \quad (2.21)$$

This is the equation which we use in order to calculate interaction matrix elements. The last term at in the right side is a delta function since cross product of two Slater determinants gives 1 or 0, depending on whether they are identical or not. These cross products test if it is possible to obtain a state $\{\alpha_N\}$ starting from a state $\{\alpha'_N\}$ following the scattering of two given electrons. Their determination is the most time consuming part of the matrix element calculations, since the two-body terms are usually pretabulated.

When building the many-body Hamiltonian, most important to remember is conservation of total angular momentum L , and projection of total spin S_z (although total spin S is also conserved, it is more convenient to consider its projection, since there is usually an applied magnetic field). That means the matrix elements like $\langle N, LS_z | \hat{H} | N, L'S'_z \rangle$ are zero. Hamiltonian can then be separated into independent subspaces with fixed L and S_z , as seen in Fig.(2.1). The advantage of doing this is clear: Instead of having one big matrix to diagonalize, we now have several but much smaller matrices to diagonalize.

2.3.3 Diagonalization

The size of a many-body Hamiltonian can be very large even for very low number of electrons. Let's consider that we build N -electron determinants from a set of n single electron states. The total number of N -electron Slater determinants is

$$\binom{n}{N} = \frac{n!}{(n-N)!N!}. \quad (2.22)$$

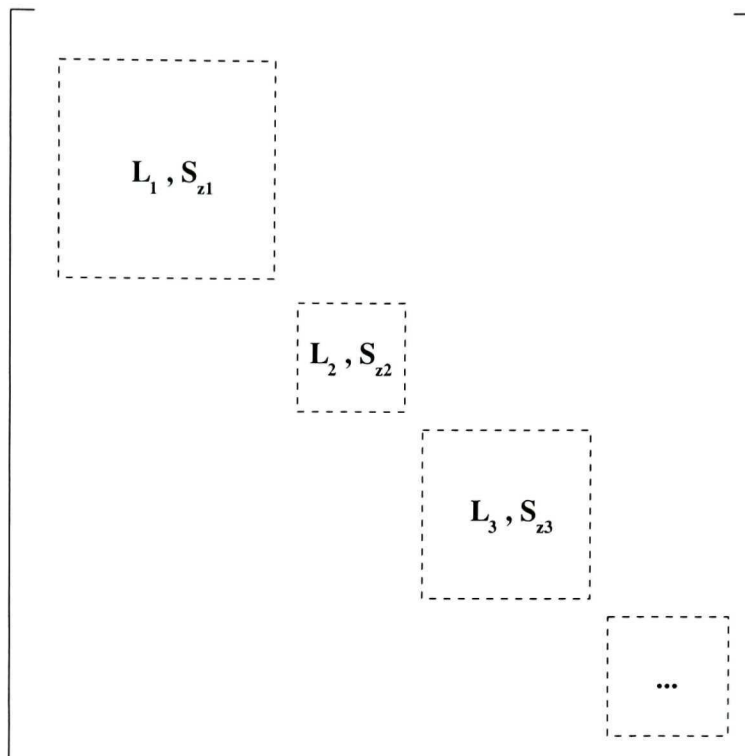


Figure 2.1: A many-body Hamiltonian with good quantum numbers L and S_z .

Usually n is few times greater than N , and equation(2.22) scales as $O(e^N)$ for large N . As an example, for $n = 40$ and $N = 6$, the size of \hat{H} becomes $\sim 4 \times 10^6$ which means we need to store $\sim 16 \times 10^{12}$ elements, well beyond the capabilities of today's computers. Taking advantage of good quantum numbers L and S_z , the size of matrices may be reduced to ~ 50000 , giving $\sim 25 \times 10^8$ elements to store, a number much more realistic for most of today's personal computers, considering that the matrices are usually very sparse. But inversion of several matrices of such size is still a very time consuming process. Thus, we use a special technique known as Lanczos diagonalization[95], which is a very accurate way to find lowest eigenstates of a real symmetric matrix. It is based on the idea that a real symmetric matrix can be converted to a tridiagonal form, which is much simpler to invert. It is a well-known method and extensively used in the literature to deal with large matrices. Technical details of the Lanczos process can be found in[95].

2.3.4 Calculation of electronic density

In this section, we discuss the computation of a quantity of physical interest, electronic density, from the result of exact diagonalization. Although it may sound like a straightforward calculation since the wave functions are known, it must be computed with care when dealing with linear combinations of thousands of N -electron Slater determinants.

Electronic density $\rho(x)$ for a many-body wave function $\Psi_{NJ}(X)$, is given by

$$\rho(x) = N \int dx_2 dx_3 \dots dx_N |\Psi_{NJ}(x, x_2, \dots, x_N)|^2, \quad (2.23)$$

where the integration includes summation over spin degree of freedom. From this equation, we can define many-body density operator as

$$\hat{\rho}(x) = \sum_{i=1}^N \delta(x - x_i). \quad (2.24)$$

Using equation(2.13), second quantized form of the density operator can then be expressed as[91]:

$$\hat{\rho}(x) = \sum_{i,j}^{\infty} \phi_i^*(x) \phi_j(x) \hat{a}_i^\dagger \hat{a}_j. \quad (2.25)$$

In numerical calculations, after the diagonalization is performed, the state $|N, J\rangle$ is a linear combination of Slater determinants:

$$|N, J\rangle = \sum_{\alpha} c_{\alpha} |\{\alpha_N\}\rangle. \quad (2.26)$$

Finally, using the definitions (2.19), we obtain a rather messy, but more convenient expression for the numerical calculations of the electronic density:

$$\rho(x) = \sum_{\alpha'} \sum_{\alpha} c_{\alpha'}^* c_{\alpha} \sum_{i,j}^N (-1)^{i+j} \phi_{\alpha'_j}^*(x) \phi_{\alpha_i}(x) \langle \{\alpha'_N\} \bar{\alpha}'_j | \{\alpha_N\} \bar{\alpha}_i \rangle. \quad (2.27)$$

2.4 Hartree-Fock approximation

We have seen in the previous section that in order to correctly express eigenstates of an interacting N -electron system, we need to build linear combination of Slater determinants by diagonalizing the many-body Hamiltonian, which is a very intensive

process. Let's now assume that we want to approximate the ground wave function by a single determinant. This can be done by optimizing the exact Hamiltonian $\hat{H} = \sum_i^N \hat{h}(x_i) + \sum_{ij}^N \hat{v}(x_i, x_j)$ with respect to single particle states $\phi(x)$ from which Slater determinant is built. Doing so, we obtain *Hartree-Fock equations*[12, 91, 90]:

$$\begin{aligned} h(x)\phi_\alpha(x) + \int dy \sum_i^N \phi_i^*(y)\phi_i(y)\phi_\alpha(x) \\ - \int dy \sum_i^N \phi_i^*(y)\phi_i(x)v(x, y)\phi_\alpha(y) = \epsilon_\alpha\phi_\alpha(x). \end{aligned} \quad (2.28)$$

As we can see, the many-body problem is reduced to a single-particle problem, in which each electron moves in a mean-field potential produced by all other particles. However, Hartree-Fock equations cannot be solved like a normal eigenvalue problem due to non-linear terms in the effective mean-field potential. Instead, we must solve it by iterations, using a self-consistent procedure. To understand how, let's express Hartree-Fock equation in matrix form using the basis set of non-interacting electrons $|m\rangle$ such that $|\phi_i\rangle = \sum_m c_{mi}|m\rangle$. Equation(2.28) becomes

$$\langle k|\hat{h}_{HF}|l\rangle = \langle k|\hat{h}|l\rangle + \sum_{mn}^{\infty} \hat{\rho}_{mn}[(km|\hat{v}|ln) - (km|\hat{v}|nl)], \quad (2.29)$$

where $\hat{\rho}_{mn}$ are the density matrix elements given by

$$\hat{\rho}_{mn} = \sum_i^N c_{mi}^*c_{ni}. \quad (2.30)$$

Then the equation (2.29) can be solved using diagonalization technique by updating $\hat{\rho}_{kl}$ after each iteration, until convergence is reached (see Fig(2.2)). It is clear that equation (2.29) will give an infinite number of eigenfunctions in principle. The ground state of the many-body system is then constructed using N lowest states. Note that the corresponding total Hartree-Fock energy is not obtained by simply adding N -lowest eigenenergies of the Hartree-Fock Hamiltonian, since each eigenenergy contains interaction energy due to all other electrons. To avoid double counting, the safest way to calculate the total energy is by inserting the Slater determinant of the occupied states in the exact Hamiltonian:

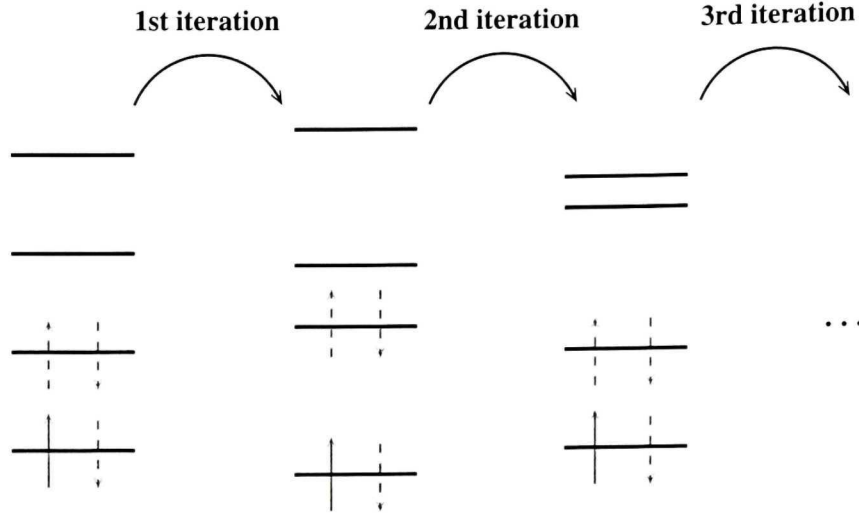


Figure 2.2: Schematized Hartree-Fock procedure.

$$\begin{aligned}
 \langle N | \hat{H} | N \rangle &= \sum_i^N \langle \phi_i | \hat{h} | \phi_i \rangle + \frac{1}{2} \sum_{ij}^N [(\phi_i \phi_j | \hat{v} | \phi_i \phi_j) - (\phi_i \phi_j | \hat{v} | \phi_j \phi_i)] \\
 &= \sum_{kl}^{\infty} \hat{\rho}_{kl} \langle m | \hat{h} | n \rangle + \sum_{kl}^{\infty} \hat{\rho}_{kl} \frac{1}{2} \sum_{mn}^{\infty} \hat{\rho}_{mn} [(km | \hat{v} | ln) - (km | \hat{v} | nl)] \quad (2.31)
 \end{aligned}$$

This equation is often used to define direct, exchange, and correlation energy of a N -electron system: second right term is direct energy, third right term is the exchange energy, whereas correlation energy can be defined as $E_{exact} - E_{HF}$ [12].

2.4.1 Restricted and unrestricted Hartree-Fock

As mentioned before, in the systems we are studying, total angular momentum L and z -component of the total spin S_z are conserved and they must commute with the non-relativistic Hamiltonian. The Hartree-Fock Hamiltonian, however, does not commute with any of these operators. Consequently, the solutions of the Hartree-Fock equations do not have proper symmetry. This is due to the symmetry breaking mean-field potential in equation (2.28).

A simple way to construct Hartree-Fock wave functions with better symmetry properties is to restrict “artificially” the single electron states to have some fixed

quantum numbers during the calculations. This will force the Hartree-Fock self-consistent procedure to converge towards a local minima with right symmetry that corresponds to these quantum numbers. In most of the Hartree-Fock calculations z -projection of the spin, s_z , is restricted such that S_z commutes with the Hartree-Fock Hamiltonian.

$$\begin{aligned}\phi_i^{HF}(x) &= \phi_i^{(+)}(\mathbf{r})\chi_+(s_z) & i = 1, \dots, N_+ \\ \phi_{i+N_+}^{HF}(x) &= \phi_{i+N_+}^{(-)}(\mathbf{r})\chi_-(s_z) & i = 1, \dots, N_-\end{aligned}\tag{2.32}$$

where N_+ and N_- are the number of spin up and spin down electrons, respectively. This procedure is often badly called *unrestricted Hartree-Fock* (UHF) in order to emphasize the difference between this restricted procedure and further restrictions on spatial states (such as angular momentum)[91]. We will also use this terminology in this thesis.

When further restrictions are imposed, such as assuming that single particle orbitals are eigenfunctions of the angular momentum operator, the ground state energy calculated by this restricted Hartree-Fock method increases. We encounter a fundamental problem known as *symmetry dilemma* of the Hartree-Fock procedure[91]: if the best possible ground state energy is sought, single particle states should be free to vary. If the symmetry is improved by restricting the variation of the orbitals, the ground state energy increases. However, it is possible to improve the symmetry of the UHF solutions by applying a projection method such as diffusion Monte Carlo method, as we will see later in this thesis.

2.5 Variational Monte Carlo

The variational Monte Carlo method is the simpler of the two zero temperature quantum Monte Carlo methods discussed in this thesis. It is a direct application of Monte Carlo calculation of multidimensional integrals. It was first used by McMillan[96] to calculate the ground state properties of liquid ^4He and then generalized to fermion systems by Ceperley *et al.*[97].

The VQMC method relies on the availability of a trial wave function $\Psi_T(\mathbf{R})$ that is a reasonably good approximation of the exact ground state wave function (we

assume spinless electrons for now). This trial wave function must satisfy following conditions: (i) it is antisymmetric for fermions, (ii) both Ψ_T and its $\nabla\Psi_T$ must be continuous wherever the potential is finite, (iii) integrals $\int d\mathbf{R}\Psi_T^*\Psi_T$, $\int d\mathbf{R}\Psi_T^*\hat{H}\Psi_T$, and $\int d\mathbf{R}\Psi_T^*\hat{H}^2\Psi_T$ should exist. Its variational energy is then an upper bound to the exact ground state energy E_0 :

$$E_V = \frac{\int d\mathbf{R}\Psi_T^*(\mathbf{R})\hat{H}\Psi_T(\mathbf{R})}{\int d\mathbf{R}\Psi_T^*(\mathbf{R})\Psi_T(\mathbf{R})} \geq E_0, \quad (2.33)$$

which can be rewritten as

$$E_V = \int d\mathbf{R}P(\mathbf{R})g(\mathbf{R}), \quad (2.34)$$

where we defined $P(\mathbf{R}) \equiv |\Psi_T|^2 / \int d\mathbf{R}|\Psi_T|^2$, and $g(\mathbf{R}) \equiv \Psi_T^{-1}\hat{H}\Psi_T$. Since, $P(\mathbf{R})$ is a normalized probability distribution, in principle we can generate a set of random vectors \mathbf{R}_m sampled from $P(\mathbf{R})$, then compute the sample average

$$E_V \approx \frac{1}{M} \sum_{m=1}^M g(\mathbf{R}_m). \quad (2.35)$$

This is the basic idea behind evaluating multidimensional integrals with Monte Carlo methods[29, 31].

2.5.1 Metropolis algorithm

One technical difficulty of the Monte Carlo evaluation of high-dimensional integrals as described above is the necessity of sampling complicated probability distributions with, in general, unknown normalization. The Metropolis rejection algorithm[29] is a very nice and useful method that allows an arbitrarily complex distribution to be sampled in a straightforward way without knowledge of its normalization.

In Metropolis algorithm, the random vectors \mathbf{R}_m , often called *walkers*, have now a dynamics of their own: they are allowed to change their position by random walks obeying a transition probability $T(\mathbf{R} \leftarrow \mathbf{R}')$ which must satisfy the *detailed balance* [31]

$$T(\mathbf{R} \leftarrow \mathbf{R}')P(\mathbf{R}') = T(\mathbf{R}' \leftarrow \mathbf{R})P(\mathbf{R}) \quad (2.36)$$

ensuring the equilibrium state $P(\mathbf{R})$. The unknown transition probability $T(\mathbf{R}' \leftarrow \mathbf{R})$ can be split into an arbitrary sampling distribution $T_0(\mathbf{R}' \leftarrow \mathbf{R})$, and an unknown

acceptance probability $A(\mathbf{R}' \leftarrow \mathbf{R})$. Since $0 \leq A \leq 1$ by definition, equation (2.36) can be rewritten as

$$A(\mathbf{R}' \leftarrow \mathbf{R}) \leq \text{Min} \left(1, \frac{T_0(\mathbf{R} \leftarrow \mathbf{R}')P(\mathbf{R}')}{T_0(\mathbf{R}' \leftarrow \mathbf{R})P(\mathbf{R})} \right). \quad (2.37)$$

We can now describe the Metropolis algorithm as following:

- Choose a $T_0(\mathbf{R}' \leftarrow \mathbf{R})$ that is easy to sample (Gaussian, hard-wall cubic, etc.).
- Initialize walkers position (randomly or from a previous calculation).
- Make a trial move to a new position \mathbf{R}' sampled from T_0 .
- Accept the trial move with the probability

$$\text{Min} \left(1, \frac{T_0(\mathbf{R} \leftarrow \mathbf{R}')P(\mathbf{R}')}{T_0(\mathbf{R}' \leftarrow \mathbf{R})P(\mathbf{R})} \right). \quad (2.38)$$

- Collect averages.

Using a judicious parameterization of $\Psi_T(\mathbf{R})$, it is then possible to optimize the parameters and obtain an accurate upper bound for the ground state energy [29]. In this work, we use VQMC to equilibrate the walkers to be used in the more advanced diffusion Monte Carlo method.

2.6 Diffusion Monte Carlo

Diffusion Monte Carlo method is, in principle, an exact method for calculating the ground state of a many-body system. It is one of the so-called *projector Monte Carlo methods* where the ground state is projected out from an arbitrary wave function with the help of an operator of the Hamiltonian.

Diffusion Monte Carlo method is often introduced by writing the many-body Schrödinger equation in imaginary time (in the following we use effective atomic units defined by setting $e = m^* = \hbar = 4\pi\epsilon_0\epsilon = 1$):

$$-\frac{\partial}{\partial t}\Phi(\mathbf{R}, \mathbf{t}) = (\hat{H} - E_T)\Phi(\mathbf{R}, \mathbf{t}), \quad (2.39)$$

where t is a real variable measuring the progress in imaginary time, and E_T is an energy offset (it's utility will be clear soon). This equation may be rewritten in the integral form:

$$\Phi(\mathbf{R}, t + \tau) = \int d\mathbf{R}' G(\mathbf{R}\mathbf{R}', \tau) \Phi(\mathbf{R}', t), \quad (2.40)$$

with

$$G(\mathbf{R}\mathbf{R}', \tau) \equiv \langle \mathbf{R} | e^{-\tau(\hat{H} - E_T)} | \mathbf{R}' \rangle \quad (2.41)$$

is a Green's function that obeys equation (2.39). Let's define a trial function $\Psi_{init}(\mathbf{R}) \equiv \Phi(\mathbf{R}, t = 0)$ and expand it in terms of eigenfunctions of \hat{H} :

$$\Psi_{init}(\mathbf{R}) = \sum_J \langle \Phi_J | \Psi_{init} \rangle \langle \mathbf{R} | \Phi_J \rangle. \quad (2.42)$$

Then, equation (2.40) becomes

$$\Phi(\mathbf{R}, \tau) = \sum_J \langle \Phi_J | \Psi_{init} \rangle \Phi_J(\mathbf{R}) e^{-\tau(E_J - E_T)}. \quad (2.43)$$

Finally, when we take the limit when τ approaches infinity, we end up with the ground state

$$\lim_{\tau \rightarrow \infty} \Phi(\mathbf{R}, \tau) = \langle \Phi_0 | \Psi_{init} \rangle \Phi_0(\mathbf{R}) e^{-\tau(E_0 - E_T)}, \quad (2.44)$$

since the excited states are all exponentially damped. The role of the offset energy E_T is now clear: it keeps the overall normalization of $\Phi_0(\mathbf{R})$ fixed when $E_T \approx E_0$. Equation (2.44) which is the fundamental property of the projector $e^{-\tau(\hat{H} - E_T)}$ forms the basis of the diffusion Monte Carlo method. Same ideas apply to other projectors such as $[1 + \tau(\hat{H} - E_T)]^{-1}$ used in *Green's function Monte Carlo* [98], or $[1 - \tau(\hat{H} - E_T)]$ used in *Power Monte Carlo* [99]. Note that the trial wave function must have an overlap with the ground state. If they are orthogonal, instead of finding the ground state, we will find the lowest excited eigenstate having an overlap with Ψ_{init} .

It is generally only feasible to determine $G(\mathbf{R}\mathbf{R}', \tau)$ explicitly for small τ , and the integral of the equation (2.40) must be solved by iterations. We can then represent the distribution $\Phi(\mathbf{R}, t)$ by walkers, *i.e.* a set of discrete sampling points \mathbf{R}_m , and move each walker to a new position \mathbf{R}'_m by the probability given by $G(\mathbf{R}\mathbf{R}', \tau)$ (see Fig.(2.3)).

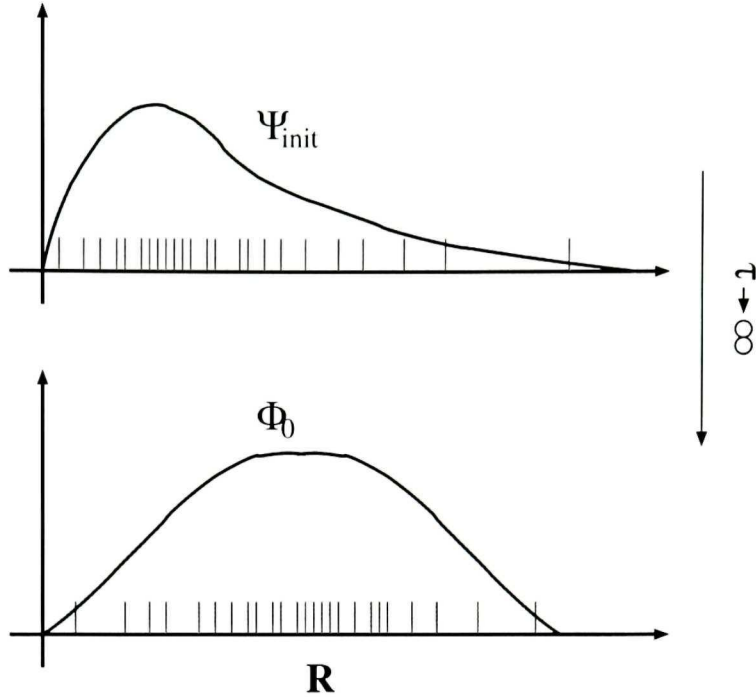


Figure 2.3: Schematic representation of DQMC process. Density of walkers which are shown by vertical lines, represent the state of the system. Each walker moves according to the Green's function $G(\mathbf{R}\mathbf{R}', \tau)$. Starting from an arbitrary initial state, the result converges to the ground state. Note that \mathbf{R} is a $3N$ dimensional vector.

To find an approximate expression for Green's function $G(\mathbf{R}\mathbf{R}', \tau)$, Trotter-Suzuki formula for the exponential of a sum of operators is used [29]. That gives

$$G(\mathbf{R}\mathbf{R}', \tau) = \langle \mathbf{R} | e^{-\tau(\hat{T} + \hat{V} - E_T)} | \mathbf{R}' \rangle$$

$$\approx e^{-\tau[V(\mathbf{R}) - E_T]/2} \langle \mathbf{R} | e^{-\tau\hat{T}} | \mathbf{R}' \rangle e^{-\tau[V(\mathbf{R}) - E_T]/2} + O(\tau^3), \quad (2.45)$$

where $\langle \mathbf{R} | e^{-\tau\hat{T}} | \mathbf{R}' \rangle$ is the Green's function for a *diffusion process*, which can be calculated by expanding the operator $e^{-\tau\hat{T}}$ in terms of plane-waves. Finally we obtain

$$G(\mathbf{R}\mathbf{R}', \tau) \approx G_d(\mathbf{R}\mathbf{R}', \tau) G_b(\mathbf{R}\mathbf{R}', \tau) \quad (2.46)$$

with

$$\begin{cases} G_d(\mathbf{R}\mathbf{R}', \tau) \equiv (2\pi\tau)^{-3N/2} \exp\left[-\frac{(\mathbf{R}-\mathbf{R}')^2}{2\tau}\right] \\ G_b(\mathbf{R}\mathbf{R}', \tau) \equiv \exp[-\tau(V(\mathbf{R}) + V(\mathbf{R}') - 2E_T)/2]. \end{cases} \quad (2.47)$$

The diffusion Green's function G_d is a Gaussian with a variance of $3N\tau$ which can be sampled using for instance Box-Muller method [100]. This will assign new position $\mathbf{R}'_{\mathbf{m}}$ to each walker, similar to the VQMC case. The *branching* Green's function G_b

acts as a time-dependent renormalization term. There are various ways to incorporate the effect of renormalization into the walkers “life”. Most efficient is the *branching or birth/death algorithm* [101], which determines whether the walker will survive after it moves, or it will be duplicated. Number of copies can be calculated by taking the integer part of $(u + G_b)$ where u is a uniform random number in $(0, 1)$. As a result, if the potential energy is less than the ground state energy, duplicate copies are generated. In the regions of very high potential energy, the walker will most likely die. Note that $V(\mathbf{R})$ includes overall electron-electron interactions as well as the confining potential.

How is E_T fixed? Actually, it is not fixed but occasionally adjusted to keep the population (total number of walkers) during the simulation constant. Since the amplitude of the wave function depends exponentially on E_T (see equation (2.44)), E_T can be updated using $E_T^{new} = E_T^{old} + \kappa \ln(P_0/P)$, where P is the current population, P_0 is the desired population, and κ is a feedback parameter chosen to be small to minimize the bias effect. This way of adjusting E_T to achieve a stable ground state distribution $\Phi_0(\mathbf{R})$, can be used as an estimator for the eigenenergy E_0 . However, we will see that there is a better way of calculating the eigenenergy.

2.6.1 Importance sampling and fixed-phase approximation

The above scheme, first suggested by Fermi, actually fails on many-body systems because the potential $V(\mathbf{R})$ is unbounded. In fact, the Coulomb potential can go to infinity when two particles coincide, making the renormalization process ill defined. Moreover, so far we have assumed that the wave function is real and positive for all \mathbf{R} (walkers must represent a distribution function), which is obviously not the case for fermions: due to their antisymmetry, fermionic wave functions may have *nodes*, where the sign of the wave function changes. This problem is known as *fermion sign problem*. They can even be complex when, for instance, there is an external magnetic field.

There is fortunately a simple cure known as importance sampling to these two problems (renormalization, and antisymmetry) discovered to deal with the renormal-

ization problem[102, 103]. Instead of sampling $\Phi(\mathbf{R}, t)$ with walkers, we now sample a new function defined by $f(\mathbf{R}, t) = \Phi^*(\mathbf{R}, t)\Psi_T(\mathbf{R})$, where Ψ_T is a known trial function. Clearly, if we assume that the Ψ_T and Φ have same phase, f will always be real and positive. This condition is automatically satisfied when we represent f by walkers, since walkers live in a “real and positive world”. This is known as *fixed-phase* approximation first time introduced by Ortiz *al.*[104] then applied to quantum dots by Bolton [32]. It is basically a straightforward generalization of the much more familiar *fixed-node* approximation for real wave functions[29]. In the following, we explain in detail how to use fixed-phase approximation through importance sampling.

To implement importance sampling into the calculations, we insert the definition of f into the equation (2.39):

$$-\frac{\partial}{\partial t}f(\mathbf{R}, t) = -\frac{1}{2}\nabla^2 f(\mathbf{R}, t) + \nabla[\mathbf{v}_D(\mathbf{R})f(\mathbf{R}, t)] + [E_L(\mathbf{R}) - E_T]f(\mathbf{R}, t), \quad (2.48)$$

where ∇ is the $3N$ -dimensional gradient operator, $\mathbf{v}_D(\mathbf{R})$ is the $3N$ -dimensional *drift velocity* defined by

$$\mathbf{v}_D(\mathbf{R}) = \Psi_T(\mathbf{R})^{-1}\nabla\Psi_T(\mathbf{R}), \quad (2.49)$$

and $E_L(\mathbf{R})$ is the *local energy* defined by

$$E_L(\mathbf{R}) = \Psi_T(\mathbf{R})^{-1}\hat{H}\Psi_T(\mathbf{R}). \quad (2.50)$$

Note that both drift velocity and local energy have a real and imaginary part, because $\Psi_T(\mathbf{R}) = e^{-i\Theta(\mathbf{R})}|\Psi_T(\mathbf{R})|$. However, since $f(\mathbf{R})$ is considered to be a real function, it can be verified that the real and imaginary parts of the equation (2.48) are decoupled, and the imaginary part contains no new information in the fixed-phase approximation. Moreover, since the imaginary parts are Hermitian and purely imaginary (see appendix A.2), their expectation values $\langle\mathbf{v}_D(\mathbf{R})\rangle$ and $\langle E_L(\mathbf{R})\rangle$ must be real. We therefore use following quantities as the drift velocity and local energy in the numerics:

$$\begin{aligned} \tilde{\mathbf{v}}_D(\mathbf{R}) &\equiv \text{Re}\{\Psi_T(\mathbf{R})^{-1}\nabla\Psi_T(\mathbf{R})\}, \\ \tilde{E}_L(\mathbf{R}) &\equiv \text{Re}\{\Psi_T(\mathbf{R})^{-1}\hat{H}\Psi_T(\mathbf{R})\}. \end{aligned} \quad (2.51)$$

With these definitions, fixed-phase approximation is enforced (imaginary parts can be used as check quantities). In appendix A.2, we give explicit expressions of these terms applied to our quantum dots. We can now write the integral form of the equation (2.48) as

$$f(\mathbf{R}, t + \tau) = \int d\mathbf{R}' \tilde{G}(\mathbf{R}\mathbf{R}', \tau) f(\mathbf{R}', t), \quad (2.52)$$

where the modified Green's function \tilde{G} is by definition equal to $\Psi_T(\mathbf{R})G(\mathbf{R}\mathbf{R}', \tau)\Psi_T(\mathbf{R}')^{-1}$. As for the G , \tilde{G} can be evaluated in the short-time ($\tau \approx 0$) approximation:

$$\tilde{G}(\mathbf{R}\mathbf{R}', \tau) \approx \tilde{G}_d(\mathbf{R}\mathbf{R}', \tau)\tilde{G}_b(\mathbf{R}\mathbf{R}', \tau) \quad (2.53)$$

with

$$\begin{cases} \tilde{G}_d(\mathbf{R}\mathbf{R}', \tau) \equiv (2\pi\tau)^{-3N/2} \exp\left[-\frac{[\mathbf{R}-\mathbf{R}'-\tau\tilde{\mathbf{v}}_D(\mathbf{R}')]^2}{2\tau}\right] \\ \tilde{G}_b(\mathbf{R}\mathbf{R}', \tau) \equiv \exp\left[-\tau\left(\tilde{E}_L(\mathbf{R}) + \tilde{E}_L(\mathbf{R}') - 2E_T\right)/2\right]. \end{cases} \quad (2.54)$$

There are 2 differences between equations (2.54) and (2.47): first, in \tilde{G}_b we now have local energy \tilde{E}_L instead of the potential energy. This is crucial because for a good trial state Ψ_T , \tilde{E}_L is roughly constant, so that the fluctuations of \tilde{G}_b is much diminished compared to G_b . Also, in the diffusion Green's function \tilde{G}_d , we now have the diffusion velocity $\tilde{\mathbf{v}}_D$. It's effect can be more easily understood in the case of non-complex wave functions. When a walker approaches a node, it will be carried away by the growing drift velocity, since Ψ_T approaches zero. Thus, the walker will avoid the node, without having to change "it's sign", and fixed-node approximation will be enhanced (this process is much less clearly visualized in the case of complex wave functions).

However, the Green's function given by the equation (2.53) is only approximative. Close to a singularity in the potential or to a nodal surface the drift velocity, and the local energy may even diverge. The resulting bias can then be significant[105]. The simplest remedy is to take smaller time steps, although this makes the calculation rather inefficient. A better idea due to Ceperley et al. [106], is to incorporate a Metropolis rejection step into the walkers dynamic. Here we generalize it in the case of complex wave functions. Since the exact Green's functions G and \tilde{G} satisfy

following relations

$$\begin{aligned} G(\mathbf{R}\mathbf{R}', \tau) &= G^*(\mathbf{R}'\mathbf{R}, \tau) \\ \tilde{G}(\mathbf{R}\mathbf{R}', \tau) &= \Psi_T^{-1}(\mathbf{R})G(\mathbf{R}\mathbf{R}', \tau)\Psi_T(\mathbf{R}'), \end{aligned} \quad (2.55)$$

we obtain

$$\tilde{G}(\mathbf{R}\mathbf{R}', \tau)|\Psi_T(\mathbf{R}')|^2 = \tilde{G}(\mathbf{R}'\mathbf{R}, \tau)|\Psi_T(\mathbf{R})|^2, \quad (2.56)$$

which is a detailed balance equation. We can then define an acceptance probability in terms of the approximative Green's function as given in equation (2.53):

$$A(\mathbf{R}'\mathbf{R}) \leq \text{Min} \left(1, \frac{\tilde{G}_d(\mathbf{R}'\mathbf{R}, \tau)|\Psi_T(\mathbf{R})|^2}{\tilde{G}_d(\mathbf{R}\mathbf{R}', \tau)|\Psi_T(\mathbf{R}')|^2} \right). \quad (2.57)$$

which can be implemented by a Metropolis algorithm, and guarantees the correct sampling regardless of the size of the time step. Note that, if we do not include birth/dead algorithm *i.e.* completely ignore \tilde{G}_b , we simply recover VQMC algorithm with $T_0 = \tilde{G}_d$.

2.6.2 Calculation of expectation values

How do we retrieve information about expectation values from the walkers? Let's first consider the energy:

$$E = \frac{\langle \Phi_0 | \hat{H} | \Phi_0 \rangle}{\langle \Phi_0 | \Phi_0 \rangle} \quad (2.58)$$

$$= \lim_{\tau \rightarrow \infty} \frac{\langle e^{-\tau \hat{H}/2} \Psi_T | \hat{H} | e^{-\tau \hat{H}/2} \Psi_T \rangle}{\langle e^{-\tau \hat{H}/2} \Psi_T | e^{-\tau \hat{H}/2} \Psi_T \rangle} \quad (2.59)$$

$$= \lim_{\tau \rightarrow \infty} \frac{\langle e^{-\tau \hat{H}} \Psi_T | \hat{H} | \Psi_T \rangle}{\langle e^{-\tau \hat{H}} \Psi_T | \Psi_T \rangle} \quad (2.60)$$

$$= \lim_{\tau \rightarrow \infty} \frac{\langle \Phi_0 | \hat{H} | \Psi_T \rangle}{\langle \Phi_0 | \Psi_T \rangle} \quad (2.61)$$

$$\approx \frac{1}{M} \sum_m^M E_L(\mathbf{R}_m), \quad (2.62)$$

where R_m is the M samples of $f(\mathbf{R}, \infty)$ resulting from the DQMC run. If the trial wave has the right phase (or node for real wave functions), this would give the exact ground state energy. But, in practice, the exact nodal or phase surfaces are unknown,

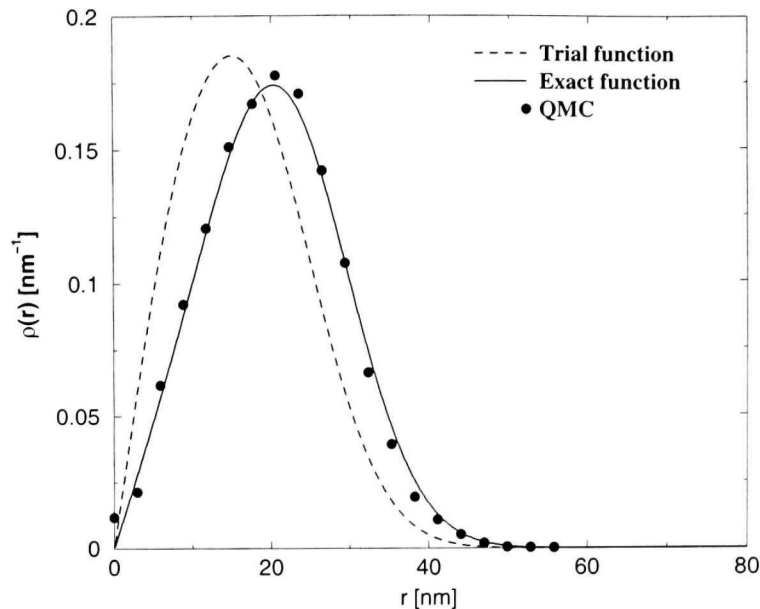


Figure 2.4: Comparison of many-body density for a 4 electron QD, $(L, 2S_z) = (3, 2)$, obtained by DQMC and exact diagonalization.

so that the equation 2.62 gives an upper bound on the exact ground state energy. The error induced by the fixed-node approximation is typically 5% of the correlation energy[29].

The above formula can also be used to calculate the quantities which commute with the Hamiltonian. But in general, for all other quantities, we must do a first order approximation to Φ_0 , which gives[29]

$$\langle \hat{S} \rangle \approx 2 \frac{\langle \Phi_0 | \hat{S} | \Psi_T \rangle}{\langle \Phi_0 | \Psi_T \rangle} - \frac{\langle \Psi_T | \hat{S} | \Psi_T \rangle}{\langle \Psi_T | \Psi_T \rangle} + O [(\Phi_0 - \Psi_T)^2], \quad (2.63)$$

often called extrapolated estimator. Here, \hat{S} is an operator of interest. Its accuracy depends on the trial wave function. As an example, we plot in Fig.(2.4) the radial density of a 4 electron quantum dot system with 1 spin-up electron. The trial state is obtained by a non-interacting electron determinant. The result obtained using equation (2.63), and compared to the exact result which is in good agreement with the extrapolated result. Exact results were calculated using the equation(2.27). All results are “self-normalized” during the calculations, so that no fitting was done after the data were obtained. The good agreement between two results gives us

confidence about our calculations since the two approaches are completely different from numerical point of view. More detailed comparison between the exact and DQMC results will be seen in chapter 5.

2.6.3 Spin

So far, we did not tell how to take into account the spin dependency of trial functions. However, as we will show now, there is a tricky way of incorporating spin into calculations which makes the QMC algorithm even faster without extra complications.

Suppose, we want to calculate the expectation value of a *spin-independent* operator $\hat{O}(\mathbf{R})$:

$$\langle \hat{O}(\mathbf{R}) \rangle = \frac{\sum_{\mathbf{s}} \int d\mathbf{R} \Psi^*(X) \hat{O}(\mathbf{R}) \Psi(X)}{\sum_{\mathbf{s}} \int d\mathbf{R} \Psi^*(X) \Psi(X)} \quad (2.64)$$

with, $X = (\mathbf{x}_1, \dots, \mathbf{x}_N)$, and $\mathbf{x}_i = (\mathbf{r}_i, s_i)$. Since $\hat{O}(\mathbf{R})$ does not depend on the spin states, the integral over \mathbf{R} must give the same value for any set of $\mathbf{s} = (s_1, \dots, s_N)$ for which Ψ is non-zero:

$$\left[\int d\mathbf{R} \Psi^*(X) \hat{O}(\mathbf{R}) \Psi(X) \right]_{\mathbf{s}} = \left[\int d\mathbf{R} \Psi^*(X) \hat{O}(\mathbf{R}) \Psi(X) \right]_{\mathbf{s}'} \quad (2.65)$$

To see why, let's look at a simple example of 2 spin-down and 1 spin-up electrons, and consider $\mathbf{s} = (\downarrow, \uparrow, \downarrow)$. Permutation symmetry of particles allows us to write

$$\begin{aligned} & \int d\mathbf{R} \Psi^*(\mathbf{r}_1 \downarrow, \mathbf{r}_2 \uparrow, \mathbf{r}_3 \downarrow) \hat{O}(\mathbf{R}) \Psi(\mathbf{r}_1 \downarrow, \mathbf{r}_2 \uparrow, \mathbf{r}_3 \downarrow) \\ &= \int d\mathbf{R} \Psi^*(\mathbf{r}_2 \uparrow, \mathbf{r}_1 \downarrow, \mathbf{r}_3 \downarrow) \hat{O}(\mathbf{R}) \Psi(\mathbf{r}_2 \uparrow, \mathbf{r}_1 \downarrow, \mathbf{r}_3 \downarrow) \end{aligned}$$

which gives

$$= \int d\mathbf{R} \Psi^*(\mathbf{r}_1 \uparrow, \mathbf{r}_2 \downarrow, \mathbf{r}_3 \downarrow) \hat{O}(\mathbf{R}) \Psi(\mathbf{r}_1 \uparrow, \mathbf{r}_2 \downarrow, \mathbf{r}_3 \downarrow), \quad (2.66)$$

since \mathbf{r}_i 's are dummy integral variables and the observable \hat{O} is symmetric with respect to exchange of electrons. We can repeat this process (collect all spin-up electrons as the first arguments), for any \mathbf{s} configuration having 1 spin-up and 2 spin-down electrons, and we will always obtain the same integral. Consequently, we can drop the sums over spins as well as spin variables (but keeping in mind that first arguments

corresponds to spin up electrons):

$$\langle \hat{O}(\mathbf{R}) \rangle = \frac{\int d\mathbf{R} \Psi^*(\mathbf{R}) \hat{O}(\mathbf{R}) \Psi(\mathbf{R})}{\int d\mathbf{R} \Psi^*(\mathbf{R}) \Psi(\mathbf{R})}. \quad (2.67)$$

This is equivalent to treating spin-up electrons distinguishable from spin-down electrons, *i.e.* there is no specific symmetry on exchange of the spatial coordinates of electrons with different spin. Therefore in QMC calculations one usually express the trial waves as a product of determinants of spin-up and spin-down electrons[29]:

$$\Psi_T(\mathbf{R}) = D^\uparrow(\mathbf{r}_1, \dots, \mathbf{r}_{N_\uparrow}) D^\downarrow(\mathbf{r}_{N_\uparrow+1}, \dots, \mathbf{r}_N), \quad (2.68)$$

such that a large determinant is now replaced by two smaller ones. This, of course, guarantees to give the right expectation value for spin-independent operators.

2.6.4 DQMC algorithm

Most important steps of a fixed-phase DQMC algorithm can be summarized as follows [29]:

- (1) Choose a “good” trial function Ψ_T (from Hartree-Fock, density functional theory etc.).
- (2) Initialize walkers position sampled from $|\Psi_T|^2$ using VQMC.
- (3) For each walker, propose a move using $\mathbf{R}' = \mathbf{R} + \chi + \tau \mathbf{v}_D(\mathbf{R})$, where χ is a $3N$ dimensional vector of normally distributed numbers with variance τ and zero mean.
- (3) Accept the move with probability given by equation (2.57).
- (4) For each walker, calculate the number of copies that will continue in the evolution given by $\text{INT}(u + G_b)$, where u is a uniform random number.
- (5) Occasionally adjust E_T using $E_T^{\text{new}} = E_T^{\text{old}} + \kappa \ln(P_0/P)$.
- (6) Accumulate the quantities of interest.
- (7) Repeat steps 3-6 until convergence is reached.

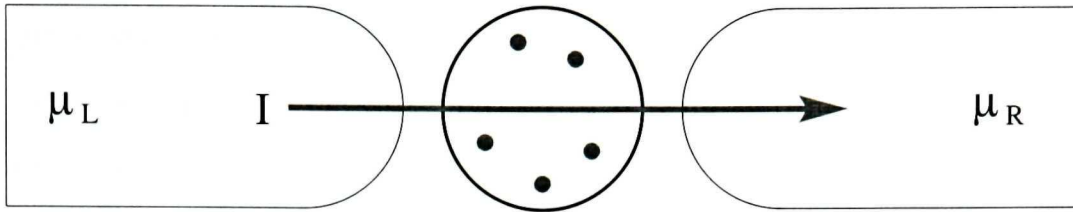


Figure 2.5: Schematic diagram of the experimental transport configuration.

2.7 Quantum transport

So far we were only concerned about closed systems. However, interesting phenomena arise when these systems are coupled to the leads, as schematized in Fig.(2.5): The interacting region is coupled to two metallic multichannel leads where the electrons are not interacting. This problem can be studied by first considering unperturbed system which consists of three uncoupled regions: left lead, right lead and the interacting region. Then we let the coupling turn on, and calculate the current when the system reaches the steady state. Keldysh Green's function formalism is well suited to study this situation, and we will now give a short review of this formalism.

2.7.1 Keldysh Green's function formalism

Keldysh Green's function formalism is particularly useful for describing nonequilibrium quantum transport, allowing us to deal with expectation values such as $\langle \hat{a}_i^\dagger \hat{a}_j \rangle$ in the presence of interactions. In the following, we give a brief description of Green's functions and we point out some of their important properties. A detailed formal discussion of Green's functions can be found in Ref.[107], while application of Keldysh Green's functions to transport problems in solid state physics is discussed in Ref.[108].

The electron Green's function is defined by

$$G_{ij}(t_1, t_2) = i \langle \hat{T} \hat{a}_i^\dagger(t_1) \hat{a}_j(t_2) \rangle, \quad (2.69)$$

where \hat{T} is the time-ordering operator, and bracket $\langle \rangle$ may represent ground state expectation value (at zero temperature) or a thermodynamic average over ground and excited states (at finite temperature). In nonequilibrium situations, *i.e.* while

the state $t = -\infty$ is described as the ground state of the unperturbed system, the state $t = \infty$ is not well defined since the perturbations remains on. A method for handling the asymptotic limit $t = \infty$, is to consider a new time axis, so called complex-time contour, for which the time variable τ goes from $t = -\infty$ to the point of interest t_0 , then goes back from $t = t_0$ to $t = -\infty$. In Keldysh Green's function formalism, using the complex-time contour $G_{ij}(t_1, t_2)$ can equivalently be defined through the following Green's functions:

$$\begin{aligned}
G_{ij}^<(t_1, t_2) &= i\langle \hat{a}_j^\dagger(t_2) \hat{a}_i(t_1) \rangle \\
G_{ij}^>(t_1, t_2) &= -i\langle \hat{a}_i(t_1) \hat{a}_j^\dagger(t_2) \rangle \\
G_{ij}^r(t_1, t_2) &= -i\Theta(t_1 - t_2) \langle \{ \hat{a}_i(t_1), \hat{a}_j^\dagger(t_2) \} \rangle \\
G_{ij}^a(t_1, t_2) &= i\Theta(t_2 - t_1) \langle \{ \hat{a}_i(t_1), \hat{a}_j^\dagger(t_2) \} \rangle.
\end{aligned} \tag{2.70}$$

Last two Green's functions are the familiar retarded and advanced Green's functions. Now, let's consider a system for which Green's functions are known, denoted as g . If we turn on some interaction terms in the Hamiltonian, the Green's function G of the system including the interactions can be described in terms of g by using *Dyson equation*, $G = g + g\Sigma G$, which gives[109]

$$\begin{aligned}
G^{r/a} &= g^{r/a} + g^{r/a}\Sigma^{r/a}G^{r/a} \\
G^{</>} &= [1 + G^r\Sigma^r]g^{</>}[1 + G^a\Sigma^a] + G^r\Sigma^{</>}G^a,
\end{aligned} \tag{2.71}$$

where $\Sigma^{r/a}$ represents interactions inside the system, while $\Sigma^{</>}$ describes how the system interacts with the outside world. They can be calculated in terms of diagrams or using equation of motion method[75]. The double products in the equations above may imply multiple integration on $d\mathbf{r}$ and dt depending on a chosen representation. In steady state problems, the Green's functions depend only on the difference between two times, and can be Fourier transformed:

$$G_{ij}(\omega) = \int dt e^{i\omega t} G_{ij}(t, 0). \tag{2.72}$$

When expressed in energy representation, the equations (2.71) are just algebraic equations.

2.7.2 Calculation of current

In order to calculate the transport properties of the system shown in Fig.(2.5), we start with the following model Hamiltonian:

$$\hat{H} = \hat{H}_{IS} + \hat{H}_{leads} + \hat{H}_T, \quad (2.73)$$

where \hat{H}_{IS} , \hat{H}_{leads} , and \hat{H}_T represent the Hamiltonian of the interacting system, leads, and tunneling between them, respectively. They can be expressed as

$$\begin{aligned} \hat{H}_{IS} &= \sum_j \epsilon_j \hat{a}_j^\dagger \hat{a}_j + \hat{H}_{int} \\ \hat{H}_{leads} &= \sum_{k\sigma} \epsilon_{k\sigma}^L \hat{c}_{Lk\sigma}^\dagger \hat{c}_{Lk\sigma} + \sum_{k\sigma} \epsilon_{k\sigma}^R \hat{c}_{Rk\sigma}^\dagger \hat{c}_{Rk\sigma} \\ \hat{H}_T &= \sum_{kj\sigma} (t_{kj\sigma}^L \hat{c}_{Lk\sigma}^\dagger \hat{a}_j + t_{kj\sigma}^R \hat{c}_{Rk\sigma}^\dagger \hat{a}_j + H.C.), \end{aligned} \quad (2.74)$$

where $\hat{c}_{Lk\sigma}$ destroys an electron with momentum k and spin σ in the left (L) lead. Reservoirs representing left and right leads are described by Fermi-Dirac statistics, and are assumed to be large enough that their bulk chemical potentials μ_L and μ_R are not perturbed by the current.

In the noninteracting case, the transport problem was solved by Landauer[108], by expressing the current in terms of local properties of the finite region (such as the transmission coefficient) and the distribution functions in connected reservoirs. Here we follow the formalism developed by Meir and Wingreen [77], which generalizes Landauer's current formula for strongly correlated systems. The current I_α can be calculated by "counting" the electrons in the left ($\alpha = L$) or right ($\alpha = R$) lead:

$$I = -e \left\langle \frac{d\hat{N}_\alpha}{dt} \right\rangle = \frac{ie}{\hbar} \left\langle \left[\sum_{k\sigma} \hat{c}_{\alpha k\sigma}^\dagger \hat{c}_{\alpha k\sigma}, \hat{H} \right] \right\rangle \quad (2.75)$$

$$= \frac{ie}{\hbar} \sum_{kj\sigma} (t_{kj\sigma}^\alpha \langle \hat{c}_{\alpha k\sigma}^\dagger \hat{a}_j \rangle - t_{kj\sigma}^{\alpha*} \langle \hat{a}_j^\dagger \hat{c}_{\alpha k\sigma} \rangle). \quad (2.76)$$

This quantity can be worked out using the definitions of Green's functions given in equation (2.70), and Dyson equation, which gives[77]

$$I = -\frac{2e}{\hbar} \text{Im} \left\{ \int \frac{d\epsilon}{2\pi} \sum_{ij} \Gamma_{ij}^\alpha(\epsilon) [f_\alpha(\epsilon) G_{ij}^r(\epsilon) + \frac{1}{2} G_{ij}^<(\epsilon)] \right\}, \quad (2.77)$$

where f_α is the Fermi-Dirac distribution of the leads, and $\Gamma_{ij}^\alpha(\epsilon)$ is a coupling parameter defined by $2\pi \sum_k t_{ki\sigma}^{\alpha*} t_{kj\sigma}^\alpha \delta(\epsilon - \epsilon_{k\alpha})$. If we assume that $\Gamma_{ij}^L(\epsilon)$ is proportional to

$\Gamma_{ij}^R(\epsilon)$ we obtain a simpler expression[72]:

$$I = -\frac{2e}{\hbar} \int \frac{d\epsilon}{2\pi} [f_L(\epsilon) - f_R(\epsilon)] \text{Im} \left\{ \sum_{ij} \Gamma_{ji} G_{ij}^r \right\}, \quad (2.78)$$

where $\Gamma \equiv \Gamma^L \Gamma^R / (\Gamma^L + \Gamma^R)$. It should be emphasized that this innocent looking formula is the central result of this quantum transport formalism, and includes, by means of the full Green's function G^r , effect of leads, electron-electron interactions, spin flips, inelastic processes, etc. The evaluation of G^r for a given system is the most critical and difficult part of the calculations, and one must do appropriate approximations in order to include correlation effects.

2.7.3 Transport through a N -body system

Let's now assume that we have solved the N -body problem for an isolated system, by exact diagonalization or DQMC method. How can we evaluate the current as given in equation (2.78)? Starting point is Dyson equation, which express G^r as a function of the unperturbed Green's function g of the isolated system which includes electron-electron interactions:

$$G^r(\epsilon) = \frac{1}{g^{r-1}(\epsilon) - \Sigma^r(\epsilon)}, \quad (2.79)$$

with $\Sigma_{ij}^r = -\frac{i}{2} \Sigma_\alpha \Gamma_{ij}^\alpha$, when matrix elements are restricted to interacting system levels \hat{a}_i [75]. We must now calculate $g_{ij}^r(\epsilon) = \int dt e^{i\epsilon t} g_{ij}^r(t)$, with

$$g_{ij}^r(t) = -i\Theta(t) \langle \{ \hat{a}_i(t), \hat{a}_j^\dagger(0) \} \rangle. \quad (2.80)$$

In order to include finite temperature effects inside the system, we must average over all possible states. Denoting $P(NJ)$ as the probability of finding a N -body state which is at it's J^{th} eigenstate, we have

$$\begin{aligned} g_{ij}^r(t) &= -i\Theta(t) \sum_{NJ} P(NJ) \langle NJ | \hat{a}_i(t) \hat{a}_j^\dagger(0) + \hat{a}_j^\dagger(t) \hat{a}_i(t) | NJ \rangle \\ &= -i\Theta(t) \sum_N \sum_{JJ'} P(NJ) \{ \langle NJ | \hat{a}_i(t) | N+1J' \rangle \langle N+1J' | \hat{a}_j^\dagger(0) | NJ \rangle \\ &\quad + \langle NJ | \hat{a}_j^\dagger(0) | N-1J' \rangle \langle N-1J' | \hat{a}_i(t) | NJ \rangle \}, \end{aligned}$$

keeping in mind that $a_i|0\rangle = 0$. Then, by explicitly writing time dependency of the operators, it is straightforward to show that

$$g_{ij}^r(t) = -i\Theta(t) \sum_N \sum_{JJ'} [P(NJ) + P(N-1J')] e^{-i(E_{NJ} - E_{N-1J'})t} \Delta_{ij}(N), \quad (2.81)$$

where E_{NJ} are the eigenenergies controlled by a gate voltage V_g as $E_{NJ} = E_{NJ}^0 - NeV_g$, and

$$\Delta_{ij}(N) \equiv \langle NJ | a_j^\dagger | N-1J' \rangle \langle N-1J' | a_i | NJ \rangle. \quad (2.82)$$

We can now take the Fourier transform to calculate $g_{ij}^r(\epsilon)$, which gives

$$g_{ij}^r(\epsilon) = \sum_N \sum_{JJ'} \frac{1}{\epsilon - E_{NJ} + E_{N-1J'} + i0^+} [P(NJ) + P(N-1J')] \Delta_{ij}(N). \quad (2.83)$$

It is then possible to get $G^r(\epsilon)$ by matrix inversion using equation (2.79). However according to equation (2.78), $G^r(\epsilon)$ must be integrated, where each integration point requires a matrix inversion. Moreover, this process must be repeated for several values of voltages V_g and temperature T in order to get complete current-voltage characteristics of the system, which makes the calculations even more complex. Thus, in the following, we will take

$$G^r(\epsilon) \approx g^r(\epsilon). \quad (2.84)$$

This approximation means that we are neglecting the broadening of the levels due to the coupling with the leads, which remains true as far as $k_B T \gg \Gamma$. Then, integration over ϵ can be evaluated analytically to give

$$I = \frac{e}{\hbar} \sum_N \sum_{JJ'} \sum_{ij} [f_L(E_{NJ} - E_{N-1J'}) - f_R(E_{NJ} - E_{N-1J'})] \times \Gamma_{ji} [P(NJ) + P(N-1J')] \Delta_{ij}(N). \quad (2.85)$$

This expression is a product of four terms. The first one describes the state of the leads. The second one is the coupling term between the leads and the interacting region. The third term is the thermodynamic probability of a given couple of many-body states in the interacting region to participate to the transport. They can be calculated from grand canonical ensemble given by $P(NJ) = \exp(-(E_{NJ} - N\mu)/k_B T)/Z$ when we are in the linear-response regime, that is in the limit of zero bias voltage.

But, in order to study finite bias effects they must be calculated from detailed balance equations that we will study in section 2.7.5. The last term, called *spectral function*, is an overlap between N and $N - 1$ states, giving the transition probability between two states due to many-body correlations. It is responsible for new physical effects in quantum dots presented in in chapter 4.

2.7.4 Calculation of spectral function

The calculation of the spectral function $\Delta_{ij}(N)$ is very important to us, since it contains most of the many-body phenomena that occurs during quantum transport. When $|NJ\rangle$ and $|N-1J'\rangle$ are single Slater determinants, the product $\langle N-1J'|\hat{a}_i|NJ\rangle$ is simply 1 or 0. However, a strongly correlated system cannot be described by a single determinant, and $\Delta_{ij}(N)$ can take any value between 0 and 1. It's calculation is easy if exact wave functions are given in the second quantized language *i.e.* by exact diagonalization.

As spectral function directly reflects many-body correlations in wave functions, an interesting and very important question is whether it is possible to evaluate $\Delta_{ij}(N)$ by DQMC method. This is less trivial than using exact diagonalization for several reasons. First of all, calculations must be restricted to ground states since in general excited states cannot be studied by DQMC. Also, as DQMC calculations are done in first-quantized notation and calculation of spectral function requires mapping between N and $N - 1$ electron Hilbert spaces, we must establish a connection between the two formalisms. A more fundamental problem is the fact that DQMC is based on fixed-phase approximation. While this approximation gives very accurate total energy or electronic density, it is not clear how it would affect the calculation of spectral function where the relative phase of different Slater determinants plays an important role. Moreover, in the DQMC, quantities which do not commute with the Hamiltonian can only be evaluated up to second order. In the following we suggest a possible way of calculating the spectral function by DQMC, in the spirit of extrapolated estimators of equation (2.63).

In DQMC, N -body ground state wave function can be written as

$$|\Phi(N) = c_T|\Psi_T(N)\rangle + c_\epsilon|\epsilon(N)\rangle. \quad (2.86)$$

For a good trial wave function $|\Psi_T(N)\rangle$, we have $c_T \approx 1 - \frac{1}{2}c_\epsilon^2$. We have then three way to approximate $\langle\Phi(N-1)|\hat{a}_i|\Phi(N)\rangle$ up to second order:

$$\begin{aligned} (1) \quad & \langle\Phi(N-1)|\hat{a}_i\Psi_T(N)\rangle + c_\epsilon(N)\langle\Phi(N-1)|\hat{a}_i\epsilon(N)\rangle \\ (2) \quad & \langle\hat{a}_i^\dagger\Psi_T(N-1)|\Phi(N)\rangle + c_\epsilon(N-1)\langle\hat{a}_i^\dagger\epsilon(N-1)|\Phi(N)\rangle \\ (3) \quad & \langle\Psi_T(N-1)|\hat{a}_i|\Psi_T(N)\rangle + c_\epsilon(N)\langle\Psi_T(N-1)|\hat{a}_i|\epsilon(N)\rangle \\ & + c_\epsilon(N-1)\langle\epsilon(N-1)|\hat{a}_i|\Psi_T(N)\rangle. \end{aligned}$$

By adding (1) and (2), then subtracting (3), we can eliminate first order terms. We finally obtain

$$\begin{aligned} \langle\Phi(N-1)|\hat{a}_i|\Phi(N)\rangle & \approx \frac{\langle\Phi(N-1)|\hat{a}_i\Psi_T(N)\rangle}{\langle\Phi(N-1)|\Psi_T(N-1)\rangle} + \frac{\langle\hat{a}_i^\dagger\Psi_T(N-1)|\Phi(N)\rangle}{\langle\Psi_T(N)|\Phi(N)\rangle} \\ & - \langle\Psi_T(N-1)|\hat{a}_i|\Psi_T(N)\rangle + O(c_\epsilon^2(N) + c_\epsilon^2(N-1) + c_\epsilon(N)c_\epsilon(N-1)). \end{aligned}$$

The first two terms at the right side of the equation can be evaluated by running $(N-1)$ and N -electron DQMC simulations respectively. Third term is the spectral function of the trial wave functions. While this equation seems plausible, our calculations show that the error generated is too high, sometimes giving unphysical results such as $\Delta_{ij}(N)$ higher than 1 or lower than 0, perhaps due to fixed-phase approximation and quality of the trial wave functions. Adding a Jastrow factor [29] to the trial wave function might help to improve the results, although this would make the calculation rather complicated. Thus, in this thesis we will only use exact diagonalization wave functions in order to calculate the spectral function. So far there is no quantum transport calculation based on DQMC in literature, and further investigations are necessary.

2.7.5 Detailed balance equations

If we assume that there is no phase coherence between the dot and the leads ($k_B T \gg \Gamma^L, \Gamma^R$), and provided that inelastic scattering in the interacting region is negligible

(an electron cannot change its state for instance, by phonon emission), steady-state occupations $P(NJ)$ of the many-body states are determined by the statistics of the leads, and can be calculated using a set of detailed balance equations [78, 110] :

$$\begin{aligned}
& \sum_{J'} P(NJ) \{ \Gamma^L [1 - f_L(E_{NJ} - E_{N-1J'})] + \Gamma^R [1 - f_R(E_{NJ} - E_{N-1J'})] \} \\
& \quad = \sum_{J'} P(N-1J') \{ \Gamma^L f_L(E_{NJ} - E_{N-1J'}) + \Gamma^R f_R(E_{NJ} - E_{N-1J'}) \}, \\
& \sum_J P(NJ) \{ \Gamma^L [1 - f_L(E_{NJ} - E_{N-1J'})] + \Gamma^R [1 - f_R(E_{NJ} - E_{N-1J'})] \} \\
& \quad = \sum_J P(N-1J') \{ \Gamma^L f_L(E_{NJ} - E_{N-1J'}) + \Gamma^R f_R(E_{NJ} - E_{N-1J'}) \},
\end{aligned} \tag{2.87}$$

where we have assumed constant couplings Γ^L, Γ^R . These equations form a system of linear homogeneous equations, and they are satisfied by following equation:

$$\gamma_1 P(NJ) = \gamma_2 P(N-1J'), \tag{2.88}$$

where

$$\begin{aligned}
\gamma_1 & \equiv f_L + \frac{\Gamma_L}{\Gamma_R} f_R \\
\gamma_2 & \equiv 1 - f_L + \frac{\Gamma_L}{\Gamma_R} (1 - f_R)
\end{aligned}$$

which must be solved using the conservation of probability, $\sum_{NJ} P(NJ) = 1$.

It can be verified that, in the special cases of linear transport regime $\mu_L = \mu_R$, or when $\Gamma^L \gg \Gamma^R$, these equations give $P(NJ) = \exp(-(E_{NJ} - N\mu_L)/k_B T)/Z$ as expected.

2.8 Summary

In this chapter, we discussed in detail several techniques which will allow us to investigate strongly correlated quantum dot systems. Exact diagonalization and quantum Monte Carlo methods are valuable numerical techniques based on first principles, and each has its own advantage and inconvenience. With exact diagonalization method, it is possible to obtain very accurate eigenfunctions and eigenenergies for both ground state and excited states. But it suffers from computational limitations for large number of electrons and for systems that do not have good symmetry properties. On the

other hand, quantum Monte Carlo technique can be applied to larger systems with arbitrary geometry for an accurate calculation of ground state energy provided that a good trial function is available, while it cannot give complete information about wave functions. For open systems, we have seen that Keldysh Green's functions formalism can be used to calculate current-voltage characteristics of the interacting region, including the effects of strong correlations through spectral function. In the following chapters, we will apply these techniques to several quantum dot systems to investigate their electronic structure and transport properties.

Perfectly Parabolic Quantum Dots

3.1 Introduction

This chapter is devoted to the study of cylindrical quantum dots with harmonic confinement potential by exact diagonalization. We also introduce Fock-Darwin states which form single-electron basis set used in most of the numerical calculations performed in this thesis, as well as in the quantum dot literature. Exact diagonalization allows us to calculate exactly the spectral function that contains all the correlation effects in a tunneling experiment. In section 3.2, we present our model Hamiltonian matrix which consist of a parabolic confinement in xy plane, a quantum well and external magnetic field in z -direction. The solutions to the parabolic confinement with the magnetic field are called Fock-Darwin states, from which we build Slater determinants used to construct the many-body Hamiltonian matrix. In section 3.3, we present and discuss the results: the addition spectrum of a quantum dot is calculated and compared to the experimental result of Fig.1.4. We then study transport properties as a function of magnetic field, by combining exact diagonalization results with the current equation derived in previous chapter using Keldysh Green's function formalism. We also study the effect of degeneracy on transport properties in the absence of magnetic field.

3.2 Fock-Darwin basis set

In most of the experimental situations, especially for very small dots, the confinement potential of the quantum dot can be approximated by a 2D-harmonic potential. When

an external magnetic field B is applied perpendicular to the harmonic confinement plane, single-electron Hamiltonian can be written as

$$\hat{H}_0 = \frac{1}{2m^*} \left(\mathbf{p} - \frac{e}{c} \mathbf{A}(\mathbf{r}) \right)^2 + \frac{1}{2} m^* \omega_0^2 \mathbf{r}^2 + g^* \mu_B B s_z + V_w(z), \quad (3.1)$$

with $\mathbf{A} = \frac{1}{2}(-Br_x, Br_y, 0)$, $e < 0$, and $\mathbf{r} = (r_x, r_y)$. V_w represents a narrow quantum well whose thickness is typically much smaller than the lateral confinement such that only its lowest level is taken into account. The parabolicity of the lateral confinement is characterized by the parameter ω_0 . g^* is an effective Landé factor depending on the material. The solutions to the parabolic confinement part of this Hamiltonian are called *Fock-Darwin states*, and were studied well before quantum dots were invented, by Fock[111] in 1928, and by Darwin[112] in 1930. The Fock-Darwin wave functions are given by

$$\varphi(r, \theta) = K e^{-im\theta} r^{|m|} L_n^{|m|} \left(\frac{r^2}{2l^2} \right) e^{-\frac{r^2}{4l^2}}, \quad (3.2)$$

with

$$\begin{cases} K = \left(\frac{n!}{2\pi l^2 2^{|m|} (n+|m|)!} \right)^{\frac{1}{2}} \\ a^2 = \frac{\hbar}{m^*} (\omega_c^2 + 4\omega_0^2)^{-1/2} \\ \omega_c = \frac{eB}{m^*} \end{cases} \quad (3.3)$$

and $L_n^{|m|}$ are associated Laguerre polynomials. The quantum numbers associated with the Fock-Darwin states are angular momentum m ($-\infty \rightarrow \infty$) and Landau level index n ($0 \rightarrow \infty$). The eigenenergies are given by

$$E_{nm} = (2n + |m| + 1) \left(\frac{1}{4} \omega_c^2 + \omega_0^2 \right)^{\frac{1}{2}} \hbar - \frac{1}{2} m \hbar \omega_c. \quad (3.4)$$

This energy spectrum reveals very interesting features (see Fig. 3.1). Near zero magnetic field, we observe closed-shell structure resulting from the two-dimensionality of the circular confinement. At 2, 6, 12... electron numbers, we would expect a stable electronic configuration. The stability of closed-shell structure against disorder will be studied in detail in chapter 6. At high magnetic fields, negative angular momentum levels are suppressed, effect of spatial confinement is reduced, and we can clearly distinguish different Landau levels.

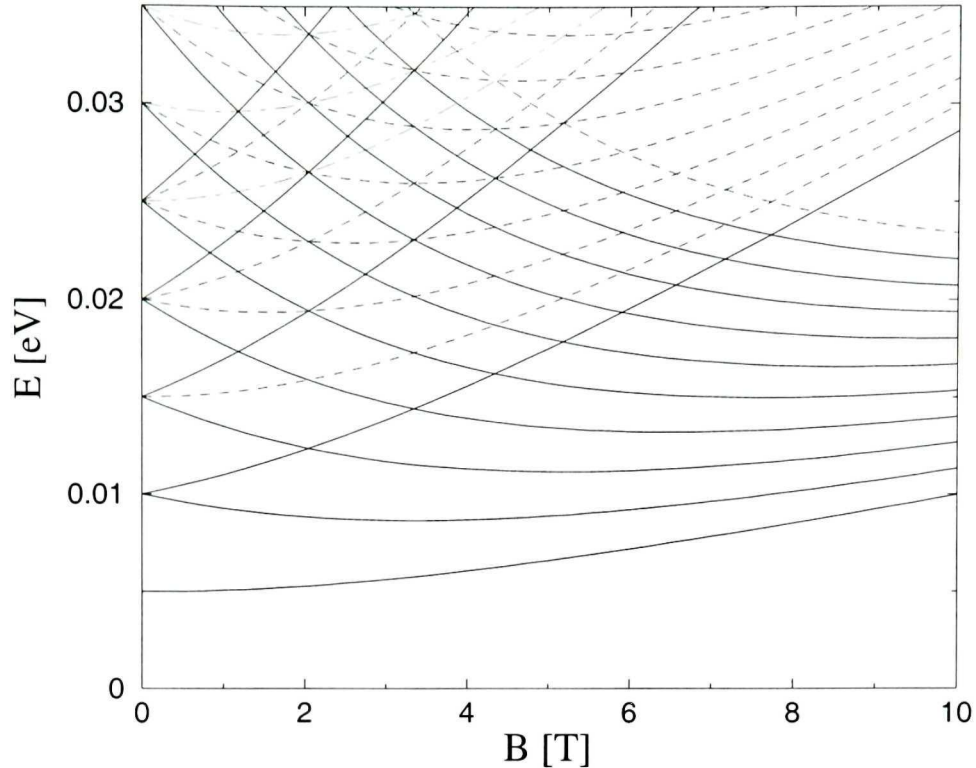


Figure 3.1: Fock-Darwin energy spectrum as a function of magnetic field. Different line styles correspond to different Landau levels. Confinement potential strength $\hbar\omega_0$ is fixed to 5 meV.

3.3 Results

3.3.1 Addition spectrum

Addition spectra such as in Fig.(1.4) can be studied by calculating the difference in total energy $E(N + 1) - E(N)$ of the ground states. This corresponds to the chemical potential $\mu(N)$ of a given N -electron quantum dot. In Fig.(3.2), we present the addition spectrum of a quantum dot with $\hbar\omega_0 = 5.4$ meV. We have used material parameters of GaAs ($m^* = 0.067m_0$, $\epsilon_r = 13.1$, $g^* = 0.52$). While it is known that the value of g^* can vary by many orders of magnitude depending on the size, and temperature of the QD, there is no satisfactory theory for predicting its value. Thus, the value of g^* used here corresponds to the experimental bulk material parameter. Numbers in parenthesis represent quantum numbers $(L, 2S_z)$ and arrows are the transition points between different many-body states. For instance, the two-electron quantum dot changes its state from $(0, 0)$ to $(1, 2)$ at $B \approx 4$ T. This is the singlet-triplet tran-

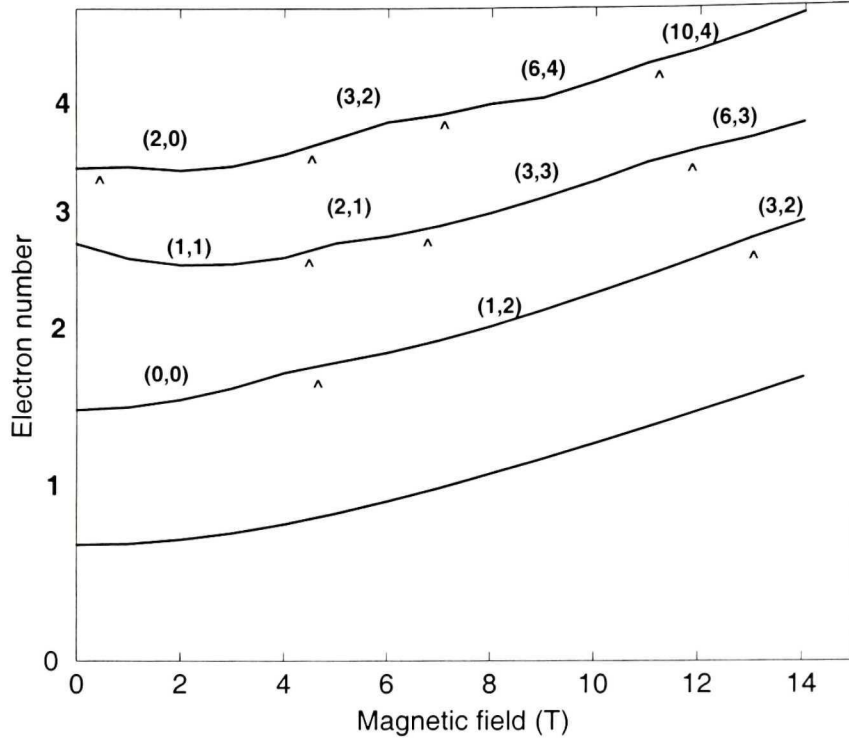


Figure 3.2: Addition spectra up to 4 electrons as calculated by exact diagonalization. Confinement potential parabolicity is $\hbar\omega_0 = 5.4$ meV. Numbers in parenthesis represent total angular momentum and total spin, $(L, 2S_z)$. Many-body transitions are shown by arrows.

sition: at low magnetic field the two electrons occupy the same spatial state. When magnetic field increases, orbitals are squeezed, energy gap between them decreases, and the overlap increases. Thus, one electron jumps to a higher orbit by gaining exchange energy. At even higher magnetic fields, the Coulomb repulsion becomes too strong and it is energetically more favorable that the center electron jumps to a larger orbit. This is also a common (but not complete) sequence of transitions for higher numbers of electrons, as naively schematized in Fig.(3.3). At low magnetic field, electrons occupy lower orbitals with total spin minimized (except at $B \approx 0$ where spin can be maximized due to Hund's rules). As magnetic field increases, system goes through a paramagnetic-ferromagnetic transition (so called “melting” process [18]), where spin flips occur until the system reaches a very stable state called “maximum density droplet” (MDD) [10]. This state can also be interpreted as the $\nu = 1$ state, familiar from quantum Hall effect: electrons occupy all the available lowest Landau levels, with their spin polarized. For higher magnetic fields, the system enter the

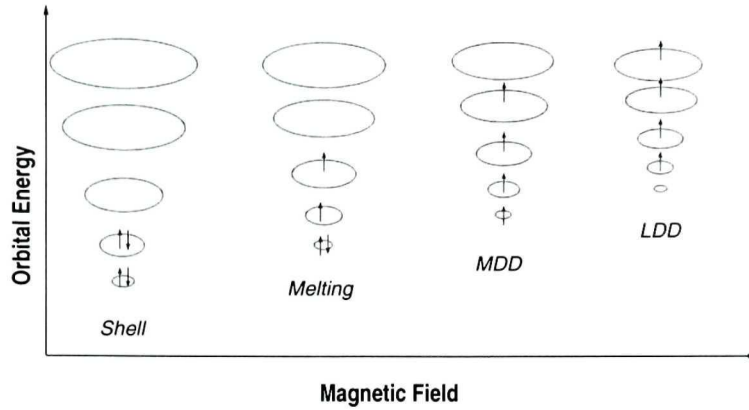


Figure 3.3: Schematic representation of magnetic field induced orbital and spin transitions.

“lower density droplet” (LDD) regime [113, 114, 115, 116, 117] experimentally observed in Ref.[10] (see Fig.(1.4)). A more detailed study of spin transitions for higher number of electrons using quantum Monte Carlo method will be done in chapter 6.

3.3.2 Spectral function and current-voltage characteristics

As discussed in chapter 2, in order to study transport properties in strongly correlated systems, we must calculate spectral function using exact diagonalization results. In QD’s with vertical geometry, the single-electron coupling terms Γ_{ij} do not depend strongly on single electron states, and for a given Coulomb peak N Eq.(2.78) gives

$$I_N = \frac{e}{\hbar} \Gamma \sum_{JJ'} [f_L - f_R] [P(NJ) + P(N - 1J')] \Delta(N), \quad (3.5)$$

with

$$\Delta(N) = \sum_{ii} \Delta_{ii}(N), \quad (3.6)$$

where we have neglected the cross terms of the overlap matrix elements $\Delta_{ii'}(N)$ which are due to the presence of second Landau level. In Fig.(3.4) we show the spectral function for a quantum dot containing up to 5 electrons, with $\hbar\omega_0 = 4$ meV. As we can see the value of the spectral function is near 1 in most of the time, but reduced for some values of magnetic field, for instance between 2.5 – 4.5 tesla: this regime correspond to the melting states, where the charge spreads over a large number of single electron

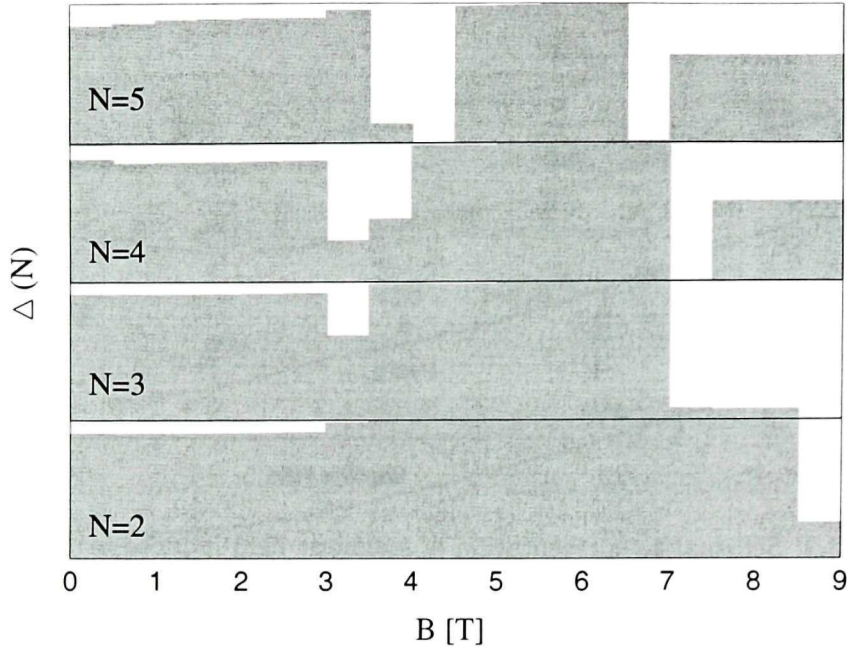


Figure 3.4: Spectral function calculated by exact diagonalization as a function of magnetic field, up to 5 electrons.

states and several spin flips occur. The overlap matrix elements between these highly correlated states is much diminished. In the maximum density droplet region, states are well described by single Slater determinants and correlation are weaker, so that overlap matrix elements approach unity. At higher magnetic fields, the MDD state breaks apart into lower density droplet (LDD), and since the transition probability is reduced between two different charge distribution, spectral function is again reduced. In some cases, the spectral function is exactly zero. This is due to the so-called *spin blockade*: in fact, when the total spins of the $(N - 1)$ - and the N -electron QD satisfy the following relation:

$$|S(N) - S(N - 1)| > \frac{1}{2} . \quad (3.7)$$

$\Delta(N)$ vanishes. In other words, it is not possible to obtain such transition by adding or removing one single electron. As verified by numerics, this happens near 4 T and 6.5 T for $N = 5$, as well as near 7 T for $N = 4$.

Fig.3.5 shows the tunnelling current I_N as a function of gate voltage V_g and magnetic field B , obtained by evaluating Eq.(2.85) using the exact overlap matrix ele-

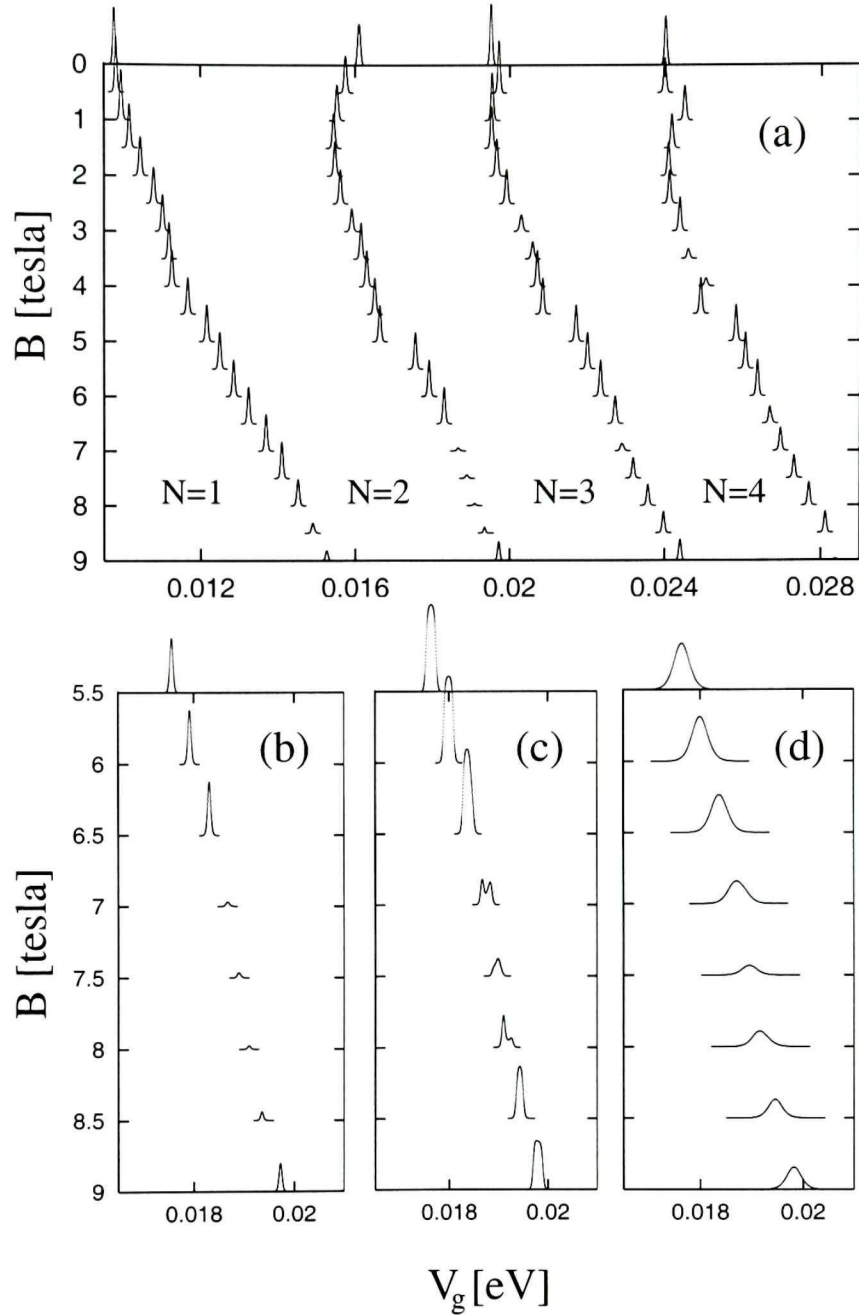


Figure 3.5: Three dimensional plot of tunnelling current I_N (arb. units) as a function of magnetic field B and gate potential V_g , for perfect quantum dot without confining potential distortion. The height of the Coulomb peaks indicate relative magnitude of the current. (a). Coulomb peaks of transitions in 2,3,4 and 5-electron QD's at bias potential $\Delta\mu = 0.05$ meV and temperature $T = 0.2$ K. (b). Emphasizing the MDD-LDD transition for $N = 3$. The effect of increasing $\Delta\mu$ to 0.2 meV and T to 1K is shown in (c) and (d) respectively.

ments. Up to 10 excited states for each electron number N were included in calculating the current, although the number of transitions significantly contributing to transport depends on applied bias voltage $\Delta\mu$ and temperature T . The estimated capacitance $C = q^2/2U$ where $U = E(N+1) - E(N)$ in constant interaction model, gives $C \approx 10$ aF. Fig.3.5(a) shows I_N at low temperature and small bias, $T = 0.2$ K and $\Delta\mu = 0.05$ meV, for which the ground state contribution to current is dominant. Clearly, there are magnetic field regions where the current is substantially suppressed as indicated in the figure by the diminishing peak heights. This is due to correlation effects which reduce the overlap matrix elements between ground states as previously discussed. In Fig.3.5(b),(c), and (d), we take a closer look to $N = 2$ to $N = 3$ transition in order to study effects of finite bias and non-zero temperature in the MDD-LDD transition regime. This transition occurs at $B \sim 7$ tesla for $N = 3$, and at $B \sim 9$ tesla for $N = 2$, resulting in a reduced current between 7 – 9 tesla (Fig.3.5(b)). When we increase the bias from 0.05 meV to 0.2 meV which makes possible transitions through excited states, two new small peaks appear (see double peak in Fig.3.5(c)). We also observe an increase of current in the MDD regime due to contributions from very close excited states. In Fig.3.5(d) we increase temperature T to 1K: the effect is to reduce the maximum current and smoothing the peaks as expected.

When the QD is asymmetrically coupled to the two leads, *i.e.* $\lambda \equiv \Gamma^L/\Gamma^R \neq 1$, an asymmetry in current flow occurs. Fig.3.6 shows the Coulomb peaks up to $N = 5$ for $B = 0$ at low temperature (0.2 K) and small bias (0.05 meV). The solid lines are current at positive bias, denoted by I_N^+ ; and dashed lines are for negative bias denoted by I_N^- (λ is set to 100). It is interesting to observe the ratio of the peak heights I_N^+/I_N^- which is 1 : 2 for $N = 1$, 2 : 1 for $N = 2$, 1 : 4 for $N = 3$, 4 : 3 for $N = 4$ and 3 : 4 for $N = 5$. This ratio directly reflects the degeneracy on the ground states. Assuming that the degeneracy of the N -electron state is g_N and neglecting the excited states, due to conservation of probability we must have

$$g_N P(N, J) + g_{N-1} P(N-1, J') = 1 \quad . \quad (3.8)$$

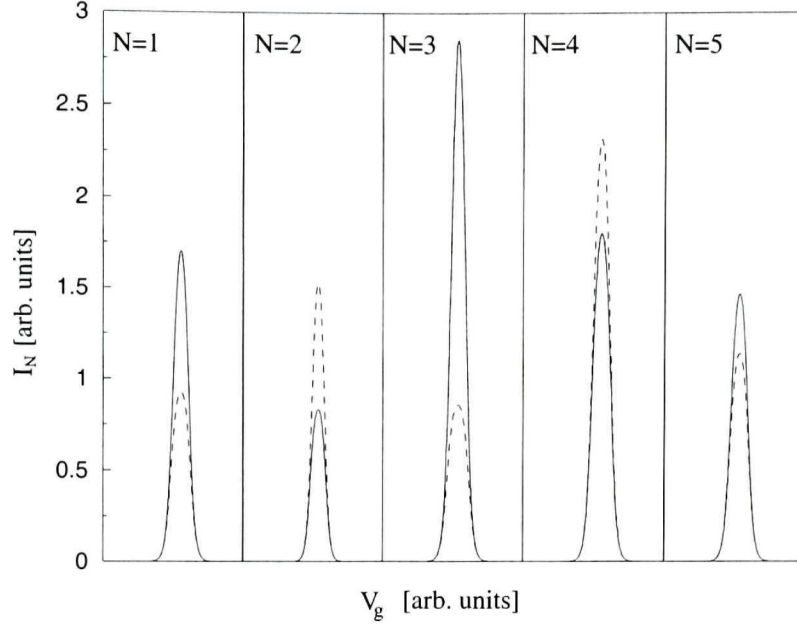


Figure 3.6: For a perfect dot with asymmetrical couplings to the two leads, this figure shows the tunnelling current as a function of gate voltage V_g for $N = 1$ to 5. Solid lines represent positive bias and dashed lines negative bias.

Combining Eq.(2.88), Eq.(3.8) and Eq.(3.5) we obtain

$$I_N = \left(\frac{e}{\hbar} \frac{\Gamma^L \Gamma^R}{\Gamma^L + \Gamma^R} \sum_{JJ'} \sum_i \Delta_{ii}(J, J') \right) \times \frac{\gamma_1 + \gamma_2}{g_{N-1} \gamma_2 + g_N \gamma_1} (f_L - f_R). \quad (3.9)$$

From this equation, when T approaches zero, we find that the relative peak heights are given by

$$\frac{I_N^+}{I_N^-} = \frac{g_N + \lambda g_{N-1}}{\lambda g_N + g_{N-1}}. \quad (3.10)$$

Eq.(3.10) can be applied to any QD regardless of the nature of its degeneracy. It is a generalization of the case where only spin degeneracy is present[67]. Note that Eq.(3.10) reduces to

$$\frac{I_N^+}{I_N^-} \approx \frac{g_{N-1}}{g_N} \quad \text{if } \Gamma^L \gg \Gamma^R, \quad (3.11)$$

which can be explained in many-body language as follows: when the bias voltage is applied such that current flows from right to left, its magnitude will be proportional to the number of available N -body states so that a new electron can enter the quantum

dot. This is because, the transport is dominated by the slower process, *i.e.* tunneling through the right lead. Now, if the applied bias voltage is reversed, transport will be dominated by the electrons inside the quantum dot that are trying to get out through the right lead. Thus, the current will be proportional to the number of available $(N - 1)$ -body states so that the system can release an electron. We conclude that $I_N^+/I_N^- \approx g_{N-1}/g_N$. For a parabolic two-dimensional QD, the many-body ground states for $N = 1$ to 5 are given by $(L, S_z) = (0; \pm 1/2), (0; 0), (\pm 1; \pm 1/2), (0; 0, \pm 1)$, and $(\pm 1; \pm 1/2)$, which perfectly explains the current ratio obtained from Fig.3.6.

This effect, if observed in a real experiment (the quantum dot must be extremely clean so that the degeneracy of many-body states is not broken), can be used to estimate the relative coupling strength of the leads.

3.4 Summary

To summarize, we have studied addition spectrum and transport properties of two-dimensional parabolic circular quantum dots using exact diagonalization technique and Keldysh Green's functions formalism. Addition spectrum calculated by exact diagonalization agrees qualitatively well with the experimental results, providing useful insight to the many-body states and transitions induced by magnetic field. Exact calculation of the spectral function allowed us to show that, for some values of magnetic field, the ground to ground state transition probabilities are diminished due to correlation effects, it can even be zero when spin blockade occurs. However, in a real experimental situation, a finite bias is applied and the temperature is nonzero, such that transitions through excited states occur. Our calculations including lowest lying excited states show that, in this case, the current is recovered for a rather small bias (≈ 0.2 meV) and temperature (≈ 0.2 K). We have also studied the effect of asymmetric coupling to the leads at zero magnetic field, which leads to a very interesting effect[118]: reversing the bias causes a change in the magnitude of the current which can be predicted using a very simple equation, which depends on (i) many-body degeneracy and (ii) relative coupling strength of right and left leads.

Ring-Shaped Quantum Dots

4.1 Introduction

Although the parabolic circular confinement potential remains a good model for explaining many important many-body properties of QD's, both experimental and theoretical investigations have provided clear indications that the confining potential landscape can play an essential role to the many-body states of the QD[119, 80, 81, 82, 120], especially under a strong magnetic field. Tunneling into a disordered QD, for example, may lead to addition of *pairs* of electrons to the QD[80] because the two electrons can enter spatially distinct regions provided by disorder[81, 25]. Experimental and theoretical analysis have also been reported for QD's with more complicated confining potential landscape, including lateral double QD's[121, 122, 123, 124], vertical double QD's[19, 125], and ring-shaped QD's[85, 86, 87, 88, 84]. First experimental spectroscopic study of quantum rings in the scatter-free quantum limit was very recently reported by Lorke *et al.* in 2000. It is expected that energetic competitions due to strong electron-electron interactions, magnetic fields, and confining potential geometry, will lead to interesting and perhaps complicated many-body correlation in QD devices which can manifest in the tunneling current.

Motivated by the importance of geometry in the confining potential of a QD, in this chapter, we present investigations of the combined effects of interactions, magnetic field, and geometrical factors by exact diagonalization and Keldysh nonequilibrium transport formalism. The geometrical effect is generated by a confining potential distortion that generates two potential minima, and abrupt electron redistribution

occurs as the magnetic field is increased. Due to the spatial localization of electrons in different potential minimum, a new transport blockade is predicted in addition to the familiar Coulomb and spin blockades. We calculate the addition spectra of the dot confining a small number of electrons, and using the exact spectral function we evaluate tunneling current by the Keldysh non-equilibrium Green's function formalism. The geometrically induced blockade drastically diminishes the tunneling current.

In section 4.2 we explain our QD model which consists of a ring-shaped potential with a central confinement potential. In section 4.3, our main results are presented: (i) Due to localization effects provided by the two local potential minima, there is an *abrupt* redistribution of electrons between the two potential minima in the QD as the magnetic field is varied; the electron density in the core potential minimum is suddenly changed at specific field strength. (ii) We have discovered a geometry induced blockade effect due to a spatial separation of electrons in the dot, which results in a suppression of conductance peaks at low temperature that should be testable experimentally. (iii) We have found that the addition spectra of the distorted QD show new behavior as electrons go into different spatial regions. While we did not detect cases of zero addition energy (so that paired tunneling occurs), due to the two potential minima there are situations of reduced addition energy.

4.2 Model and method

We consider cylindrically symmetric QD's with a parabolic confinement potential distorted by a smooth radial barrier (see inset in Fig.4.1(a)). As discussed above the symmetry helps the exact diagonalization procedure. Our QD is confined in the z -direction by infinite walls, and an uniform magnetic field B is applied along this direction. Before discussing the many-body analysis, we first consider the single particle basis set which we use to expand the many-body wave functions. In the effective mass approximation, single particle Hamiltonian of this system is given by

$$\begin{aligned} \hat{H}_0 = & \frac{1}{2m^*} \left(\mathbf{p} - \frac{e}{c} \mathbf{A}(\mathbf{r}) \right)^2 + \frac{1}{2} m^* \omega_0^2 \mathbf{r}^2 \\ & + g^* \mu_B B s_z + V_w(z) + V_p(r) \end{aligned} \quad (4.1)$$

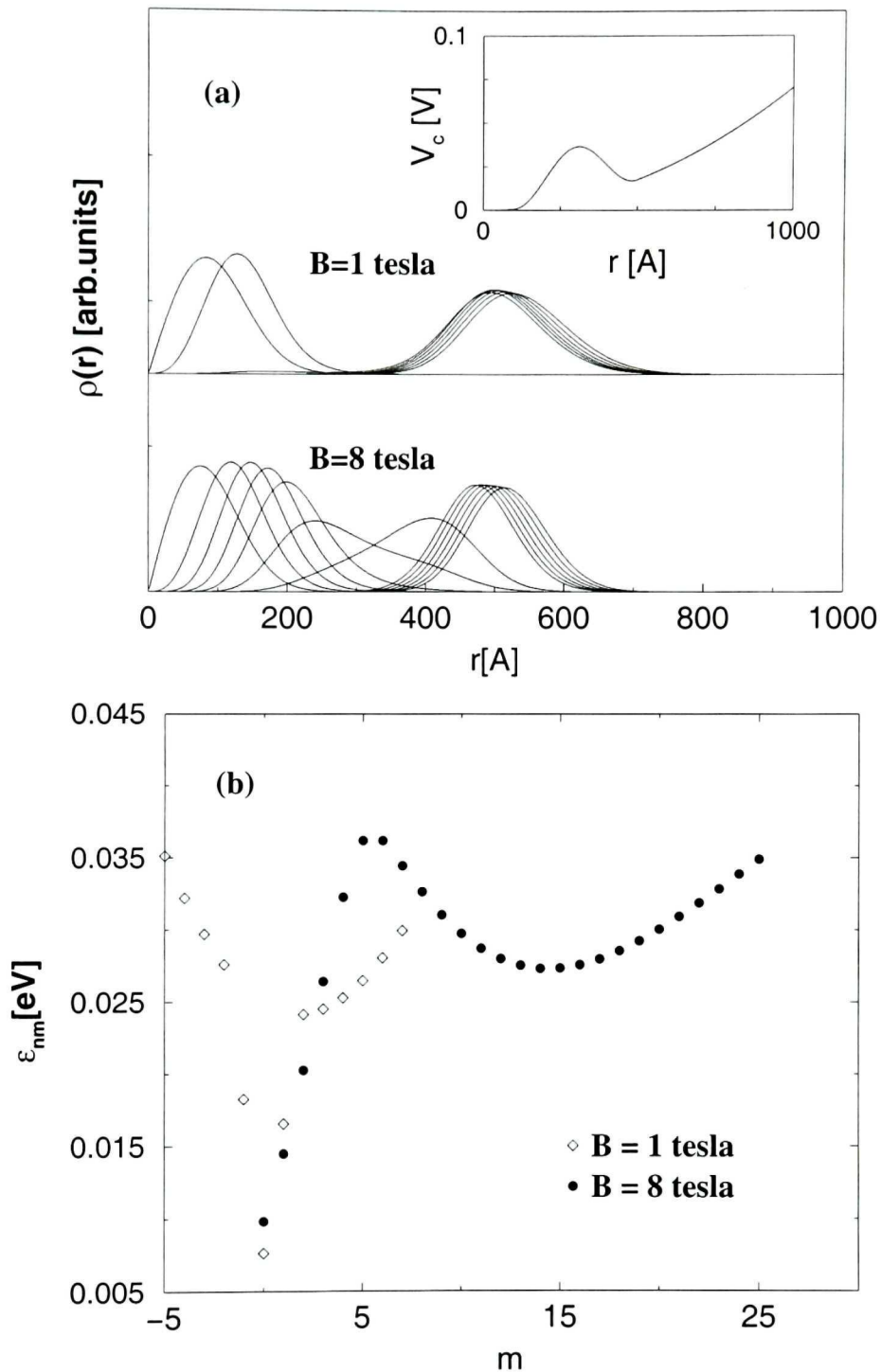


Figure 4.1: Single particle density for a few lowest single particle states. (a) Density as a function of radial coordinate r , at $B = 1$ tesla and $B = 8$ tesla. Inset: the confining potential as a function of radial distance for the quantum dot. The confining potential is distorted from a perfect parabolic shape by a barrier that separates the dot into a core and a peripheral region. (b) Single-particle energy levels as a function of angular momentum m for quantum number $n = 0$, for the QD potential in the inset of (a).

This equation is similar to Eq.(3.1), except the additional distortion term $V_p(r)$. The precise radial form of $V_p(r)$ is not crucial for the general physics we study—so long as the total confining potential possesses two potential minima so that electrons can reside in localized spatial regions. In the present work, we choose

$$V_p(r) = V_o \left(1 - \cos \left(2\pi \frac{r - r_o + \frac{d}{2}}{d} \right) \right), \quad (4.2)$$

for $r_o - \frac{d}{2} < r < r_o + \frac{d}{2}$; and $V_p(r) = 0$ for other values of r . Here V_o , r_o and d are parameters describing perturbation strength, radial position and barrier width, respectively. We have fixed $r_o = 300 \text{ \AA}$, $d = 400 \text{ \AA}$ throughout the analysis. We use standard material constants correspond to GaAs and fixed the parameter $\hbar\omega_0 = 4 \text{ meV}$. We have investigated two different cases for the confining potential: with weak distortion where $V_o = 5 \text{ meV}$, and strong distortion where $V_o = 15 \text{ meV}$. The inset of Fig.4.1(a) shows the confining potential of a strongly distorted QD.

Although it is possible to use Fock-Darwin states to construct Slater determinants, this is not a good choice for exact diagonalization for the distorted QD. In order to improve the convergence of the results, we first calculate single particle eigenstates of the distorted QD system, starting from Fock-Darwin wave functions. Adding the perturbation potential $V_p(r)$, only the radial part of the wave functions is modified, and the new radial wave functions can be obtained using the Fock-Darwin states as a basis set. Since the angular momentum is still conserved, for each angular momentum state m we obtain modified Landau levels by mixing enough original Landau levels. Energy separation between the different new Landau levels has similar characteristics to the original separations. Therefore, for many-body calculations, the Hilbert space can be restricted to a few modified Landau levels. In this work, we use two modified Landau levels below $B = 6$ tesla and one Landau level above this value.

To give a feeling of the single particle states, Fig.4.1(a) plots single electron densities as a function of distance, for a few lowest states at $B = 1$ and 8 tesla, for a strongly distorted dot with $V_o = 15 \text{ meV}$. The radial barrier leads to localization of these single particle wave functions in different potential minima. Therefore, we define “core” states which live inside the central potential minimum, and “peripheral”

states which live inside the outer minimum. As seen from Fig.4.1(a), the number of core states depends on the magnitude of B . Magnetic field has the effect of squeezing the orbitals and, as a consequence, the number of wave functions which can be fitted in the core region increases with B . Moreover, the overlap between the core states and the peripheral states is very small, therefore if we build two N -body Slater determinants having different numbers of core electrons, the correlation between these states would be practically zero. This has an important effect on transport blockade properties as will be seen later. In Fig.4.1(b), we plot the single electron energies as a function of angular momentum m for $n = 0$. The core states can easily be distinguished from peripheral states by their larger energy gap. At $B = 8$ tesla, the energy separation is about 5 meV between the core single particle states, and it can be much smaller between the lower peripheral states. For instance, the gap between the two lowest peripheral states ($m = 13 - 15$) is about 0.02 meV. Since this is smaller than the Zeeman splitting (0.03 meV/tesla for GaAs), in the single electron picture the first three electrons entering the ring would have their spin up. Thus, the Zeeman splitting which is negligible in the core region cannot be ignored in the ring region.

4.3 Results

4.3.1 Weakly distorted dot

In the following we consider the weakly perturbed QD with $V_0 = 5$ meV. Fig.4.2 shows the spectral function $\Delta = \sum_i \Delta_{ii}$, for the ground state transitions of the QD. An effect of the confining potential distortion is to increase the potential curvature of the core region so that energy separation between the single-electron levels there are higher, and the melting processes (paramagnetic-ferromagnetic transition) occur at higher magnetic fields. For the 5-electron QD, in the region between $B = 2 - 4.5$ tesla as well as at $B = 5$ tesla, the spin blockade occurs, *i.e.* the ground state transition from the 4-electron QD to the 5-electron QD involves changing the total spin of the QD by more than 1/2, which has zero probability (see Eq.3.7). Spin blockade extending over wide field range has also been predicted in double QD's[69].

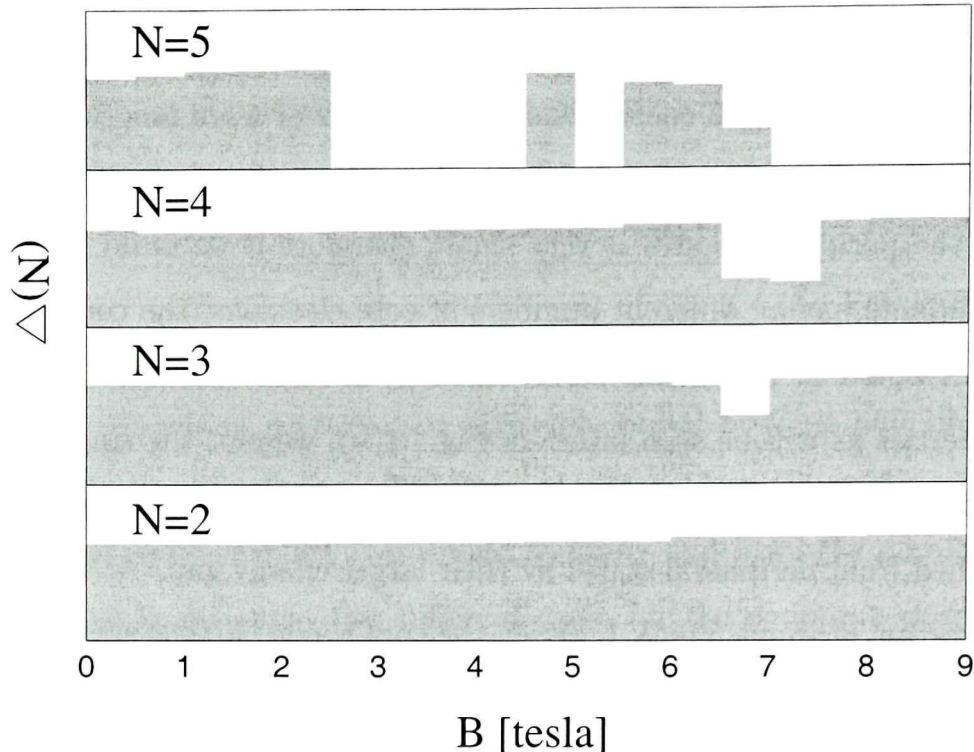


Figure 4.2: Spectral function for the ground state transitions as a function of magnetic field B , for the weakly distorted QD. The empty regions are blocked due to spin blockade or geometrical blockade.

Most interesting, however, is the finding that some many-body states are very strongly affected by the confining potential distortion, an example is the $N = 5$ electronic state (see, also, next subsection where this occurs in $N = 3$ QD). In particular, we found that there is another forbidden transition going from the 4-electron QD to the 5-electron QD in the field range $B \approx 6.5 - 9$ tesla, shown by the absence of Δ in Fig.4.2. This is *not* due to spin blockade because the total spin is changed by only $1/2$. Our investigation indicates that this a new blockade regime that is induced by the fact that electrons can be localized in the two potential minima when $V_0 \neq 0$. At low magnetic fields, the electronic distribution is spread over the two potential minima. When B increases, electrons become more localized in the core and the peripheral regions since the single-electron wave functions are squeezed by the field. This can be seen clearly from the distribution of electron density that can be made quantitative by using Eq(2.27). In Fig.4.3, we show the radial part of $\rho_N(x)$ for $N = 5$. The solid, dashed and dash-dotted lines are for $B = 4, 6$ and 8

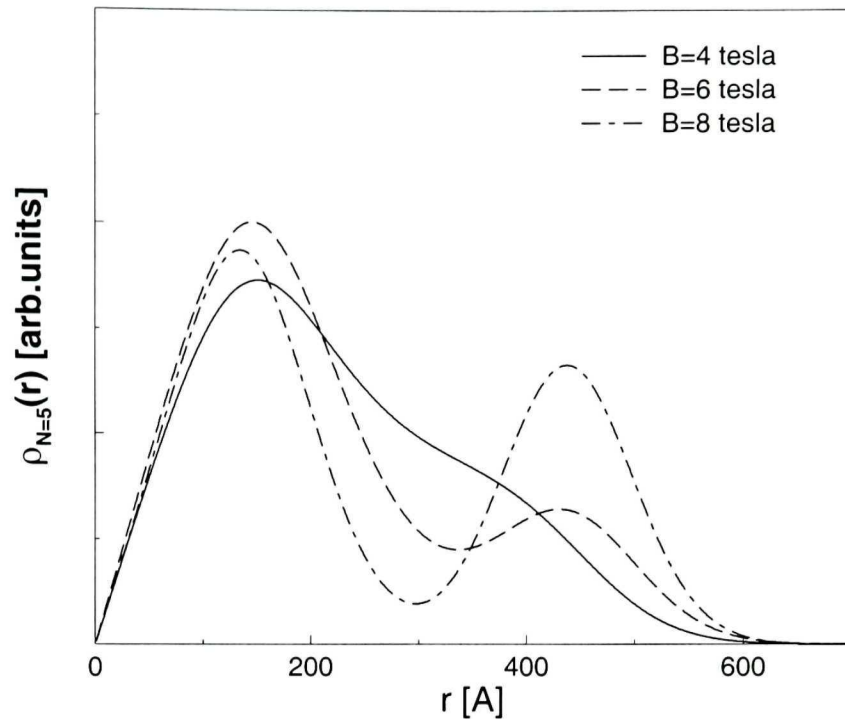


Figure 4.3: Many-body ground state density function for 5 electrons versus radial coordinate r for the weakly distorted dot. Solid line is for $B = 4$ tesla, dashed line for $B = 6$ tesla, and dash-dotted line for $B = 8$ tesla. Localization of electrons in the core and in the peripheral regions is apparent.

tesla respectively. At $B = 8$ tesla, approximately $2/5$ of the total charge resides in the peripheral region. On the other hand, the ground state of the 4-electron QD have all the four electrons in the core region at the same field. Therefore, to add one electron to the 4-electron QD, the $4 \rightarrow 5$ transition requires the addition of the new electron plus a redistribution of one core electron to the peripheral region. The transition probability of such a process is proportional to that given by Eq. (3.6) which turns out to be practically zero. To understand why is this, we denote the 5-electron QD wave function as $|c, c, c, p, p\rangle$ indicating that there are three core electrons (c) and two peripheral electrons (p), and the 4-electron QD wave function after one more electron is added as $|c, c, c, c, X\rangle$, which indicates the four original core electrons and the newly added electron in region X where $X = c$ or $X = p$. Therefore the spectral function is $\Delta = \sum_i |\langle c, c, c, p, p | a_i^\dagger | c, c, c, c \rangle|^2 \sim |\langle c, c, c, p, p | c, c, c, c, X \rangle|^2$. This transition probability is extremely small because mixing between Slater states with different localization configuration is extremely small (smaller than 0.1%) due

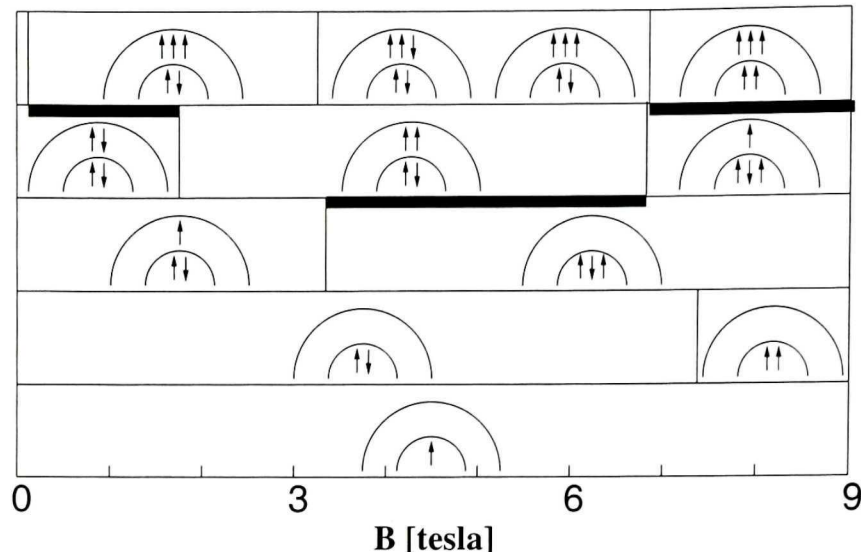


Figure 4.4: Many-body ground states up to 5 electrons as a function of B , for a strongly distorted QD. The QD is schematized by an inner disc representing the core region and an outer ring representing the peripheral potential minimum. Thick lines represent blocked regions during a transport measurement. The arrows indicate spin configuration of the electrons. For simplicity, only those states with equivalent localization-spin configuration representing more than 95% contributions to the exact ground state for $B < 3$ tesla, and more than 99.9% contributions for $B > 3$ tesla, are shown. For this QD, the transition from $N = 3$ to $N = 4$ between $B \approx 3.2$ tesla to 6.8 tesla, and the transition from $N = 4$ to $N = 5$ between $B \approx 6.8$ tesla to 9 tesla are geometrically blocked.

to the spatial separation of the single particle states that make up the many-body Slater determinants. Such a *geometry induced blockade* is near 100% complete: it would greatly reduce the tunneling current when occurs.

We emphasize that the above qualitative picture holds when the single electron states are well localized in different potential minima, *i.e.* when the magnetic field is sufficiently high or when the confining potential distortion is sufficiently strong. We also believe this geometry induced blockade should be a more general behavior when QD potential is sufficiently disordered so that localization of electrons occur, because this effect is due to the geometrical separation of electrons that drastically reduces the spectral function, and it is not related to the specific cylindrical symmetry of the potential distortion used in our QD model.

4.3.2 Strongly distorted dot

The exact diagonalization of the QD with strong distortion ($V_0 = 15$ meV) produces the many-body ground state configurations schematically shown in Fig.4.4, as a func-

tion of magnetic field B . The results are qualitatively similar to the weakly distorted dot. In order to make the interpretation easier, only those states which have different spin and spatial configuration are shown. Configurations in Fig.4.4 represent the most relevant Slater determinants which contribute to the ground state in the corresponding ranges of field. The QD is symbolized with two semi-circles, the inner circle represents the core region (central potential minimum), and the outer circle represents the peripheral region (outer potential minimum). The arrows indicate spin states of the electrons occupying the regions. Thus, for example, at 4.5 tesla and for a 4-electron QD, the ground state has two electrons in the core region forming a spin singlet with the other two electrons in the peripheral region in a spin triplet. The thick black lines represents forbidden transitions between a $(N - 1)$ -electron QD and a N -electron QD. For instance, between $B \approx 3.2$ tesla to 6.8 tesla, no electron can be added to a 3-electron QD to obtain a 4-electron QD due to the geometrical blockade discussed in the last subsection: transport is therefore blockaded in this field range.

Strictly speaking, eigenstates of a many-body Hamiltonian are a superposition of all possible Slater determinants with the same M and S_z . Therefore one may expect a possible mixing between states with different localization configuration but the same total angular momentum, leading to a much more complicated graph than Fig.4.4. However, especially when there is a strong magnetic field such that the system is dominated by the first Landau level, the mixing between states with different localization configuration is practically negligible due to weak tunneling between the two potential minima. Moreover, when B increases, the angular momentum of the lowest peripheral states decreases, which makes the energy difference between the Slater states with the same M but different localization configuration higher, reducing the mixing even more. For instance, for $B = 3 - 6$ tesla, the contribution to the 4-electron ground state by Slater states having only one peripheral electron (instead of the two as shown in Fig.4.4), is found to be less than 0.1%. These contributions, while non-zero, are not important, so that we do not draw them in Fig.4.4. We note that this picture holds especially at low number of electrons, otherwise the wave

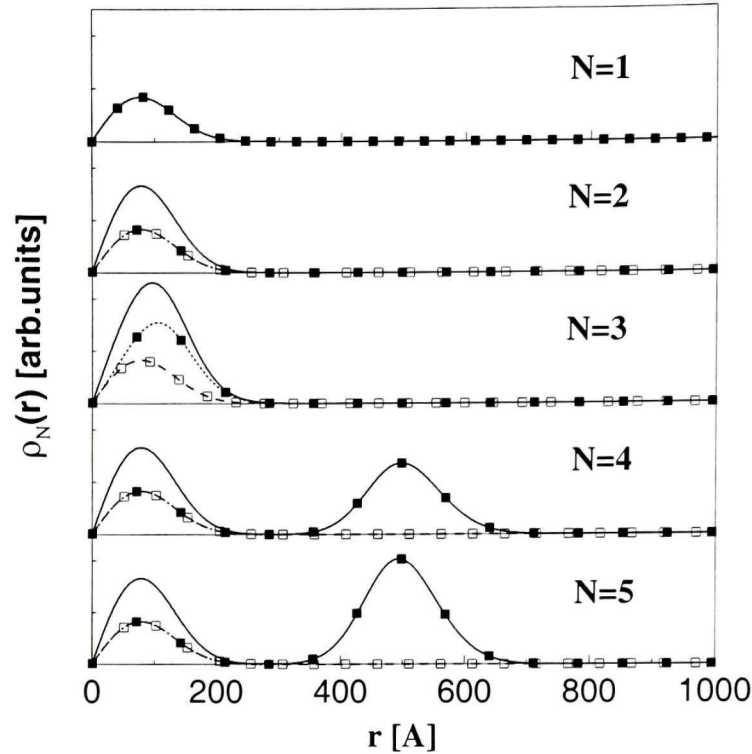


Figure 4.5: Many-body ground state density function versus position r up to $N = 5$ at $B = 6$ tesla, for the strongly distorted QD. Solid lines are for the total radial charge distribution; dotted lines with solid squares are for spin-up contribution; dashed lines with empty squares are for spin-down contribution.

functions would become delocalized in the dot. The distribution of electron density, schematically shown in Fig.4.4, can be made quantitative by using Eq.(2.27). The solid lines in Fig.4.5 show the radial part of $\rho_N(x)$ up to five electrons at $B = 6$ tesla. The dotted line with solid squares indicate the spin-up contribution to $\rho_N(r)$, while the dashed line with empty squares are for spin-down configurations. Comparing with Fig.4.3, it is clear that the spatial separation of electrons into the core and peripheral regions is much more apparent for this QD with stronger confining potential perturbation.

The most interesting result is how the spatial separation of electrons correlate with the orbital and spin degrees of freedom. Returning to Fig.4.4, for 2-electron wave functions, our calculations show that the only effect of potential distortion is to push the singlet-to-triplet transition to near 7 tesla from ~ 3 tesla when there is no distortion. A large field is needed for our distorted dot because of the larger energy gap between core states which makes the change of an electron from $m = 0$ to $m = 1$

more difficult. For three electrons the effect is more striking: the peripheral and core regions are in competition for the third electron. At low field, the third electron (keeping in mind that we are using single electron language in these discussions) has two possibilities: it may reside in the core region and occupy the next single particle state, or it may reside in the peripheral region. For our QD, it turns out that the ground state is for the third electron to reside in the peripheral region at low B , because of the large energy gap between the core states at low B so that the third electron rather enters the peripheral region even though that region is a higher potential minimum. Another reason is that a reduction of total Coulomb interaction occurs when the third electron goes into the outer region of the QD. As B increases, the energy gap between the core states decreases, and as a result, an abrupt *redistribution* of an electron into the core region occurs at $B \sim 3.8$ tesla. Thus, in this transition regime the electron density n_e changes abruptly from $\sim 2.5 \times 10^{10} \text{ cm}^{-2}$ to $2.5 \times 10^{11} \text{ cm}^{-2}$. These estimates were obtained using the effective dot area. Using the conventional definition $r_s = a_B^{-1}(\pi n_e)^{-1/2}$ (where a_B is Bohr radius which is about $1 \times 10^{-6} \text{ cm}$ for GaAs), we obtain $r_s \sim 3.6$ below 3.7 tesla and $r_s \sim 1.1$ above this field. Abrupt electron redistribution has previously been seen experimentally[10] in another context, namely when a MDD in the QD breaks up into LDD as B is increased. In other words, during the MDD to LDD transition driven by an increase of B , the density reduces. However, exactly the opposite is observed in our distorted dot. This is because our MDD states are at higher values of B , *e.g.* the last configurations of the $N = 2$ and $N = 5$ panels of Fig.4.4, and here the inter-minima electron redistribution occurs at a lower B and it is totally due to an energetic competition between the two potential minima. For the 4-electron QD at $B < 2$ tesla, there are two electrons in the core and two in the peripheral region with total spin minimized. At ~ 2 tesla, the outer electrons become spin polarized. This singlet-triplet transition involving peripheral electrons is easier to realize than that in the core region because of the closer gap between the electronic states in the peripheral region. Then, at $B \sim 7$ tesla, a transition between the two local potential minima occurs by which an outer

electron redistributes into the core region. For the 5-electron QD, the localization configuration does not change in the magnetic field range studied here, *e.g.* there are two electrons in the core and three in the peripheral regions all the way to $B = 9$ tesla. However, when B is between 3 – 7 tesla, we observe a rapid oscillation of the total spin in the peripheral region, where the single electron level spacing can be as low as 0.05 meV which is in the same order of magnitude as the Zeeman splitting as discussed earlier. Therefore, as the magnetic field varies, the fifth electron changes its spin state essentially due to the level crossing, although in some case, we also observe that one electron in the peripheral region can jump into a larger orbital reducing the Coulomb interaction instead of staying in the lowest peripheral state. Finally, near 7 tesla the system becomes fully polarized.

These results, obtained from our specific QD, suggest a general picture on electron distribution in QD's with two (or more) potential minima, namely that it is critically affected by the relative single particle level spacing in each of the potential wells. Together with the Coulomb interaction, these factors determine to a large extent where the electrons will reside. The magnetic field B , on the other hand, reduces the level spacing and squeezes the orbital, causing a redistribution of the charges.

In Fig.4.6 we plot the addition spectra as function of B . The first 3 electrons enter the QD with an addition energy between 8 – 10 meV. However, the next electrons have addition energies which are decreased considerably. There are several reasons for this behavior. First, interaction between electrons sitting in different potential minima is much weaker, only about 2 meV (with essentially no exchange energy due to weak wave function overlap). The direct Coulomb energy between peripheral states is low, ~ 3 meV, because they lie on large orbitals; whereas the attractive exchange energy between the nearest peripheral states can be as high as 1.5 meV due to their substantial overlap. In addition, as mentioned earlier, the energy difference between the lowest peripheral states are smaller than 0.1 meV. As a result, the overall addition energy for 4 and 5 electrons is about 1 – 3 meV. These results suggest that, in a tunneling measurement, the closest electron addition energy should occur after

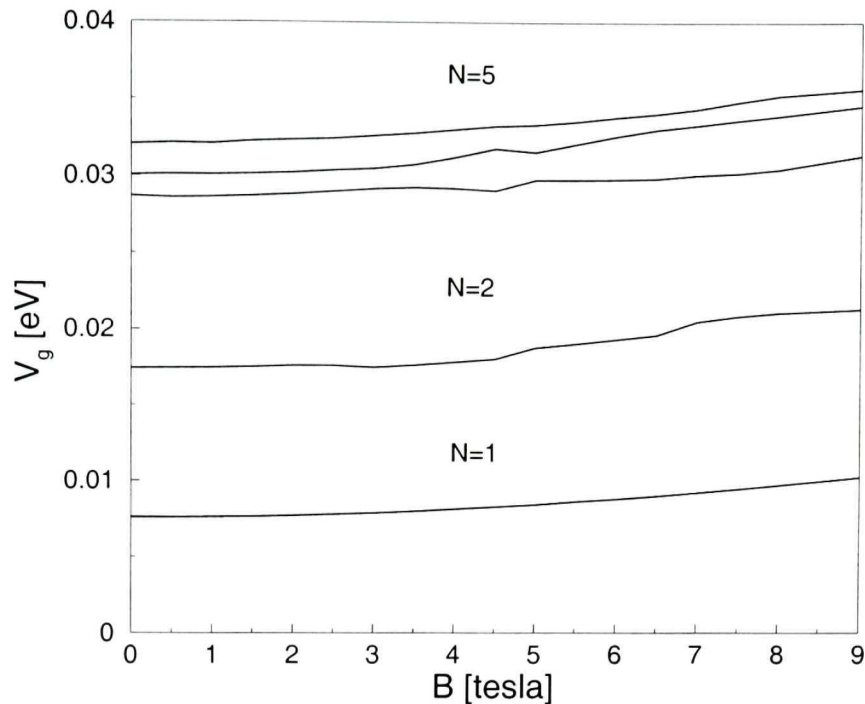


Figure 4.6: The addition spectra (chemical potential) of a strongly distorted QD as a function of B . The charging energy is substantially reduced after $N = 3$ due to spatial localization of electrons.

the first time when an electron enters the outer potential minimum, *i.e.* the third electron for $B < 4$ tesla, the fourth electron for $B > 4$ tesla, etc.

In Fig.4.7, we compare transport properties of 3,4 and 5-electron QD's at temperatures $T = 0.2$ K and 1 K as calculated by Eq.(3.5). Bias voltage is fixed to 0.05 meV such that the system is essentially in the linear regime at low temperatures, and we take $\lambda = 0.01$. At $T = 0.2$ K, the current is dominated by transitions through ground states as given in the Fig.4.4. It is clear that the current is strongly suppressed especially for $N = 3$ to $N = 4$ transition in the geometric blockade region. In the spin blockade region between $B = 0.5 - 2.5$ tesla, most of the current is recovered due to the transition from the 4 electron first excited state as we verified from the numerical analysis. In the $N = 5$ geometric blockade region, the gap of excitation energies is about 0.1 meV which is higher than bias voltage. However, this is small enough to make transitions through excited states which are not blockaded ($|c, c, p, p \rangle$ to $|c, c, p, p, p \rangle$ and $|c, c, c, p \rangle$ to $|c, c, c, p, p \rangle$) possible with increasing temperature. Thus, we see that at $T = 1$ K the current peaks increase in the $N = 5$ geometric

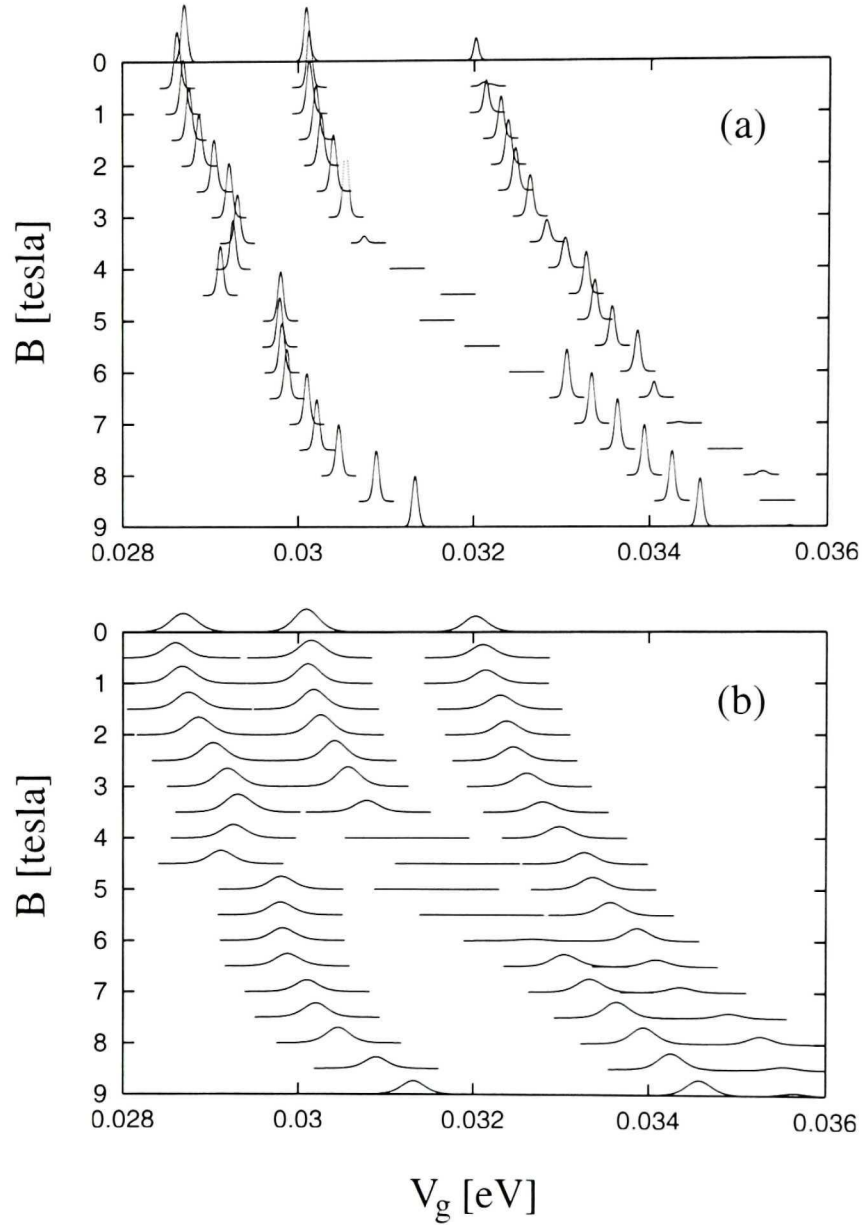


Figure 4.7: 3D plot of tunnelling current (arb.units) as a function of B and V_g for a strongly distorted QD. (a) For $T = 0.2$ K and (b) for $T = 1$ K. Bias voltage and the asymmetry parameter λ are fixed at 0.05 meV and 0.01 respectively. The blocked regions are clearly seen, and raising temperature may increase tunnelling current in the blocked regime.

blockade region. However, for $N = 4$ blockade region, current is still strongly suppressed at $T = 1\text{K}$ due to a larger energy spacing of the excited states. For instance, gap between the lowest $|c, c, p\rangle$ excited state and the $|c, p, p\rangle$ ground state reaches 0.5 meV at 5.5 tesla . This gives an approximative maximum bias voltage for which geometric blockade effect can be observed in this specific dot. We also note that at the edges of the blockaded region, excitation gap of different localization states become degenerate. As a consequence, the transition channels from $|c, c, p\rangle$ to $|c, c, p, p\rangle$, and from $|c, c, c\rangle$ to $|c, c, c, p\rangle$ become available at $B \sim 3.5\text{ tesla}$ and $B \sim 6.5\text{ tesla}$ respectively.

4.4 Summary

To summarize, using exact diagonalization we have analyzed 2D quantum dots whose confining potential is distorted so that there are two potential minima present. The ring-shaped potential landscape provides a competition of various contributions to the total energy by spatially separating electrons. Such effects have interesting implications for tunneling current in the Coulomb blockade regime, at least for cases involving small number of strongly interacting electrons as we have studied. By localizing in different potential minima, the total ground state energy is minimized. However, due to the energetics competition, adding an electron to the QD may involve a charge redistribution between the two potential minima. We found that this redistribution occurs abruptly as the magnetic field is increased. A most interesting outcome of the redistribution is a new blockade phenomenon which is caused by a drastic reduction of the spectral weight for the transition from a $(N - 1)$ -electron QD to a N -electron QD due to the spatial localization of the electrons. The geometric blockade leads to a drastic reduction of the tunneling current which should be measurable experimentally. Finally, the addition energy is substantially reduced when electrons start to redistribute in different spatial regions, this is similar to that obtained before[25].

Clearly, the precise occurrence of the geometric blockade, *i.e.* at which number of

electrons N and at what magnetic field value B , is dependent on the strength of the confining potential distortion and spatial separation of the minima, but the physics of energetic competition between strong interactions, magnetic fields, and geometry, is rather general and should be present in QD's with sufficient disorder so that electrons can localize themselves in different spatial regions.

Effect of Impurities in Parabolic Quantum Dots

In the previous chapter, we have studied the effect of spatial localization of electrons in a ring-shaped potential landscape *i.e.* where the circular symmetry is not broken, by exact diagonalization method. Another interesting situation occurs when the potential landscape is distorted by random disorder such that the circular symmetry is broken. This is a very important problem from experimental point of view. Unfortunately, exact diagonalization method is very difficult to apply to these systems, since the total angular momentum is not conserved and matrices to diagonalize are too large even for very small number of electrons. A more suitable choice is QMC method, and it is the purpose of this chapter to report our investigation of disordered (and clean) QD's under an external uniform magnetic field which confine up to 13 electrons, using a diffusion quantum Monte Carlo numerical procedure as discussed in chapter 2. To the best of our knowledge, QMC analysis of QD's containing impurities have been limited to 2 electrons[44, 45], and we are not aware of any previous exact calculations on energetics and spin configurations of disordered QD's up to $N = 13$. Moreover, our DQMC data allow us to probe the physics of clean QD's under external magnetic field with larger number of electrons than studied before. We focus on investigating the competing energetics of electron-electron interaction, magnetic field, and disorder.

In section 5.1, we present our disorder model which consists of gaussian shaped impurities randomly distributed in a circular parabolic confinement potential. The results are discussed in section 5.2; we found that DQMC gives excellent total energy and spin configuration for clean-QD's as compared with exact diagonalization.

Compared with the unrestricted Hartree-Fock (UHF) technique, used as trial states in DQMC procedure, we found that DQMC gives superior advantages in total energy accuracy, especially for low magnetic field regime. DQMC also reduces the problem of artificial density modulation in UHF[56]. We found that disorder has a very significant effect to the total energy of QD. In particular, the energetic transitions (the kinks in energy) between many-body states are made much less clear due to disorder, and the required magnetic field to induce such transitions can be rather different than that of clean-QD. We also found that the Hund's rule for closed shells is robust against even strong disorder, but less so for open shells.

5.1 Model and Method

We consider the standard QD model with cylindrically symmetric parabolic confinement potential. We introduce disorder by randomly positioned impurities with a Gaussian-like impurity potential. We assume a strong confinement in the z-direction so that our QD's are effectively two-dimensional (2D), *i.e.* we neglect effects of the z-dimension on the electron-electron interactions. In the effective mass approximation, the single particle Hamiltonian for such a system is

$$\begin{aligned} \hat{H}_0 = & \frac{1}{2m^*} \left(\mathbf{p} - \frac{e}{c} \mathbf{A}(\mathbf{r}) \right)^2 + \frac{1}{2} m^* \omega_0^2 \mathbf{r}^2 \\ & + g^* \mu_B B s_z + \sum_i V_i^{imp}(\mathbf{r}), \end{aligned} \quad (5.1)$$

where material constants corresponding to GaAs are fixed to $m^* = 0.067m_0$, dielectric constant $\kappa = 12.4$, and fix the parameter $\hbar\omega_0 = 5$ meV which is within typical experimental range [59, 10]. The resulting dimensionless interaction strength of the parabolic confinement given by $r_s = (e^2/\kappa l_0)/\hbar\omega_0$ is fixed to 1.54, where $l_0 = (\hbar/(m^*\omega_0))$. As in previous chapters, Fock-Darwin states are used as the basis set in our calculations of interacting QD's. In Eq.5.1, $\sum_i V_i^{imp}$ represents impurities which are modeled by a Gaussian profile:

$$V_i^{imp} = A_i e^{-\frac{|\mathbf{r}-\mathbf{r}_i|^2}{2\sigma_i^2}}. \quad (5.2)$$

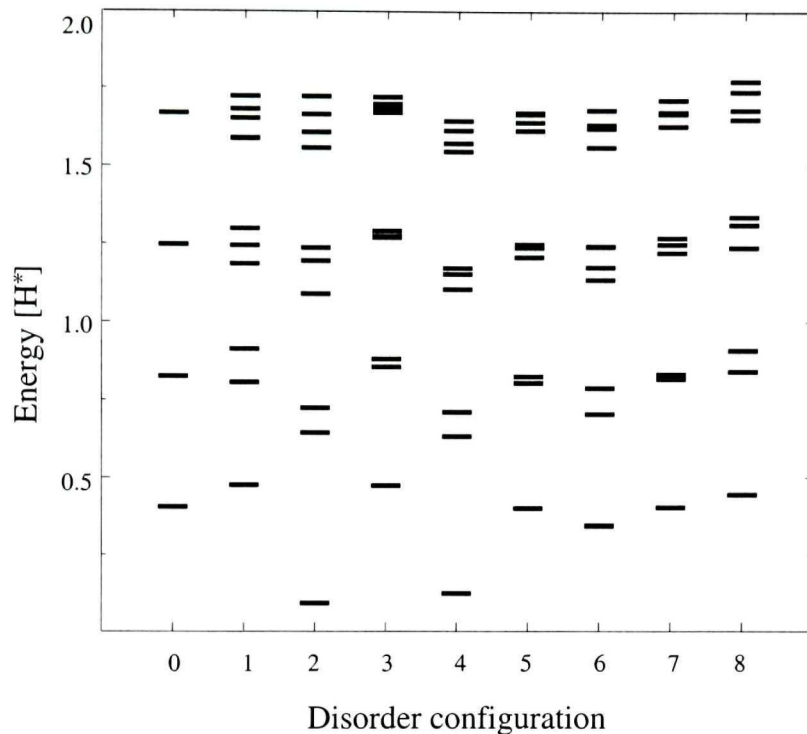


Figure 5.1: Single particle energy for different random disorder configurations used in DQMC calculations. Disorder number 0 corresponds to the clean QD case.

Here the potential strength A_i is uniformly distributed within a range of ± 11.86 meV; and the width σ_i is uniformly distributed in range 3–10 nm. Number of impurities in the physical area occupied by up to 13 electrons is fixed to 6 which gives an estimated impurity density of $0.6 \times 10^{-3} \text{ nm}^{-2}$. In the following we will use effective atomic units determined by taking into account the effective mass and dielectric constant of GaAs. We define effective Bohr radius a_0^* by Bohr radius times $\kappa m_0/m^*$ which gives 9.793 nm and, effective Hartree H^* by Hartree times $m^*/(m_0\kappa^2)$ which gives 11.86 meV. For magnetic field, we use the unit defined by $\tau = (m^*/m_0\kappa)^2(\epsilon_0/2\mu_B)$ which gives 6.862 tesla.

In this work, we have considered eight different disorder configurations at zero magnetic field (B), and one configuration for finite B . To give a feeling of the strength of the disorder, in Fig.5.1 we plot single electron energies for the eight different disorder configurations at $B = 0$. The first configuration corresponds to a clean dot without

any disorder and its four levels represent the s, p, d and f shells which are responsible for the Hund's rule up to 20 electrons. Adding disorder breaks the cylindrical symmetry of the QD and removes the degeneracy of the shells, as seen in Fig.5.1. However, we note that the shell structure is not completely destroyed by our disorder, and the spacing between levels of the same shell varies around $5 \text{ mH}^* - 100 \text{ mH}^*$.

To investigate the disordered QD's with electron-electron interaction as described by the total Hamiltonian $H = \sum H_0 + H_I$ where H_I is the Coulomb interaction between electrons, we apply a diffusion quantum Monte Carlo technique. The accuracy of DQMC depends largely on the quality of trial wave functions. Several different trial functions have been used in the literature, including solutions by local density approximation[33], single- or multiple-configuration states of non-interacting electrons[32], optimized with Jastrow factors. Our DQMC method uses unrestricted Hartree-Fock (UHF) solutions as trial states. Since spatial symmetry is broken by disorder, it is unclear *a priori* how to make assumptions on the form of the trial wave function. We expect UHF solutions to be a good starting point as we have checked (see below) by comparing DQMC solutions using UHF trial states with exact diagonalization in a disorder-free QD: a very good agreement is found. It is worth mentioning that since UHF solutions are single Slater determinants, only the projection S_z of the total spin can be resolved. To resolve the total spin S , one needs to construct multi-determinant trial functions which is not possible in Hartree-Fock approximation that we use.

The presence of impurities in the Hamiltonian H adds a new degree of complexity to DQMC, because UHF solutions become complex numbers even at zero magnetic field. As discussed in chapter 1, since QMC methods can only deal with positive real numbers, a fixed-phase approximation, which is a generalization of the fixed-node approximation, must be used. In the fixed phase approximation, the exact solution of the many-body problem is assumed to have the same phase as the trial wave function. This approximation was introduced in Ref.[104] to deal with 2D electron gas and later applied to clean QD's[32], in the presence of a magnetic field.

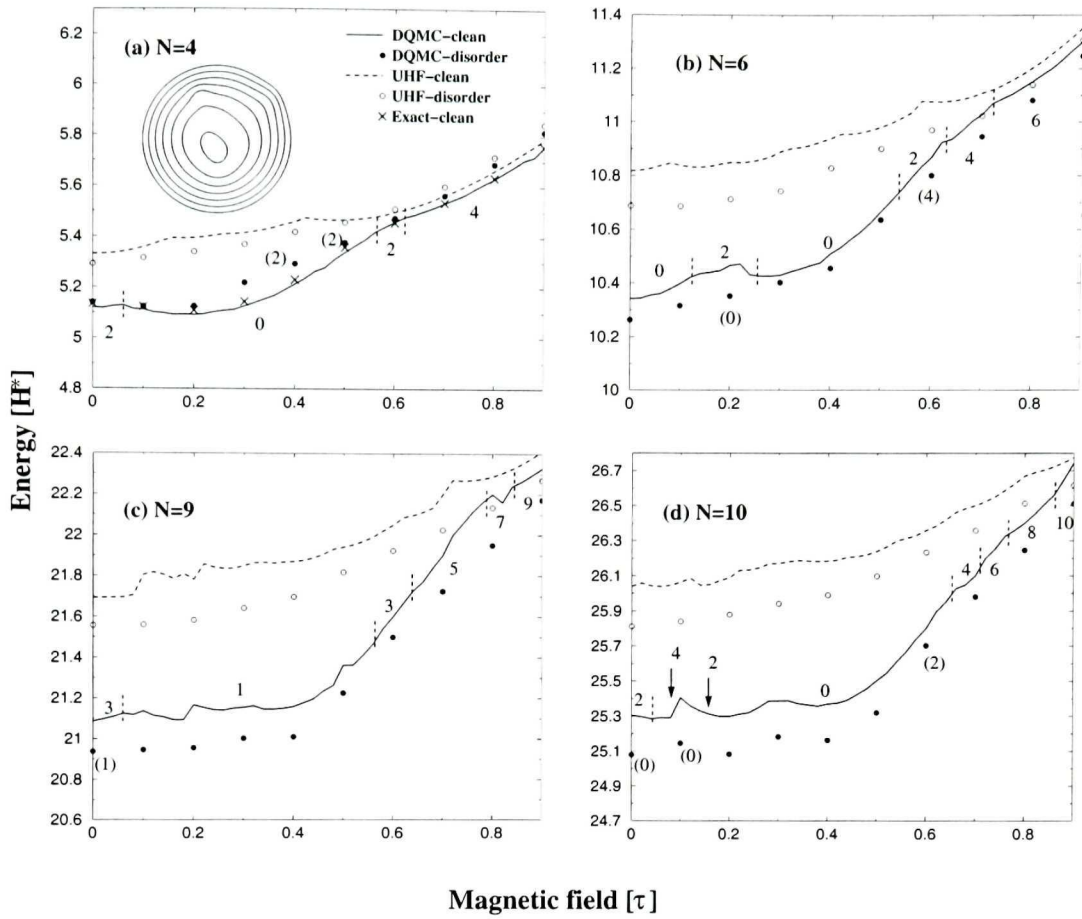


Figure 5.2: Many-body ground state energy as a function of magnetic field for (a) 4 electrons, (b) 6 electrons, (c) 9 electrons, and (d) 10 electrons. DQMC results are shown by solid lines (clean QD) and filled circles (disordered QD); UHF results are shown by dashed lines (clean QD) and open circles (disordered QD). For 4 electrons QD, exact results are also shown. The inset represents the confining potential of the first disordered QD (see Fig.1) and walker positions for $B = 0.9 \tau$ and $N = 4$.

5.2 Results and Discussion

5.2.1 Energy and addition spectra

In this subsection we present results of the total energy and the addition spectra of clean and disordered QD's under an external uniform magnetic field.

In Fig.5.2 we present ground state energies obtained by UHF and DQMC for $N = 4, 6, 9,$ and 10 electrons. Here DQMC results are represented by solid lines for clean QD and filled circles for disordered QD; UHF results are represented by dashed lines for clean QD and open circles for disordered QD. Clean QD results are obtained at every 0.02τ , whereas disordered QD results are obtained at every

0.1 τ . For comparison, we also include results of exactly diagonalizing the many-body Hamiltonian H for $N = 4$ electrons in a disorder-free QD (Fig.5.2(a)). The vertical dashed lines represent spin transitions as obtained by DQMC for clean QD, and total spin in the z-direction ($2 \times S_z$) are also indicated as integers in different magnetic field ranges separated by the vertical dashed lines. The numerical numbers in parenthesis are spins for states of disordered QD, and are indicated only if they differ from the clean QD results. The data for distorted QD in Fig.5.2 were obtained from the first disorder configuration (see Fig.5.1) and its confining potential is shown as the inset of Fig.5.2(a). The shaded area in the confining potential indicates the random walker positions in our DQMC simulation at $B = 0.9 \tau$ and $N = 4$.

First, we consider results for clean-QD's. We have verified that results from exact diagonalization and DQMC agree very well, as shown in Fig.5.2(a) for a clean QD with $N = 4$ electrons. The DQMC results are actually *lower* by $\sim 0.03 H^*$ in the low field region, indicating a slightly better convergence of the DQMC results. The exact diagonalization produced a slightly higher energy in the range of B -field, presumably due to the limited number of Landau levels used in our analysis: In our exact diagonalization calculation, we have used three Landau levels for $B < 5 \tau$, and two Landau levels for $B > 5 \tau$, to obtain numerical convergence of the results. Nevertheless, the agreement between DQMC and exact diagonalization is very satisfactory. In the maximum density droplet (MDD) region, *i.e.* $B > 0.6 \tau$, results from DQMC and exact diagonalization become indistinguishable. The essentially perfect agreement in the MDD region is not surprising since the MDD state has a very small correlation energy and is well approximated by a single Slater determinant. This is also the reason that UHF results are rather close to the DQMC/exact results in the MDD state, see Fig.5.2(a). However, for lower magnetic fields it is well known that the HF method does not give accurate energies and correct spin states[18], as clearly seen in Fig.5.2 for up to ten electrons. Our DQMC results for 6 electrons in a clean QD (solid line of Fig.5.2(b)) agree well with a variational QMC calculation reported in Ref.([38]). Our results give the same spin transition sequences of

$0 \rightarrow 2 \rightarrow 0 \rightarrow 2 \rightarrow 4 \rightarrow 6$ with an increasing magnetic field. For $N = 9$ and $N = 10$ clean-QD's, spin transition sequences are found to be $3 \rightarrow 1 \rightarrow 3 \rightarrow 5 \rightarrow 7 \rightarrow 9$ and $0 \rightarrow 2 \rightarrow 0 \rightarrow 4 \rightarrow 0 \rightarrow 2 \rightarrow 0 \rightarrow 4 \rightarrow 6 \rightarrow 8 \rightarrow 10$ as seen in the Fig.5.2(c) and (d), respectively. The spin states which appear for very small magnetic field windows are shown by arrows in Fig.5.2(d).

Next, we discuss the disorder effects shown in Fig.5.2. The most striking result is the deformation caused by disorder in energy as a function of magnetic field. For instance, the energy difference between clean QD and disordered QD for $N = 6$ is about $0.1 H^*$ at $B = 0.2 \tau$, while it is about $0.02 H^*$ at $B = 0.3 \tau$, as shown in Fig.5.2(b). Due to these differences, the structures in the $E = E(B)$ curve, which are caused by different spin or momentum transitions, are drastically reduced for disordered QD. Such an effect is also observed for other electron numbers, and can make experimental observation of many-body transitions difficult. Analyzing the spin transitions, we find that disorder can strongly affect the total spin. For instance, in a 4-electron QD, $0 \rightarrow 2$ transition occurs at much smaller B (see Fig.5.2(a)), and in the 10-electron QD, $S_z = 2$ state appears at $B = 0.6 \tau$, while no such state exists in the corresponding clean QD. Here we emphasize the qualitative result that disorder can alter the many-body states in some important ways, but the precise changes probably depend on the details of the disorder and its configuration.

Fig.5.3 shows the addition spectrum of clean (solid lines) and disordered (filled circles) QD's. The addition spectrum measures the chemical potential $\mu_N \equiv E_{N+1} - E_N$ as a function of B , which can be experimentally determined by capacitance or tunneling microscopy. Fig.5.3 plots μ_N for up to ten electrons. Note that the even-odd effect[83, 8], *i.e.* the shift in tunneling current in pairs with B , is still visible in the presence of disorder. This pairing effect can be explained in single electron language as follows: When successive spin up and spin down electrons enter the quantum dot, they occupy same spatial orbital, hence they have similar energy versus magnetic field dependency. For clean QD's, we observe the out-of-phase variation of paired spacing which were detected experimentally[83, 8] for higher number of electrons. This effect

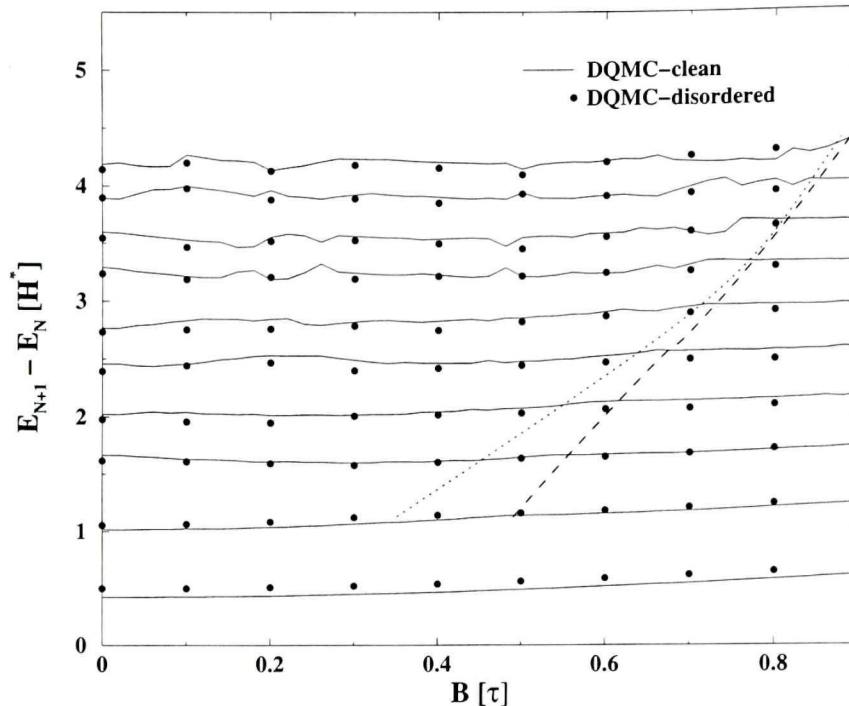


Figure 5.3: Addition spectrum as a function of magnetic field up to 10 electrons, for clean QD (solid lines) and the first disordered QD. Dotted and dashed lines represent left border of the MDD region for disordered and clean QD's respectively.

is due to sharp kinks in energy for odd number of electrons. For instance, the energy of $N = 9$ QD (Fig.5.2(c)) has a sharp transition at $B = 0.5 \tau$, which affects the $\mu_8 = E_9 - E_8$ and $\mu_9 = E_{10} - E_9$ lines of the addition spectrum in an opposite way. Similar effects are also observed for $N = 7$ and 8 pair, sometimes accompanied by a spin transition (*e.g.* $B = 0.48 \tau$). More interesting is how the transition to MDD state is affected by disorder. To see this, in Fig.5.3 we have plotted an approximative line representing the left border of the MDD regime, for clean QD (dashed line) and disordered QD (dotted line). The difference in the transition lines is more important for lower number of electrons. Importantly, although the slope of the transition is changed by disorder, the transition line is still rather smoothly defined as N is increased.

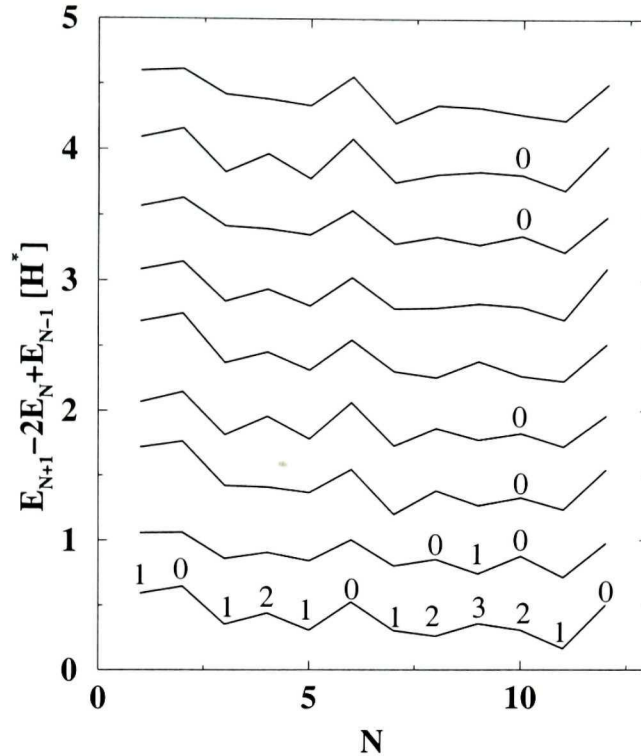


Figure 5.4: Addition energy at $B = 0$ up to 13 electrons for clean QD (the lowest line) and 8 different disorder configuration following the order represented in Fig.1 (2nd line and up). The numbers represent $2 \times S_z$, and they are shown for disordered QD's only if they differ from the clean QD results. Vertical scale is shifted by a constant amount in order to make the interpretation easier.

5.2.2 Hund's rule at zero magnetic field

In atomic physics, Hund's rule determines whether a spin-down or a spin-up electron is added in order to fill the shells sequentially. For closed shells, *i.e.* at atomic numbers (magic numbers) 2, 10, 18, ..., total spin must be zero. For any other atomic numbers, total spin in the open shell must be maximized. Due to the symmetry of the two-dimensional harmonic potential, the magic numbers for the QD system we are studying are 2, 6, 12, ... Experimentally, magic numbers as well as the half-shell electron numbers (4, 9, ...) can be observed since they are responsible for the maxima in addition energies in QD's[8, 126]. This has also been found by exact calculations up to six electrons[20]. The stability of Hund's rule against elliptical deformation[60], random disorder[63] and non-parabolicity of the confinement potential[126] were tested by density functional theories.

In Fig.5.4, we show addition energy up to 13 electrons at zero magnetic field, calculated for a clean QD (the lowest line) and 8 different disorder configurations following the order presented in Fig.5.1 (2nd line and up). It is clear that closed shell structures are not affected by disorder at least for the disorder strengths we have used, giving a higher peak at magic numbers $N = 2, 6$ and 12 corresponding to closed shells. This holds even for the case of large disorder where the ratio between perturbation energy due to disorder and the shell gap is about $1/3$ (see Fig.5.1). On the other hand, although the half-shell peak at $N = 4$ is not affected by disorder, the half-shell peak at $N = 9$ is found to be less robust against disorder. Our calculations show that for the eight disordered QD's we investigated, the 9–th peak is an energy minimum in four of them; in addition, statistical noise in the DQMC calculation prevented us from reaching conclusive results for another three QD's. Finally, we note that a very clear dip at $N = 11$ is observed in all our results.

In Fig.5.4, the numbers on the lowest spectrum represent $2 \times S_z$ for different N . For disordered QD's, S_z is plotted only if it differs from the clean QD case. According to Hund's rule, the total spin must be maximized in the outer shell. Moreover, it is believed that, in disordered QD's, high-spin states are suppressed due to a lifting of the degeneracy [63]. As mentioned before, in our calculations only z-component of the total spin can be resolved, and so in the following we limit our discussions to S_z . Without disorder, our DQMC results are in perfect agreement with Hund's rule. When disorder is added, we found that Hund's rule is especially stable for closed shells as well as for the second open shell ($N = 3, 4, 5$). For the third open shell ($N = 7 - 11$), Fig.5.4 shows that there are some deviations in S_z from that of the clean QD, especially for $N = 10$ where $S_z = 0$ was found in five out of the eight disordered QD's, different from the $S_z = 2$ for the clean QD. A higher probability of $S = 0$ state for $N = 10$ was also found in density functional calculations of Ref.([63]). These results also show that maximal spin alignment does not guarantee a peak at half-shell filling in agreement with the results of Ref.([126]) as seen, for instance, in the disorder configuration number two. Other deviations from the clean QD case

are observed for the third shell of disordered QD number one; spin is minimized for $N = 7, 8,$ and 9 QD's. Finally, in the UHF results (not shown), we did not find any evidence of Hund's rule nor the appearance of high peaks at magic numbers in the addition spectra, even for the disorder-free QD. This is understandable since UHF is not expected to describe effects due to strongly correlated electrons in the QD.

5.2.3 Many-body densities

In this section, we investigate and compare two-dimensional many-body electron densities obtained by UHF and DQMC methods. In QMC methods, expectation values of quantities that do not commute with the Hamiltonian can be calculated using a combination of mixed and variational estimators which, for the density operator, is given by (see Eq.2.63)

$$\rho_{QMC} \approx 2 \times \rho_w - \rho_T + O[(\Phi - \Psi_T)^2], \quad (5.3)$$

where ρ_w is given by the walkers density (mixed estimator), and ρ_T is the density of the trial wave function (variational estimator), which is an UHF determinant in our case. The error obtained by using such estimators depend on the trial wave function. It is well known that unrestricted version of HF can give artificial charge densities arising from symmetry-violating mean field, and it was shown[56] that an azimuthal modulation of charge density can occur due to a superposition of opposite angular momenta. Similar effects are also observed in density-functional theories. It is therefore interesting to see how DQMC reacts to UHF trial functions when such modulations occur.

In Fig.5.5, we superimpose $\rho_{QMC}(\mathbf{r}, \uparrow)$ and $\rho_T(\mathbf{r}, \uparrow)$ calculated for $N = 13$ in such a way that only the highest values are plotted. In the absence of disorder (Fig.5.5(a)), it is clear that UHF method gives azimuthal modulations (solid lines) which are artifacts due to UHF. On the other hand, DQMC smoothes out these modulations (dashed lines) by decreasing the maxima and increasing low density regions by approximately 5-10%. The reduced *radial* modulation in QMC results with respect to HF results were previously observed[33]. Our results further verify that QMC tends to recover

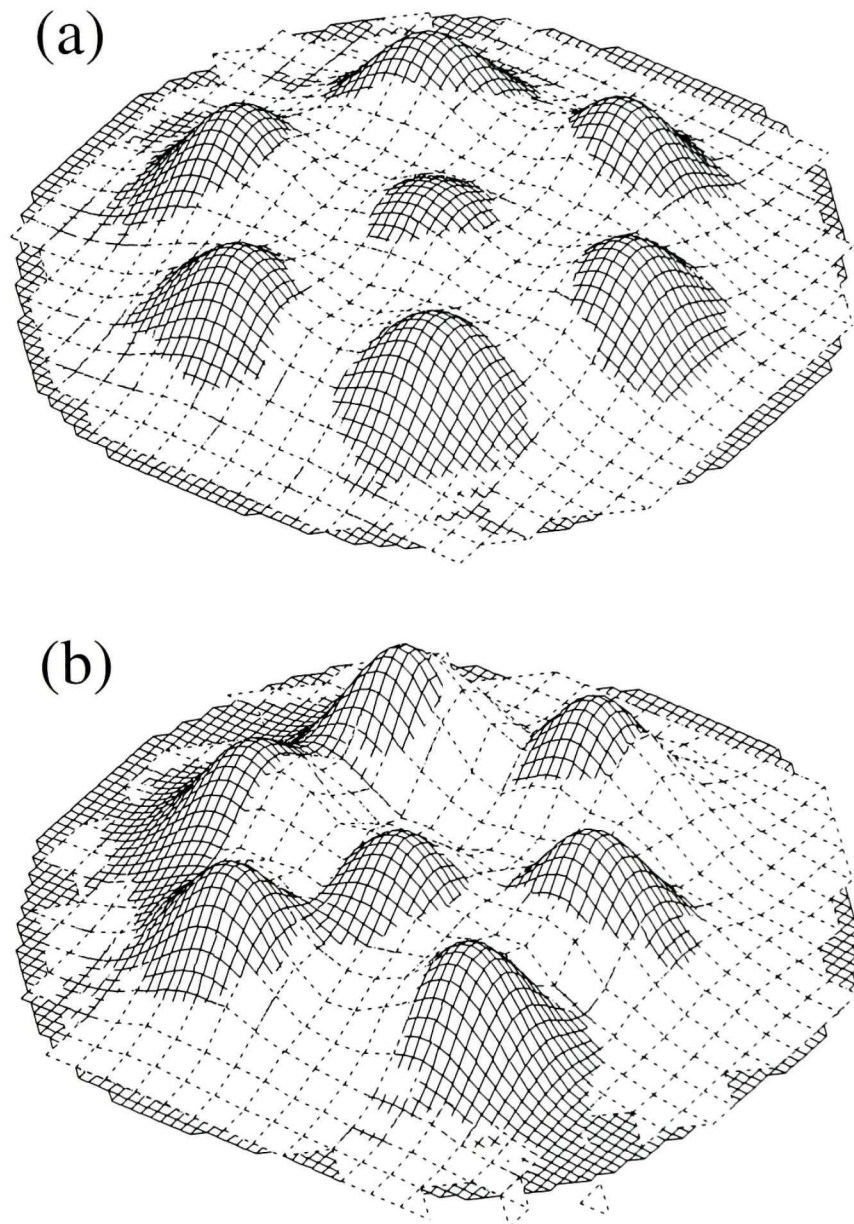


Figure 5.5: Superimposed many-body densities for spin up electrons, obtained by DQMC (dashed lines) and UHF (solid lines), for (a) clean QD, and (b) disordered QD. Only highest values are plotted in order to enhance the difference between DQMC and UHF results.

the correct symmetry properties by also reducing the *azimuthal* modulation. We note that circular symmetry is not completely recovered even with DQMC. There are two reasons: (i) density calculated by Eq.(5.3) is only a second order approximation to the true density; and (ii) DQMC wave functions are assumed to have the same phase as the UHF solutions. Similar density properties are also observed in disordered QD's, as shown in Fig.5.5(b). For disordered QD, there is no circular symmetry so that some azimuthal modulations are expected. However, the DQMC results are still smoother than those of UHF; and the azimuthal modulations in UHF results are distorted by disorder (compare Fig.5.5(a) and 5.5(b)).

Another interesting result obtained by symmetry-violating models such as HF and density-functional approximations is *spin-density-wave* states[57, 51], *i.e.* space-dependent spin polarization with zero total spin. It was argued in Ref.[60] that these states are artifacts of the fact that only S_z is conserved. While we did not observe any spin-density-waves in our clean QD, disorder was found to enhance the UHF ground state spin-density-waves at non-zero magnetic field. In Fig.5.6(a), we plot UHF solutions to 8-electron QD at $B = 0.3 \tau$, where solid lines are for spin up electrons and dashed lines for spin down electrons, showing a spin texture which is created by a dephased azimuthal charge density modulation of spin-up and spin-down electrons (a density maximum for spin up electrons corresponds to a density minimum of spin down electrons). However, once again, in DQMC calculations the modulations are smoothed as seen in Fig.5.6(b) for spin-up electrons and similar result is obtained for spin-down electrons (not shown). Therefore, we conclude that DQMC reduces the artificial spin-density-waves although without destroying them completely for the same reasons given above.

5.3 Summary

We have investigated the competing energetics of electron-electron interaction, magnetic field, and disorder, in quantum dots with up to thirteen electrons, using a DQMC technique. DQMC is shown to give excellent total energy and spin configu-

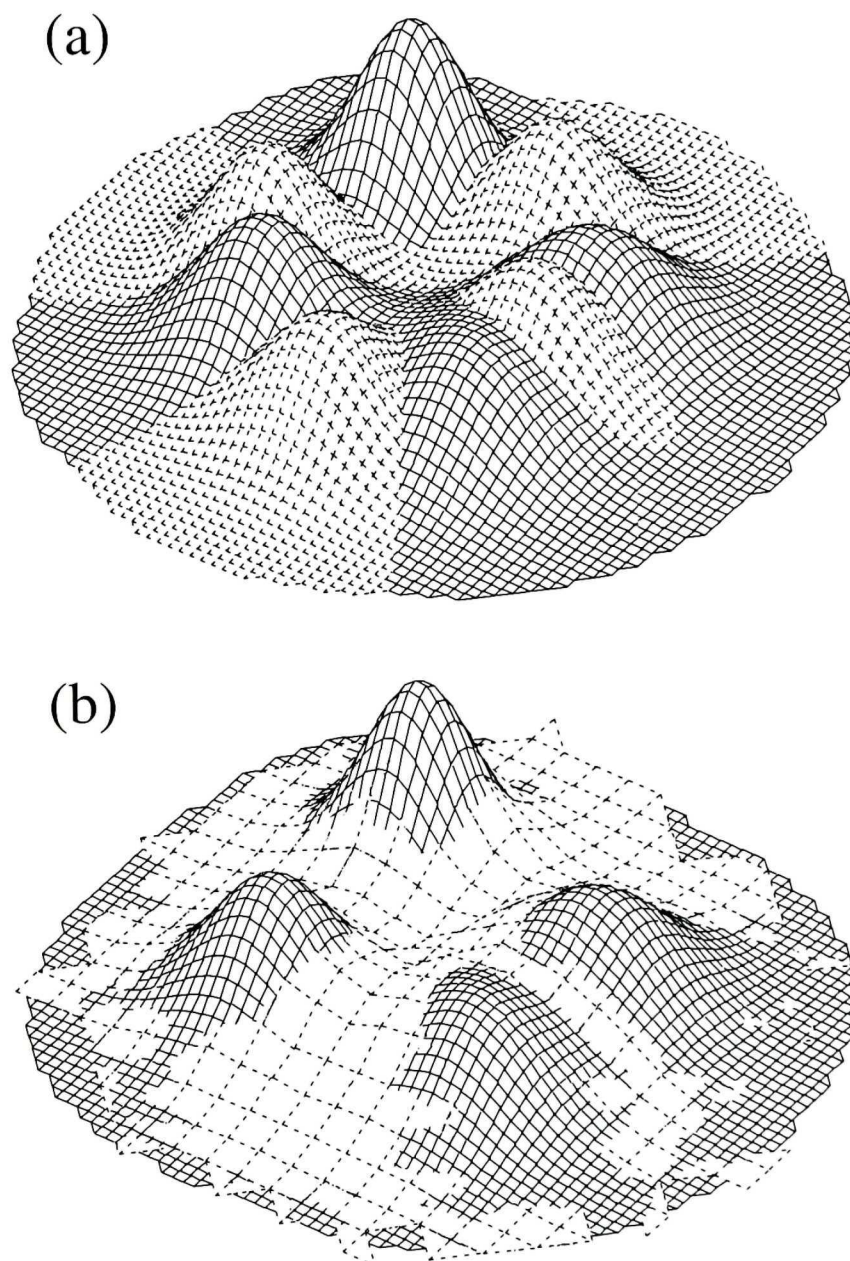


Figure 5.6: Superimposed many-body densities (a) obtained by UHF for spin up (solid lines) and spin down (dashed lines) electrons, (b) obtained by UHF (solid lines) and DQMC (dashed lines) for spin up electrons.

ration for clean-QD's as compared with exact diagonalization, and is very powerful for investigating disordered QD's which do not possess any spatial symmetry. The lack of spatial symmetry makes an exact calculation very difficult if not impossible for $N > 7$, even for modern computers. Compared with the UHF technique, DQMC gives superior advantages in total energy accuracy, especially for low magnetic field before the transition to maximum density droplet states. DQMC also reduces the problem of artificial density modulation in UHF which is a symmetry breaking mean field theory. Disorder is found to have very significant effects to the total energy of QD. In particular, the energetic transition (the kinks in energy) between many-body states is made much less clear due to disorder, and the required magnetic field to induce such transitions may be rather different than that of clean-QD, this may have important implications to interpreting tunneling spectroscopy data. We found that Hund's rule for closed shell is robust against even strong disorder, but less so for open shells. For the lower shells, the spin states are largely unaffected by disorder, but for higher shells (larger number of electrons N) this may change due to disorder.

Kondo Effect in a Quantum Dot Molecule

6.1 Introduction

A peculiar behavior of conductance in some metals discovered over 60 years ago is the enhanced resistivity as the temperature is lowered below a certain value. This phenomenon which is due to the presence of magnetic impurities in the metal was first explained by Kondo[127] as spin-flip scattering between the delocalized conduction electrons and the localized impurity spin. Later, theoreticians [128, 129, 73, 76] predicted that similar effect should manifest itself in the transport through QD's. Consider a QD whose energetic diagram is established by various gate and bias voltages as shown in Fig.6.1. Here all the levels below (μ_L, μ_R) are filled except the highest level ϵ_0 which is occupied by only one electron. We assume it to have spin-up. When our QD is in the state shown in Fig.6.1, the electron at ϵ_0 cannot tunnel out of the QD because $\epsilon_0 < \mu_L, \mu_R$. An electron outside the QD cannot enter the QD unless the Coulomb energy U is overcome. Therefore, the first order tunneling events are Coulomb blocked and there is no current flow. This is the familiar Coulomb blockade phenomenon discussed before in chapter 1. However, due to uncertainty principle, in a time $\tau \sim \frac{\hbar}{\mu - \epsilon_0}$ (assume $\mu_L \approx \mu_R = \mu$), the electron at ϵ_0 can tunnel out of the QD, followed by another electron outside QD having spin-down tunneling into the QD. This is a virtual co-tunneling process and the quantum superposition of infinitely many of these co-tunneling events gives rise to a real contribution to transport so that the current at μ is enhanced. At the same time, the average spin in ϵ_0 is zero due to the rapid spin flips during co-tunneling, and we say that the local

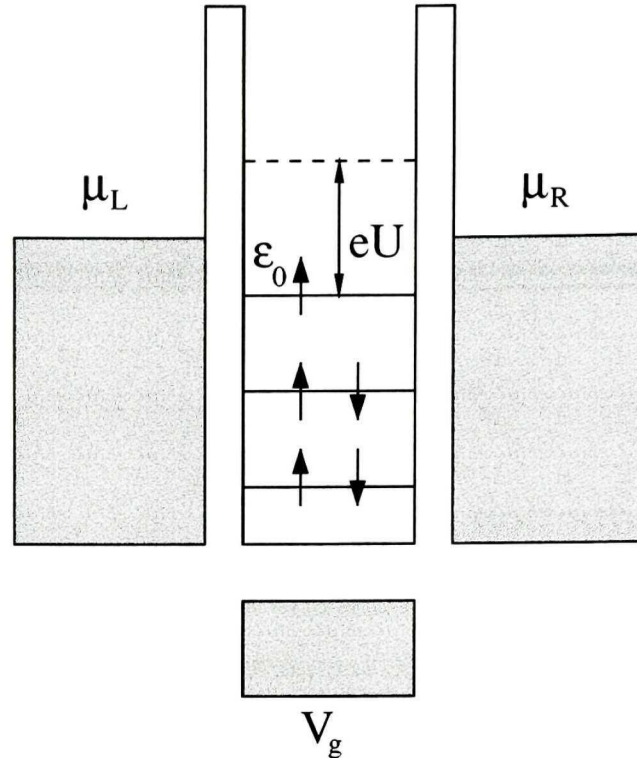


Figure 6.1: Energetic diagram of a QD in Kondo regime.

spin at ϵ_0 is “screened” by the free electrons in the leads. This is the phenomenology of QD Kondo effects, observed experimentally by many groups so far[64, 65, 66].

Another interesting question is whether Kondo effect can occur between a localized spin and quantized states instead of delocalized free electrons. Such system can be experimentally realized by coupling two QD’s (QD molecule) together, and by connecting one of them to external leads. Recent theoretical calculations show that[130, 131, 132], transport through a single quantized state in Kondo resonance with a localized spin can be strongly suppressed. A more realistic situation occurs in QD molecules when several quantized states (transport channels) are present. This question has not yet been addressed, and it is the purpose of this chapter to study transport properties through a multi-channel QD coupled to a strongly interacting QD, in Kondo regime. In section 6.2, we present our model consisting of an Anderson Hamiltonian, and we introduce a *slave-boson* mean field theory which helps us to simplify the many-body problem. In section 6.3, we calculate the Green’s functions of the system that we need to investigate transport properties. The results are pre-

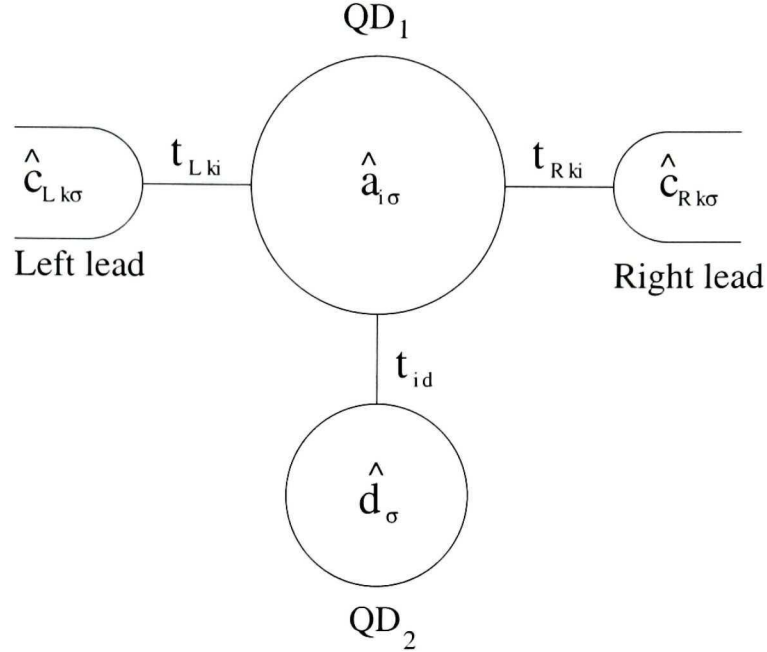


Figure 6.2: Schematic representation of the QD molecule. The bigger dot (QD_1) where the electron-electron interactions are neglected is coupled to the leads. Smaller dot (QD_2) acts as a Kondo impurity and is coupled to QD_1 .

sented in section 6.4. We found that linear conductance has very interesting features as a gate voltage to the conduction channels is applied and the energy of the spin impurity QD is changed. In particular, our results show that the phase of the usual resonant transport oscillations is reversed as the system enters the Kondo regime.

6.2 Model and method

In Fig.6.2, we schematically present our QD molecule. The annihilation operator of the non-interacting states in the bigger dot (QD_1) is represented by $\hat{c}_{i\sigma}$. This QD_1 is coupled to a smaller dot QD_2 in which electron-electron interactions are assumed to be much stronger than in QD_1 . We are interested in investigating transport properties of this system when QD_1 is coupled to the leads. In the Hubbard approximation (*i.e.*, we consider only one channel in the interacting region and include spin degree

of freedom), Hamiltonian of this system can be written as

$$\begin{aligned}
\hat{H} = & \sum_{\sigma} \epsilon_d \hat{d}_{\sigma}^{\dagger} \hat{d}_{\sigma} + \sum_{i\sigma} \epsilon_i \hat{a}_{i\sigma}^{\dagger} \hat{a}_{i\sigma} + \sum_{\alpha k \sigma} \epsilon_{\alpha k} \hat{c}_{\alpha k \sigma}^{\dagger} \hat{c}_{\alpha k \sigma} \\
& + \sum_{\alpha k \sigma i} (t_{\alpha k i} \hat{c}_{\alpha k \sigma}^{\dagger} \hat{a}_{i\sigma} + \text{H.c.}) + \sum_{\sigma i} (t_{i d} \hat{a}_{i\sigma}^{\dagger} \hat{d}_{\sigma} + \text{H.c.}) \\
& + U \hat{d}_{\uparrow}^{\dagger} \hat{d}_{\uparrow} \hat{d}_{\downarrow}^{\dagger} \hat{d}_{\downarrow},
\end{aligned} \tag{6.1}$$

where the first three terms at the right side correspond to single electron states of the QD₁, QD₂, and the leads, respectively. The first term in the second line gives the tunneling matrix elements between the leads and the QD₁, while the second term gives the tunneling matrix elements between the two QD's. The electron-electron interaction in the QD₂ is given in the last line. Note that, there is no summation over the interaction term. This is because, we can at most have one spin up electron plus one spin down electron in a single channel.

The presence of U -term in the above equation makes the Green's function expansion awkward. In order to simplify, we will consider the limit of strong interactions $U \rightarrow \infty$, such that it is less likely to have 2 electrons at the same time in the interacting region. Then, we can simply ignore the U -term. Of course, we now have make sure that the total number of electrons in the QD₂ do not exceed one, by imposing constraints to the Hamiltonian. This can be done through the *slave-boson* approach[130], by enlarging the Fock space which contains the fields of electrons. Let's define a boson field b , and a new fermion field f_{σ} such that

$$\hat{d}_{\sigma} = \hat{b}^{\dagger} \hat{f}_{\sigma}. \tag{6.2}$$

This equation implies that destroying an electron in the QD₂ with spin σ is equivalent to destroy a "pseudo-electron" f with spin σ and create a boson b . Then, the constraint

$$\hat{b}^{\dagger} \hat{b} + \sum_{\sigma} \hat{f}_{\sigma}^{\dagger} \hat{f}_{\sigma} = 1 \tag{6.3}$$

guarantees that we have at most one electron in the interacting dot QD₂. This constraint can be enforced by adding $\lambda(\hat{b}^{\dagger} \hat{b} + \sum_{\sigma} \hat{f}_{\sigma}^{\dagger} \hat{f}_{\sigma} - 1)$ to the Hamiltonian of the

Eq.6.1, where λ is a Lagrange multiplier[130]. Together with Eq.6.2, we obtain

$$\begin{aligned} \hat{H} = & \sum_{\sigma} \tilde{\epsilon}_d \hat{f}_{\sigma}^{\dagger} \hat{f}_{\sigma} + \sum_{i\sigma} \epsilon_i \hat{a}_{i\sigma}^{\dagger} \hat{a}_{i\sigma} + \sum_{\alpha k \sigma} \epsilon_{\alpha k} \hat{c}_{\alpha k \sigma}^{\dagger} \hat{c}_{\alpha k \sigma} + \lambda(\hat{b}^{\dagger} \hat{b} - 1) \\ & + \sum_{\alpha k \sigma i} (t_{\alpha k i} \hat{c}_{\alpha k \sigma}^{\dagger} \hat{a}_{i\sigma} + \text{H.c.}) + \sum_{\sigma i} (t_{id} \hat{a}_{i\sigma}^{\dagger} \hat{b}^{\dagger} \hat{f}_{\sigma} + \text{H.c.}) \end{aligned} \quad (6.4)$$

with,

$$\tilde{\epsilon} = \epsilon + \lambda. \quad (6.5)$$

In the following, we will use a mean-field approximation to describe the boson field, by setting \hat{b} to a constant number b . This means that we are neglecting charge fluctuations around the average $\langle b(t) \rangle$. Nevertheless, this approximation is correct for describing spin fluctuation (Kondo regime). Furthermore, we will suppress the spin index σ since the system is assumed to be spin degenerate.

6.3 Calculation of Green's functions

In order to study transport properties, we need to calculate the full Green's function G_{ii}^r of the QD₁ (see Eq.2.78). To do this, we use Dyson-Keldysh equations 2.71. Generally speaking, when the perturbation Hamiltonian consists of $t_{\alpha\gamma} \hat{a}_{\beta}^{\dagger} \hat{a}_{\gamma}$ tunneling process [75], interaction coupling elements $\Sigma_{\beta\gamma}$ have a very simple expression:

$$\begin{aligned} \Sigma_{\alpha\gamma}^r &= t_{\alpha\gamma} \\ \Sigma_{\alpha\gamma}^< &= 0, \end{aligned} \quad (6.6)$$

which can be shown in terms of diagrams or using equation of motion method. As discussed in section 2.7, Σ^r describes how electrons interact inside the system, thus it is given by the tunneling matrix element $t_{\alpha\gamma}$. On the other hand, $\Sigma^<$ represents the interaction with the outside world. Since the unperturbed Hamiltonian is chosen to be a closed system (including the leads, and the two QD's in our case), we have $\Sigma_{\alpha\gamma}^< = 0$. Our starting point is the Green's functions g_0 , for which all the interaction

terms are turned-off, that is $t_{id} = t_{\alpha ki} = 0$. In Fourier space, we have[107]

$$\begin{aligned}
g_{0ii}^r &\equiv \mathcal{F} \left[-i\Theta(t) \langle \{ \hat{a}_i(t), \hat{a}_i^\dagger(0) \} \rangle \right] = (\epsilon - \epsilon_i + i0^+)^{-1} \\
g_{0d}^r &\equiv \mathcal{F} \left[-i\Theta(t) \langle \{ \hat{f}(t), \hat{f}^\dagger(0) \} \rangle \right] = (\epsilon - \tilde{\epsilon}_d + i0^+)^{-1} \\
g_{0ii}^< &\equiv \mathcal{F} \left[i \langle \{ \hat{a}_i(0), \hat{a}_i^\dagger(t) \} \rangle \right] = 2\pi i \langle n_i \rangle \delta(\epsilon - \epsilon_i) \\
g_{0d}^< &\equiv \mathcal{F} \left[i \langle \{ \hat{f}(0), \hat{f}^\dagger(t) \} \rangle \right] = 2\pi i \langle n_d \rangle \delta(\epsilon - \tilde{\epsilon}_d),
\end{aligned} \tag{6.7}$$

where \mathcal{F} represents Fourier transformation. Now, let's turn on the coupling to the leads, $t_{\alpha ki}$ only, and denote the new Green's functions by g . This is the well-known problem of resonant transmission through a non-interacting system[108]. By applying Dyson-Keldysh equations or using equation of motion method, it can be shown that Green's functions in the QD₁ are given by

$$(g^r)^{-1} = \begin{bmatrix} \epsilon - \epsilon_1 & 0 & 0 \\ 0 & \epsilon - \epsilon_2 & \vdots \\ 0 & \dots & \dots \end{bmatrix} + \frac{i}{2}(\Gamma^R + \Gamma^L), \tag{6.8}$$

with

$$\Gamma_{ij}^\alpha(\epsilon) \equiv 2\pi \sum_k t_{ki\sigma}^{\alpha*} t_{kj\sigma}^\alpha \delta(\epsilon - \epsilon_{k\alpha}), \tag{6.9}$$

and

$$g^< = g^r i(\Gamma^L f_L + \Gamma^R f_R) g^a. \tag{6.10}$$

In the QD₂, we have $g_d = g_{0d}$, obviously. We now open the coupling between the two QD's, and calculate G_{ij}^r :

$$G_{ij}^r = g_{ij}^r + \sum_{\beta\gamma} G_{i\beta}^r \Sigma_{\beta\gamma}^r g_{\gamma j}^r, \tag{6.11}$$

where β and γ run over all the states. Using Eq.6.6, we obtain

$$G_{ij}^r = g_{ij}^r + \sum_{lm} g_{il}^r \tilde{t}_{ld} G_d^r \tilde{t}_{md} g_{mj}^r, \tag{6.12}$$

where the summation runs over the QD₁ states only. Again by applying Dyson equation we can calculate G_d^r . This gives

$$G_d^r = ((g_d^r)^{-1} - \sum_{ij} \tilde{t}_{id} g_{ij}^r \tilde{t}_{jd})^{-1}. \tag{6.13}$$

Now, we need to calculate b and λ . b is giving by

$$b^2 = 1 - 2\langle f_\sigma^\dagger f_\sigma \rangle = 1 - 2(-i \int \frac{d\epsilon}{2\pi} G_d^<). \quad (6.14)$$

Also, using equation of motion for b , $-i\partial_t b = [b, H]$, we find

$$\lambda b^2 = i \sum_{i\sigma} \tilde{t}_{id} \int \frac{d\epsilon}{2\pi} G_{id}^<. \quad (6.15)$$

We will now use Keldysh equation with $\Sigma^< = 0$ to calculate $G_d^<$ and $G_{id}^<$:

$$G_d^< = (1 + \sum_i G_{di}^r \tilde{t}_{id}) g_d^< (1 + \sum_j \tilde{t}_{jd} G_{jd}^a) + \sum_{ij} G_d^r \tilde{t}_{id} g_{ij}^< \tilde{t}_{jd} G_d^a. \quad (6.16)$$

Realizing that $G_d^r/g_d^r = 1 + \sum_i G_{di}^r \tilde{t}_{id}$, we have

$$G_d^< = G_d^r (g_d^r)^{-1} g_d^< (g_d^a)^{-1} G_d^a + \sum_{ij} G_d^r \tilde{t}_{id} g_{ij}^< \tilde{t}_{jd} G_d^a. \quad (6.17)$$

Using Eqs.6.7, first term at the right side cancels, and we obtain

$$G_d^< = \sum_{ij} G_d^r \tilde{t}_{id} g_{ij}^< \tilde{t}_{jd} G_d^a. \quad (6.18)$$

Similarly, for $G_{di}^<$, we find

$$G_{di}^< = G_d^r \sum_{lm} \tilde{t}_{ld} g_{lm}^< (\delta_{mi} + \tilde{t}_{md} G_{di}^a). \quad (6.19)$$

But,

$$\begin{aligned} G_{ji}^a &= g_{ji}^a + \sum_m g_{jm}^a \tilde{t}_{md} G_{di}^a, \\ \sum_j (g_{mj}^a)^{-1} G_{ji}^a &= \delta_{mi} + \tilde{t}_{md} G_{di}^a. \end{aligned} \quad (6.20)$$

Thus,

$$G_{di}^< = G_d^r \sum_{lmj} \tilde{t}_{ld} g_{lm}^< (g_{mj}^a)^{-1} G_{ji}^a. \quad (6.21)$$

For simplicity, we will now take the $\Gamma_{ij}^\alpha \approx \Gamma^\alpha \delta_{ij}$, and $t_{id} \approx t$. Within these approximations, equations that we need to solve can be summarized as follow:

$$\begin{aligned}
g_{ii}^r &= [\epsilon - \epsilon_i + \frac{i}{2}(\Gamma^R + \Gamma^L)]^{-1} \\
g_{ii}^< &= i \frac{\Gamma^L f_L + \Gamma^R f_R}{(\epsilon - \epsilon_i)^2 + (\Gamma^L + \Gamma^R)^2/4} \\
G_d^r &= (\epsilon - \tilde{\epsilon}_d - \tilde{t}^2 \sum_i g_{ii}^r)^{-1} \\
G_{ij}^r &= g_{ii}^r \delta_{ij} + g_{ii}^r \tilde{t} G_d^r \tilde{t} g_{jj}^r \\
G_d^< &= \sum_i G_d^r \tilde{t} g_{ii}^< \tilde{t} G_d^a \\
G_{di}^< &= \sum_j G_d^r \tilde{t} g_{jj}^< (g_{jj}^a)^{-1} G_{ji}^a \\
b^2 &= 1 - 2\text{Im} \int \frac{d\epsilon}{2\pi} G_d^< \\
\lambda b^2 &= i \sum_{i\sigma} \int \frac{d\epsilon}{2\pi} \tilde{t} G_{di}^<.
\end{aligned} \tag{6.22}$$

These equations must be solved self-consistently for λ and b . A convenient way is to fix $\tilde{\epsilon}_d$ as an input parameter instead of fixing ϵ_d . Then, we can solve the self-consistent problem for b only, and calculate λ afterwards.

6.4 Results

The simplest case occurs when we only have one channel in the QD₁. In Fig.6.3, we plot small bias conductance as a function of QD₂ energy ϵ_d . given by

$$G = \left(\frac{dI}{dV} \right)_{\Delta V=0} = 2e \frac{\Gamma^R \Gamma^L}{\Gamma^R + \Gamma^L} \text{Im} \sum_{\sigma} \int \frac{d\epsilon}{2\pi} \partial_{\epsilon} f(\epsilon) \sum_i G_{ii}^r(\epsilon). \tag{6.23}$$

In the calculations, we use coupling parameters $\Gamma^R = \Gamma^L = \Gamma = 0.2$ and $t = 0.5$. G_0 represents the conductance without QD₂. In all the figures, the energy scale is renormalized in unit of Γ . Experimentally, ϵ_d can be controlled by applying a gate voltage. As expected, for high values of ϵ_d , G/G_0 approaches unity. At low temperature, and $\epsilon_d \approx -1$, we observe a clear dip in the conductance which is due to Kondo resonance between the two QD₁ and QD₂ channels; the spin up and spin down electrons in the QD₁ can tunnel into QD₂ for very short times $\approx \hbar/|\epsilon_i - \epsilon_d|$, and the phase-coherent superposition of all possible tunneling events gives rise to a spin-singlet in QD₂. In Kondo regime, the average occupation number n_{σ} of the

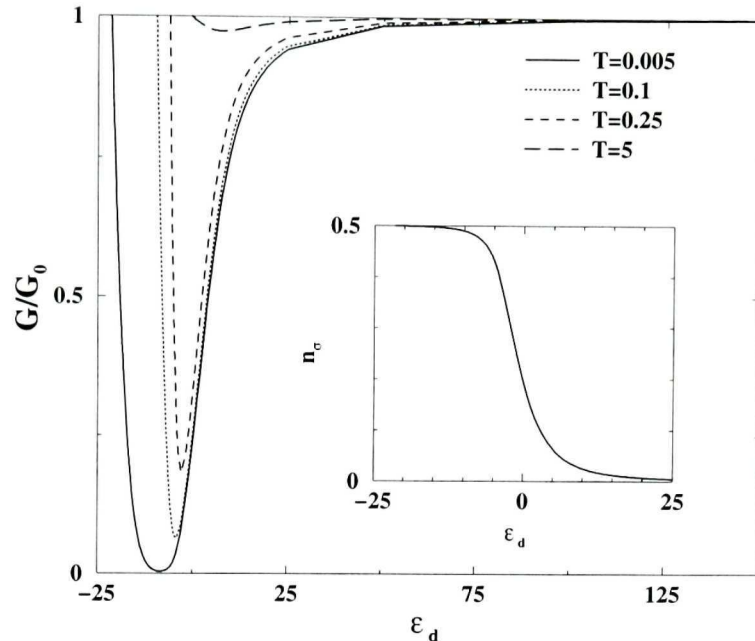


Figure 6.3: Conductance as a function of QD₂ energy level for different temperatures. G_0 is the conductance for $\epsilon_d \rightarrow \infty$. Inset shows the average occupation number n_σ of QD₂. All the energy scale is renormalized in unit of Γ in this figure and in subsequent figures.

QD₂ approaches unity, as we can see in the inset of Fig.6.3. As the temperature is increased, Kondo resonance is destroyed and the current is recovered.

In Fig.6.4, we plot the *local density of states* (LDOS) inside QD₁ for different values of ϵ_d and at $T = 0.001$, giving by

$$\text{LDOS}_1(\epsilon) = -\frac{1}{\pi} \text{Im} \sum_i G_{ii}^r(\epsilon). \quad (6.24)$$

At $\epsilon_d = 20$, the coupling to QD₁ is ineffective and we simply have a resonant tunneling peak with width $\approx \Gamma$, near $\epsilon = 0$. As ϵ_d decreased, a new peak approaches from right due to coupling with QD₂. In Kondo regime, the two peaks overlap and a strong dip whose width decreases exponentially with ϵ_d , appears. The Kondo temperature, *i.e.* the temperature above which the phase-coherent co-tunneling between the free electrons and the strongly interacting system is destroyed, is proportional to the width of this dip. As a result, if the temperature is smaller than the Kondo temperature, current is suppressed. When ϵ_d is decreased further, Kondo temperature becomes too small, so that Kondo resonance is destroyed and current is recovered (see Fig.6.3).

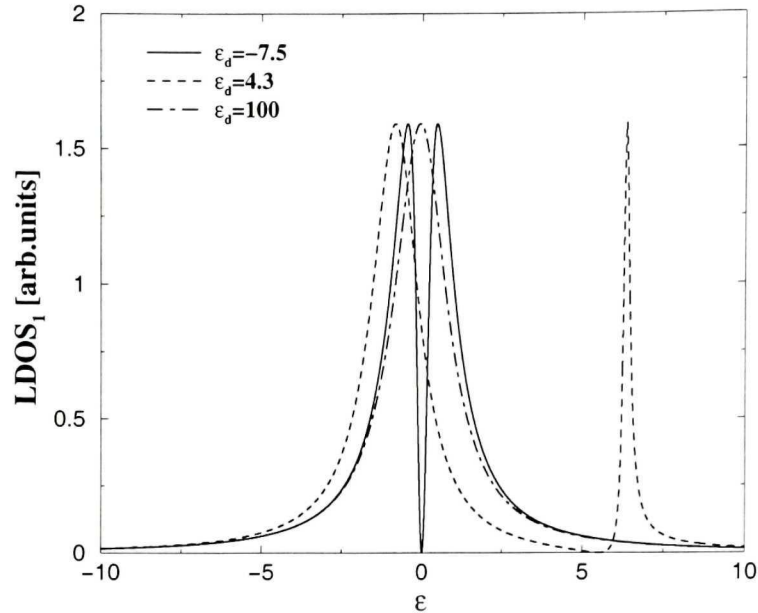


Figure 6.4: Local density of states inside QD₁ at different QD₂ energy levels. A narrow Kondo dip appears for small values of ϵ_d .

These result also agree with Ref.[131], where the authors investigate conductance properties of a quantum wire coupled to a quantum dot.

We now investigate the effect of including many levels inside QD₁. In Fig. 6.5, we consider 5 channels with different energy separations $\Delta\epsilon_i$. Channels are placed such that two of them are below the Fermi energy μ of the leads, two others are above μ , and one channel is aligned with μ . Compared to the case of $\Delta\epsilon_i \rightarrow \infty$, we see that when many channels are present, current is not completely suppressed anymore. This is because more electrons can now participate to the transport, while in Kondo regime the average number of electrons in Kondo resonance remains always $2n_\sigma \approx 1$. We also observe a slight displacement of Kondo minimum towards left. In fact, in the presence of several channels, probability of spin fluctuations is higher. This is also seen in the inset of Fig.6.5; the ϵ_d dependence of n_σ is smoothed due to fluctuations through several channels. As a result, Kondo temperature is higher, and for a given temperature T , Kondo minimum occurs at lower ϵ . In Fig.6.6, we show the growth of Kondo peak inside QD₂ with decreasing ϵ_d . The transition from a smoother local

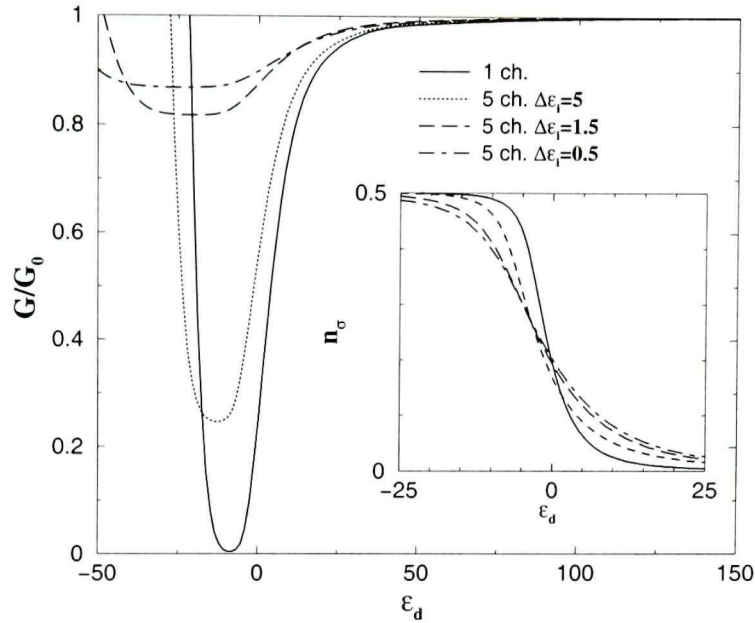


Figure 6.5: Conductance as a function of ϵ_d of a 5 channel QD₁ for different energy separation of the channels. Inset shows the average occupation number in QD₂, as a function of ϵ_d .

density of states to the sharp resonant behavior as a function of ϵ_d is clear.

In Fig.6.7, we study the effect of applying a gate voltage V_g to the QD₁ on the zero bias conductance. The spacing between QD₁ energy levels is fixed to 0.3, and we consider 11 channels to ensure a periodic behavior of transport properties as a function of V_g . We use the same coupling parameters t and Γ as in previous calculations. Results are obtained for 11 values of V_g between -0.15 and 0.15 (one complete period). As we can see from the figure, for non-zero V_g , the behavior of the conductance as a function of ϵ_d can be different. For instance, when the energy of the channel initially aligned with the Fermi energy μ is slowly increased by applying a small $V_g = 0.06$, the conductance G first increases with a decreasing ϵ , then G starts decreasing. This yields to a very interesting V_g dependency of conductance as shown in Fig.6.8: by varying ϵ_d from very high values to low values, it is possible to reverse the phase of oscillations of the conductance. To see why, let's first consider $\epsilon_d = 100$. In this case, coupling between the two QD's is negligible, and we simply have resonant transmission through non-interacting dot levels, *i.e.* the conductance

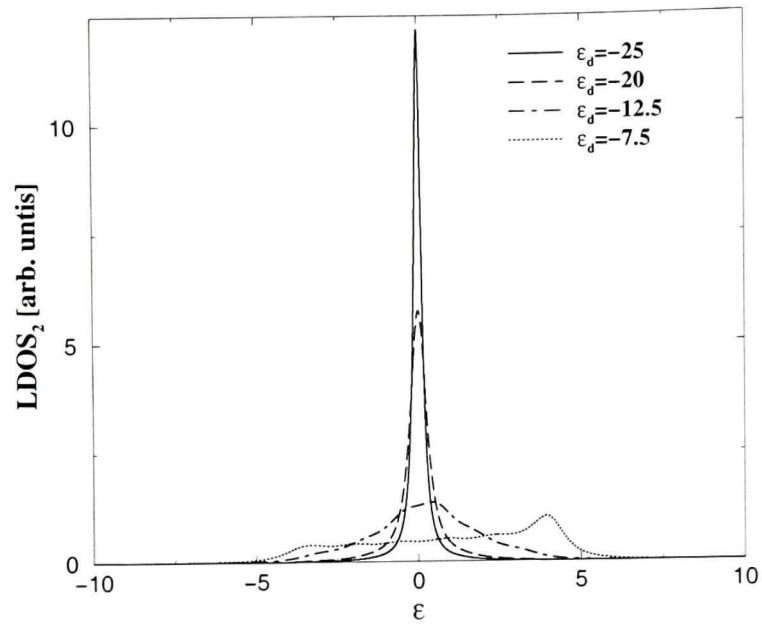


Figure 6.6: Local density of states in QD₂. Kondo peak is enhanced as ϵ_d is decreased.

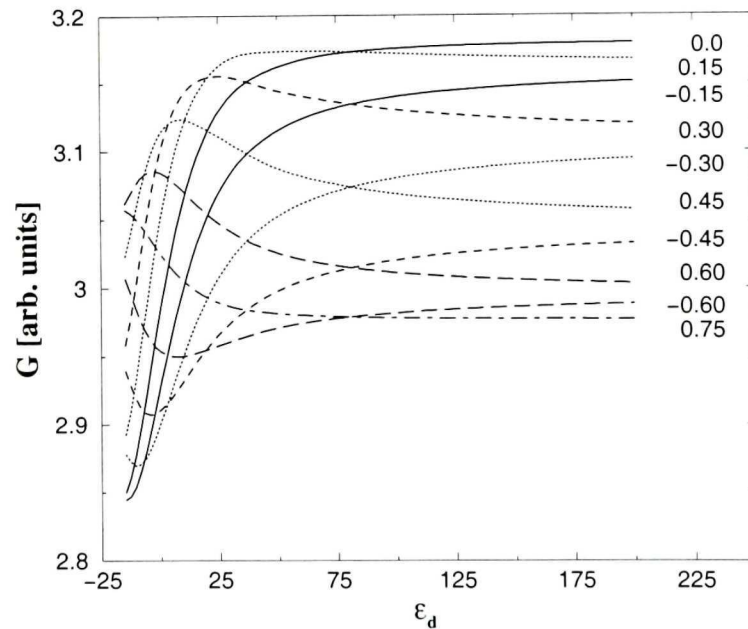


Figure 6.7: Conductance as a function of QD₂ energy level ϵ_d , for different gate voltages applied to QD₁. When a transport channel inside QD₁ is not aligned with the Fermi level of the leads, decreasing ϵ_d may lead to an increasing in conductance.

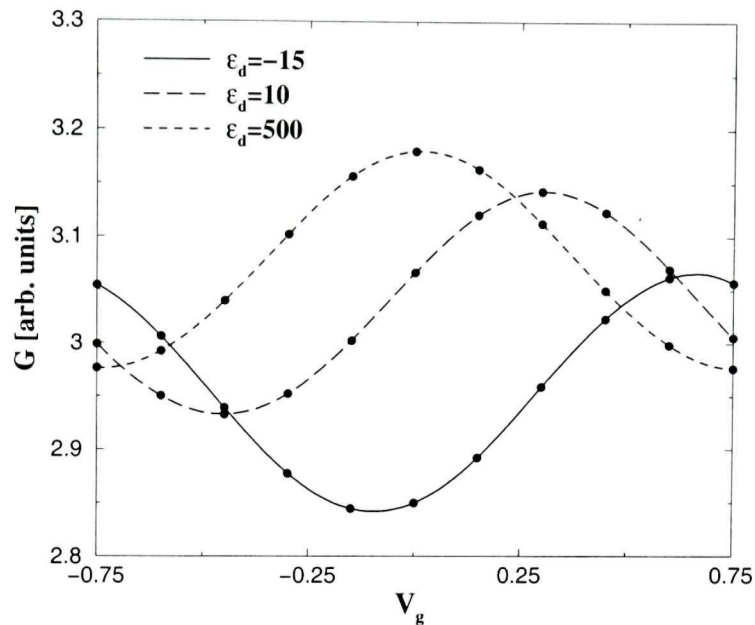


Figure 6.8: Conductance as a function of gate voltage V_g applied to QD₁, for different ϵ_d .

is maximized when $V_g = \mu = 0$. For $\epsilon_d = -3$, Kondo effect becomes important such that the conductance is minimized when $V_g = \mu = 0$. On the other hand for non-zero V_g , the Kondo scattering becomes inefficient, thus, electrons which were in Kondo resonance can now participate to the tunneling current. For medium values of ϵ_d , there is a complex competition between Kondo scattering and resonant transmission giving rise to a dephased oscillation as a function of applied gate voltage.

6.5 Summary

In conclusion, we have studied the Kondo correlation in a QD molecule, between quantized transport channels of the a QD and a strongly interacting QD. We have shown that while the linear conductance can be completely suppressed due to Kondo scattering when there is only one transport channel, in the presence of several channels, current is partially recovered when energy gap between the channels is decreased. We have also studied the effect of applying a gate voltage to the conducting QD. When the principal conduction channel is not aligned with the Fermi energy of the leads,

Kondo effect is reduced, which gives rise to an interesting competition between the resonant tunneling and Kondo scattering. As a result, by tuning the energy level of the interacting QD, it is possible to reverse the oscillatory phase of the conductance as a function of gate voltage.

Conclusion

Both for experimental and theoretical studies, there is a growing interest in quantum dots since they provide a powerful tool for investigating the physics of small, coherent quantum systems. Especially, the ability to control their shape, size, number of electrons, and interaction strength experimentally has made them very attractive to physicists. So far, theoretical and experimental investigations of QD physics have advanced the understanding of many-body phenomena, the electron transport features in nanoelectronic devices, as well as generating novel device concepts.

While the basics physics of important transport features for a QD weakly coupled to external leads such as Coulomb blockade, spin blockade, and Kondo effect have been well understood, these small artificial structures continue providing several new physical effects which require detailed investigations based on quantum physics. In this thesis, we have investigated several different quantum dot structures, in order to elucidate complex physical effects arising from competing electron-electron interactions, magnetic field, geometrical factors, and strong couplings.

The techniques that we used in this thesis were based on many-body formalism, since our primary goal was to understand full quantum mechanical effects, including electronic correlations. The basic principles of many-body physics, as well as advanced analysis techniques such as exact diagonalization, quantum Monte Carlo, Hartree-Fock, and Keldysh Green's function formalism, were presented in detail in chapter 2. We have also emphasized how they are implemented, the advantages of each method, and in which cases they are beneficial or powerless from a practical point of view.

In chapter 3, we have investigated cylindrical QD's with a circular harmonic con-

finement potential under magnetic field. We have introduced Fock-Darwin wave functions that are used as a basis set also in the subsequent chapters. By combining exact diagonalization results with Keldysh Green's function formalism, we were able to study the many-body transport properties. We have shown that current-voltage characteristics depend strongly on electronic correlations inside the dot especially when an external magnetic field is applied. Moreover, numerical and analytical calculations for zero magnetic field shows that transport properties reveals the shell structure of the system.

In chapter 4, we have studied a ring-shaped QD structure having two potential minima. Such potential landscape provides a competition of various contributions to the total energy by spatially separating electrons. Such effects have interesting implications for tunneling current in the Coulomb blockade regime. at least for cases involving a small number of strongly interacting electrons as we have studied. By localizing in different potential minima, the total ground state energy is minimized. However, due to the energetics competition, adding an electron to the QD may involve a charge redistribution between the two potential minima. We found that this redistribution occurs abruptly as the magnetic field is increased. A most interesting outcome of the redistribution is a new blockade phenomenon which is caused by a drastic reduction of the spectral weight for the transition from a $(N - 1)$ -electron QD to a N -electron QD due to the spatial localization of the electrons. This geometric blockade leads to a drastic reduction of the tunneling current which should be measurable experimentally.

Chapter 5 was devoted to the study of the effect of random disorder in a parabolic confinement potential on the electronic structure up to 13 electrons by DQMC method. DQMC is shown to give excellent total energy and spin configuration for clean-QD's as compared with exact diagonalization, and is very powerful for investigating disordered QD's which do not possess any spatial symmetry. Compared with the UHF technique, DQMC gives superior advantages in total energy accuracy, especially for low magnetic field before the transition to maximum density droplet states. Disorder

is found to have very significant effects to the total energy of QD. In particular, the energetic transition (the kinks in energy) between many-body states is made much less clear due to disorder, and the required magnetic field to induce such transitions may be rather different than that of clean-QD, this may have important implications to interpreting tunneling spectroscopy data. We found that Hund's rule for closed shell is robust against even strong disorder, but less so for open shells. For the lower shells, the spin states are largely unaffected by disorder, but for higher shells (larger number of electrons N) this may change due to disorder.

In chapter 6, the effect Kondo resonance between several quantized transport channels and a spin impurity was studied. Such phenomena should occur when a large QD dot is coupled to a smaller one for which electron-electron interactions are more important. In contrast with the previous chapters where the many-body problem is solved in a continuous potential landscape, we have used a tight-binding Hamiltonian model that we have expanded in terms of Keldysh Green's functions. By solving the problem in the slave-boson approximation, we have shown that the competition between resonant transport and Kondo resonance yields to very interesting current-voltage oscillations.

There are of course several improvements that can be done in the research line that we have taken. Our study of transport properties in correlated systems, calculations of Green's functions were restricted to first order while including the coupling to the leads. It would be interesting to see how an exact treatment of the leads may affect transport properties. With the increasing computational powers, such calculations should become possible.

For quantum Monte Carlo calculations, a critical step is the construction of trial wave functions. In this work, we used Hartree-Fock solutions. Another possibility is to perform a density-functional calculation, which might give in some cases better trial waves. Also, including a Jastrow factor for variational quantum Monte Carlo calculations might improve the trial functions. An improved Jastrow factor can also allow the calculation of the many-body spectral function as discussed in section 2.7.4.

This would be very interesting and very important for transport calculations. Moreover, in our quantum Monte Carlo algorithm, Fock-Darwin states are used as a basis set. Implementation of a more general grid basis set should improve computation time, especially when the potential confinement is not perfectly parabolic, such as in a quantum dot molecule.

Appendices

A.1 Two-body interaction terms in Fock-Darwin basis set

In order to perform exact diagonalization using the Fock-Darwin basis set (see section 3.2), one needs to calculate the two-body interaction terms given by Eq. (2.17). Using Fock-Darwin wave functions, we obtain

$$v_{ijkl} = 4\pi^2 l^3 \delta_{m_i+m_j, m_k+m_l} K_i K_j K_k K_l \int_0^\infty dk I_{ki}(k) I_{jl}(k) F(k), \quad (\text{A.1})$$

where K_i is given in equation 3.3, and

$$\begin{cases} I_{ki}(k) \equiv \int dr r^{|m_i|+|m_k|+1} e^{-\frac{r^2}{2}} L_{n_i}^{|m_i|}(\frac{r^2}{2}) L_{n_k}^{|m_k|}(\frac{r^2}{2}) J_{m_k-m_i}(kr) \\ F(k) \equiv \int dz_1 dz_2 e^{-\frac{k}{l}(z_>-z_<)} Z_{\nu_i}(z_1) Z_{\nu_k}(z_1) Z_{\nu_j}(z_2) Z_{\nu_l}(z_2) \end{cases}. \quad (\text{A.2})$$

Usually, confinement in z -direction is much smaller so that calculation of $F(k)$ can be restricted to lowest level $\nu_i = \nu_j = \nu_k = \nu_l = 1$. Furthermore, this expression can be further simplified if we assume that $z_> - z_< \approx 0$ for a narrow well, which gives $F(k) \approx 1$. From numerical point of view this approximation has a great advantage since the double integrations do not depend anymore on the magnetic field. We have tested the effect of including $F(k)$ in our calculations for typical values of $\hbar\omega_0$ (≈ 5 meV) and well width (≈ 10 nm), and we have found that including a finite well thickness sustains the electron-electron interaction slightly as expected. In the following, we derive an analytical form for $F(k)$ for an infinite confinement potential. The lowest level wave function for a infinite well width a is given by

$$Z(z) = \sqrt{\frac{2}{a}} \sin\left(\frac{\nu\pi z}{a}\right), \quad (\text{A.3})$$

with $\nu = 1$. Then, we have

$$\begin{aligned} F(k) &= 4 \int_0^1 dz_1 dz_2 e^{-\frac{ka}{l}(z_>-z_<)} \sin^2(\pi z_1) \sin^2(\pi z_2) \\ &= 4 \int_0^1 dz_2 \sin^2(\pi z_2) \left\{ \int_0^{z_2} dz_1 e^{-\frac{ka}{l}(z_2-z_1)} \sin^2(\pi z_1) + \int_{z_2}^1 dz_1 e^{-\frac{ka}{l}(z_1-z_2)} \sin^2(\pi z_1) \right\}. \end{aligned}$$

The evaluation of these integrals is tedious but straightforward. It gives

$$F(k) = \frac{2}{\kappa} \left[1 + (e^{-\kappa} - 1) \frac{16\pi^4}{\kappa} (\kappa^2 + 4\pi^2)^{-2} + \kappa^2 (\kappa^2 + 4\pi^2)^{-1} \right],$$

where $\kappa \equiv ka/l$. This function slowly decreases with k at a rate determined by a/l . We have tested the effect of including $F(k)$ in our calculations for typical values of $\hbar\omega_0 \approx 5$ meV and well width $a \approx 10$ nm, and we have found that finite well thickness sustains the electron-electron interaction slightly as expected. We have also performed calculations by mixing second confinement level $\nu = 2$, which was found to be negligible.

A.2 Drift velocity and local energy in fixed-phase DQMC

In DQMC method, one needs to evaluate the drift velocity $\mathbf{v}_D(\mathbf{R})$ and local energy $E_L(\mathbf{R})$. As discussed in section 2.6.1, they are given by

$$\begin{aligned}\mathbf{v}_D(\mathbf{R}) &= \Psi_T(\mathbf{R})^{-1} \nabla \Psi_T(\mathbf{R}) \\ E_L(\mathbf{R}) &= \Psi_T(\mathbf{R})^{-1} \hat{H} \Psi_T(\mathbf{R}),\end{aligned}\tag{A.4}$$

where $\Psi_T(\mathbf{R})$ is a trial wave function which can be written as

$$\Psi_T(\mathbf{R}) = e^{i\Theta(\mathbf{R})} A(\mathbf{R}),\tag{A.5}$$

where A is the amplitude of the wave function. Then the drift velocity becomes

$$\mathbf{v}_D(\mathbf{R}) = A^{-1} \nabla A - i \nabla \Theta.\tag{A.6}$$

In fixed-phase approximation, the expectation value of the imaginary part of $\langle \mathbf{v}_D(\mathbf{R}) \rangle$ must give zero. Thus, we define a modified drift velocity, used for numerics, as

$$\tilde{\mathbf{v}}_D(\mathbf{R}) = A^{-1} \nabla A\tag{A.7}$$

For the calculation of the local energy, let's write the Fock-Darwin Hamiltonian in effective atomic units

$$\begin{aligned}\hat{H} &= \sum_j^N \frac{1}{2} (\mathbf{p}_j + \mathbf{A}_j)^2 + \frac{1}{2} \omega_0 r_j^2 + g^* B s_z^j + \sum_{i < j}^N \frac{1}{|\mathbf{r}_i - \mathbf{r}_j|} \\ &= \sum_j^N \frac{1}{2} \left(-\nabla_j^2 + \omega^2 r_j^2 + B(L_z^j + 2g^* s_z^j) \right) + \sum_{i < j}^N \frac{1}{|\mathbf{r}_i - \mathbf{r}_j|},\end{aligned}\tag{A.8}$$

with $L_z^j = \partial_{\Theta_j}$. We have

$$\begin{aligned}\nabla_j^2 \Psi_T &= \nabla_j^2 (e^{i\Theta} A) \\ &= e^{i\Theta} \left[\nabla_j^2 - (\nabla_j \Theta)^2 + i2(\nabla_j \Theta) \nabla_j + i(\nabla_j^2 \Theta) \right] A,\end{aligned}\tag{A.9}$$

and

$$\begin{aligned}L_z^j \Psi_T &= L_z^j (e^{i\Theta} A) \\ &= e^{i\Theta} \left[(\partial_{\Theta_j} \Theta) - i \partial_{\Theta_j} \right] A.\end{aligned}\tag{A.10}$$

As before, since expectation value of $E_L(\mathbf{R})$ must be a real quantity, we only need consider the real part in the numerical calculations:

$$\tilde{E}_L(\mathbf{R}) \equiv \text{Re}\{E_L(\mathbf{R})\} = A^{-1}\hat{H}_{eff}A, \quad (\text{A.11})$$

with

$$\hat{H}_{eff} \equiv \frac{1}{2} \sum_j^N \left(-\nabla_j^2 + (\nabla_j \Theta)^2 + \omega^2 r_j^2 + B(\partial_{\Theta_j} \Theta + 2g^* s_z^j) \right) + \sum_{i < j}^N \frac{1}{|\mathbf{r}_i - \mathbf{r}_j|}. \quad (\text{A.12})$$

To summarize, we use equations A.7 and A.11 in the numerical calculations.

A.3 Matrix elements for a Gaussian perturbation in Fock-Darwin basis set

In section 5.1, we model the impurity term in the single-electron Hamiltonian by a two-dimensional Gaussian profile:

$$V^{imp} = e^{-\frac{|\mathbf{r}-\mathbf{r}_0|^2}{2\sigma^2}}. \quad (\text{A.13})$$

Thus, in Hartree-Fock calculations, we need to calculate the following integrals:

$$\langle i|\hat{V}^{imp}|j\rangle = \int r dr d\Theta \phi_i(r, \Theta) V^{imp} \phi_j(r, \Theta), \quad (\text{A.14})$$

where $\phi(r, \Theta)$'s are Fock-Darwin wave functions (see section 3.2), and V^{imp} can be written as

$$V^{imp} = e^{-\frac{r^2+r_0^2}{2\sigma^2}} e^{\frac{rr_0}{\sigma^2} \cos(\Theta-\Theta_0)}. \quad (\text{A.15})$$

Then, we obtain

$$\langle i|\hat{V}^{imp}|j\rangle = e^{-i(m_i-m_j)\Theta_0} \int d\Theta dx f_i(x) f_j(x) e^{-i(m_i-m_j)\Theta} e^{-\frac{r^2+r_0^2}{2\sigma^2}} e^{\frac{rr_0}{\sigma^2} \cos(\Theta-\Theta_0)}, \quad (\text{A.16})$$

where $x \equiv \frac{r^2}{2a^2}$, and

$$f(x) \equiv \left(\frac{n!}{(n+|m|)!} \right)^{\frac{1}{2}} e^{-x/2} x^{|m|/2} L_n^{|m|}(x). \quad (\text{A.17})$$

Angular part of the Eq.A.16 is given by

$$S_\Theta \equiv \int d\Theta e^{-i(m_i-m_j)\Theta} e^{\frac{rr_0}{\sigma^2} \cos\Theta}, \quad (\text{A.18})$$

and it can be evaluated in terms of *modified Bessel functions* $I_n(x)$ as

$$S_\Theta = 2\pi I_{m_i-m_j}\left(\frac{rr_0}{\sigma^2}\right). \quad (\text{A.19})$$

For numerical calculations, it is also useful to consider the asymptotic behavior of the Bessel function, to prevent divergence problems:

$$I_n(x > 600) \approx \frac{e^x}{\sqrt{2\pi x}}, \quad (\text{A.20})$$

and the exponential e^x cancels out when inserted in the Eq.A.16.

Note that the factor $e^{-i(m_i-m_j)\Theta_0}$ in Eq.A.16 makes the Hartree-Fock Hamiltonian and its solutions complex. Therefore, DQMC calculations must be done in the fixed-phase approximation, even if there is no magnetic field.

A.4 Description of exact diagonalization code

Our exact diagonalization software is divided into three main codes (see Fig.A.1). In the following, we describe these three main steps, as well as the important input/output files.

- **Intpot:** Short for interaction potential, this code calculates the two-body interaction elements given by the Eq.A.1. User must specify if the z -direction will be taken into account, as well as the range of angular and Landau level quantum numbers for which all non-zero elements will be calculated and written in an output file.
- **XDN:** Short for exact diagonalization for N -electrons, XDN is the main part of the calculations. In the input file *input_XDN*, user must specify number of electrons, magnetic field, parabolicity of the confinement potential, single particle levels used to construct Slater determinants, and good quantum numbers L and S_z for which the subspaces will be calculated using the Eq.2.21. The matrices that are smaller than the size specified in the input file are diagonalized by a conventional diagonalization technique, and the results are written in *DDresults*. For bigger matrices, XDN only calculates the matrix elements, which are then written in input files for each subspace, for Lanczos diagonalization.
- **Lanczos:** This is a conventional Lanczos diagonalization algorithm which uses the input file *input_Lanczos* supplied by XDN. Results are written in *LDresults*.

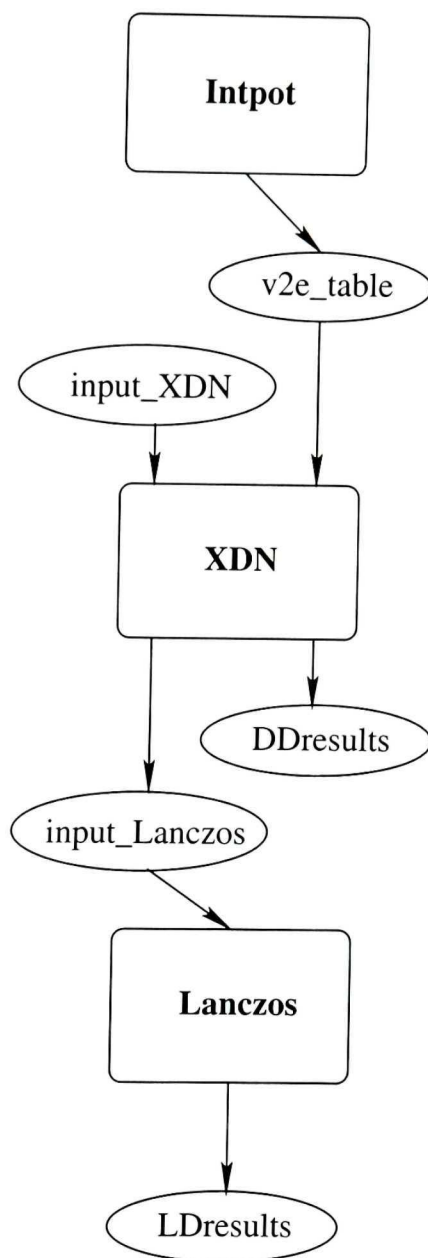


Figure A.1: Input/output flow chart of exact diagonalization calculations. The main codes are **Intpot** (calculation of two-body interaction potential elements), **XDN** (construction of different many-body Hamiltonian subspaces and diagonalization), and **Lanczos** (diagonalization). Input and output files are shown in ellipses.

A.5 Description of quantum Monte Carlo code

Main codes and important input/output files of our quantum Monte Carlo software are schematized in Fig.A.2. The software package is divided into three main steps:

- **HF:** This is the Hartree-Fock code. In the input file denoted as *job* (see Fig.A.2), number of electrons, magnetic field, harmonic confinement parabolicity, number of single electron states, number of Gaussian impurities and their parameters must be specified. The code first calculates non-interacting Hamiltonian. Then Hartree-Fock iterations are performed until the convergence is reached. The file *Hashtable* contains two-body interaction terms, and it is updated during the iterations if necessary. The file *results.hf* contains Hartree-Fock eigenenergy, while Hartree-Fock wave functions for spin-up and spin-down electrons are written in *job_u.wav* and *job_d.wav* files. The file *job.in* contains the information on trial waves that are necessary for QMC calculations.
- **QMC:** The quantum Monte Carlo code needs *job.in* file where the trial wave function is specified. Walkers positions are initialized randomly unless a *job.cfg* file where walkers positions are specified, already exists. Once the equilibrium state is reached, average values for the energy are collected in each iteration. Walkers positions are also written in *job.den* in regular time intervals, for the calculation of electron density.
- **DenCal:** Short for density calculation, this code is an analysis tool which calculates spin-up and spin-down electronic densities. It needs Hartree-Fock wave functions, as well as the walkers positions from which the QMC density is calculated. QMC densities for spin-up and spin-down electrons are written in *job_u.qmc* and *job_d.qmc* files respectively. An extrapolation between the Hartree-Fock and QMC densities is performed as given in Eq.2.63, and the results are written in *job_u.out* and *job_d.out* files.

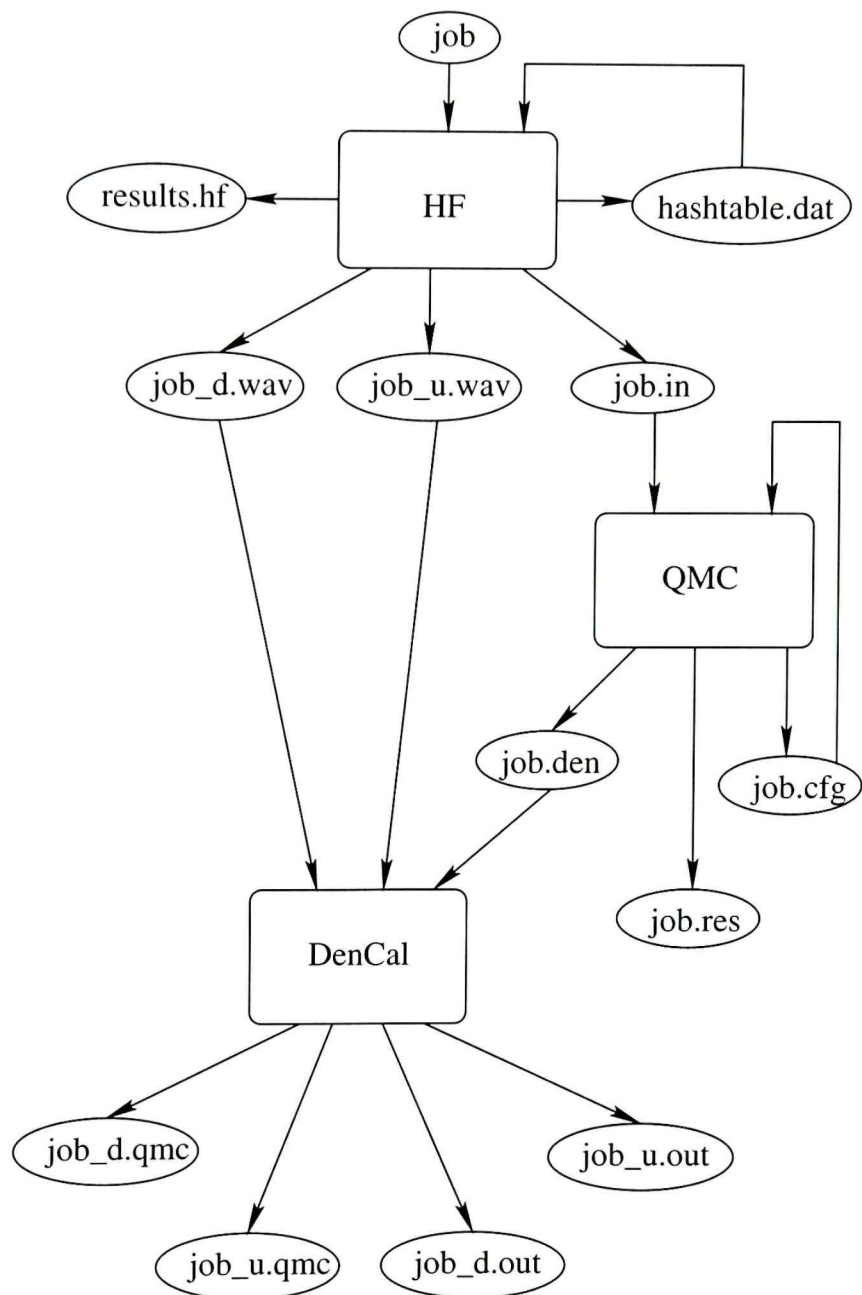


Figure A.2: Input/output flow chart of quantum Monte Carlo calculations. The main codes are HF (Hartree-Fock calculation of trial states), QMC (variational and diffusion quantum Monte Carlo calculations), and DenCal (density calculation). Input and output files are shown in ellipses.

A.6 Publications

- Güçlü A.D, Sun, Q.F., Guo, H., and Harris R., (2003) Kondo effect in a quantum dot molecule. To be submitted to Phys. Rev. Lett.
- Güçlü A.D, Wang, J., and Guo, H., (2003) Disordered quantum dots: a diffusion quantum Monte Carlo study. Accepted for publication in Phys.Rev.B.
- Güçlü A.D, Sun, Q.F., Guo, H., and Harris R., (2002) Geometric blockade in a quantum dot: transport properties by exact diagonalization. Phys.Rev.B. 66: 195327.
- Güçlü A.D and Guo, H. (2003) Exact diagonalization and quantum Monte Carlo studies of quantum dots. High performance computing systems and applications proceedings. 79-85.
- Güçlü A.D, Wang J., and Guo, H. (2003) Diffusion quantum Monte Carlo study of quantum dots. American physical society march meeting. Contributed talk.
- Güçlü A.D, Sun, Q.F., Guo, H. (2002) Geometric blockade: addition spectra of a quantum dot with two potential minima. American physical society march meeting. Contributed talk.
- Wang, J., Güçlü A.D, Guo, H. (2002) Addition spectra of quantum dots by quantum Monte Carlo simulation. American physical society march meeting. Contributed talk.
- Güçlü A.D, Sun, Q.F., Guo, H. (2002) Many-body transport through quantum dots. CERION workshop on advanced materials for nano-science and nano-technology. Poster presentation.

BIBLIOGRAPHY

- [1] M.A. Kastner. *Phys. Today*, 46:24, 1993.
- [2] R.C. Ashoori. *Nature*, 379:413, 1996.
- [3] S.M. Reimann and M. Manninen. *Rev. Mod. Phys.*, 74:1283, 2002.
- [4] Y. Alhassid. *Rev. Mod. Phys.*, 72:895, 2000.
- [5] M.A. Reed, J.N. Randall, R.J. Aggarwall, R.J. Matyi, T.M. Moore, and A.E. Wetsel. *Phys. Rev. Lett.*, 60:535, 1988.
- [6] R.C. Ashoori, H.L. Stormer, J.S. Weiner, L.N. Pfeiffer, S.J. Pearton, K.W. Baldwin, and K.W. West. *Phys. Rev. Lett.*, 68:3088, 1992.
- [7] R.C. Ashoori, H.L. Stormer, J.S. Weiner, L.N. Pfeiffer, K.W. Baldwin, and K.W. West. *Phys. Rev. Lett.*, 71:613, 1993.
- [8] S. Tarucha, D.G. Austing, T. Honda, R.J. van der Hage, and L. P. Kouwenhoven. *Phys. Rev. Lett.*, 77:3613, 1996.
- [9] L. P. Kouwenhoven, T.H. Oosterkamp, M.W.S. Danoesastro, M. Eto, D. G. Austing, T. Honda, and S. Tarucha. *Science*, 278:1788, 1997.
- [10] T.H. Oosterkamp, J.W. Janssen, L.P. Kouwenhoven, D. G. Austing, T. Honda, and S. Tarucha. *Phys. Rev. Lett.*, 82:2931, 1999.
- [11] S. Tarucha, D. G. Austing, Y. Tokura, W.G. van der Wiel, and L. P. Kouwenhoven. *Phys. Rev. Lett.*, 84:2485, 2000.
- [12] A. Szabo and N.S. Ostlund. *Modern quantum chemistry*. McGraw-Hill, New York, 1989.

- [13] P.A. Maksym and T. Chakraborty. *Phys. Rev. Lett.*, 65:108, 1990.
- [14] U. Merkt, J. Huser, and M. Wagner. *Phys. Rev. B*, 43:7320, 1991.
- [15] N.F. Johnson and M.C. Payne. *Phys. Rev. B*, 45:3819, 1992.
- [16] P. Hawrylak. *Phys. Rev. Lett.*, 71:3347, 1993.
- [17] S.R.Eric Yang, A.H. MacDonald, and M.D. Johnson. *Phys. Rev. Lett.*, 71:3194, 1993.
- [18] J.J. Palacios, L. Martin-Moreno, G. Chiappe, E. Louis, and C. Tejedor. *Phys. Rev. B*, 50:5760, 1994.
- [19] J.J. Palacios and P. Hawrylak. *Phys. Rev. B*, 51:1769, 1995.
- [20] A. Wojs and P. Hawrylak. *Phys. Rev. B*, 53:10841, 1996.
- [21] A. Wojs and P. Hawrylak. *Phys. Rev. B*, 56:13227, 1997.
- [22] A. Wojs and P. Hawrylak. *Phys. Rev. B*, 55:13066, 1997.
- [23] N.A. Bruce and P.A. Makysm. *Phys. Rev. B*, 61:4718, 2000.
- [24] R. Berkovits. *Phys. Rev. Lett.*, 81:2128, 1998.
- [25] C.M. Canali. *Phys. Rev. Lett.*, 84:3934, 2000.
- [26] P.Hawrylak, C. Gould, A. Sachrajda, Y. Feng, and Z. Wasilewski. *Phys. Rev. B*, 59:2801, 1999.
- [27] M. Ciorga, A. Sachrajda, P.Hawrylak, C. Gould, P. Zawadski, S. Jullian, Y. Feng, and Z. Wasilewski. *Phys. Rev. B*, 61:16315, 2000.
- [28] J. Kyriakidis, M. Ciorga, A. Sachrajda, and P.Hawrylak. *Phys. Rev. B*, 66:35320, 2002.
- [29] W. M. C. Foulkes, L. Mitas, R. J. Needs, and G. Rajagopal. *Rev. Mod. Phys.*, 73:33, 2001.

- [30] G. Senatore and N.J. March. *Rev. Mod. Phys.*, 66:445, 1994.
- [31] D.M. Ceperley. *Rev. Mod. Phys.*, 67:279, 1995.
- [32] F. Bolton. *Phys. Rev. B*, 54:4780, 1996.
- [33] F. Pederiva, C. J. Umrigar, and E. Lipparini. *Phys. Rev. B*, 62:8120, 2000.
- [34] L. Coletti, F. Pederiva, E. Lipparini, and C. J. Umrigar. *Eur. Phys. J. B*, 27:385, 2002.
- [35] A. Harju, V. A. Sverdlov, and R. M. Nieminen. *Europhys. Lett.*, 41:407, 1998.
- [36] A. Harju, V. A. Sverdlov, R. M. Nieminen, and V. Halonen. *Phys. Rev. B*, 59:5622, 1999.
- [37] A. Harju, S. Siljamaki, and R. M. Nieminen. *Phys. Rev. B*, 60:1807, 1999.
- [38] H. Saarikoski, E. Rasanen, S. Siljamaki, A. Harju, M.J. Puska, and R. M. Nieminen. *Eur. Phys. J. B*, 26:241, 2002.
- [39] S. Siljamaki, A. Harju, R. M. Nieminen, V.A. Sverdlov, and P. Hyvonen. *Phys. Rev. B*, 65:121306, 2002.
- [40] C.H. Mak, R. Egger, and H. Weber-Gottschick. *Phys. Rev. Lett.*, 81:4533, 1998.
- [41] R. Egger, W. Hausler, C. H. Mak, and H. Grabert. *Phys. Rev. Lett.*, 82:3320, 1999.
- [42] J. Harting, O. Mulken, and P. Borrmann. *Phys. Rev. B*, 62:10207, 2000.
- [43] A. D. Guclu, J. Wang, and H. Guo. *Phys. Rev. B*, 68:035304, 2003.
- [44] Y. Wan, G. Ortiz, and P. Phillips. *Phys. Rev. B*, 55:5313, 1997.
- [45] E. Lee, A. Puzder, M. Y. Chou, T. Uzer, and D. Farrelly. *Phys. Rev. B*, 57:12281, 1998.

- [46] B. Reusch, W. Hausler, and H. Grabert. *Phys. Rev. B*, 63:113313, 2001.
- [47] M. Fujito, A. Natori, and H. Yasunaga. *Phys. Rev. B*, 53:9952, 1996.
- [48] H.M. Muller and S.E. Koonin. *Phys. Rev. B*, 54:14532, 1996.
- [49] H. Tamura and M. Ueda. *Phys. Rev. Lett.*, 79:1345, 1997.
- [50] K.-H. Ahn, K. Richter, and In-Ho Lee. *Phys. Rev. Lett.*, 83:4144, 1999.
- [51] C. Yannouleas and U. Landman. *Phys. Rev. Lett.*, 82:5325, 1999.
- [52] A. Cohen, K. Richter, and R. Berkovits. *Phys. Rev. B*, 60:2536, 1999.
- [53] S. Levit and D. Orgad. *Phys. Rev. B*, 60:5549, 1999.
- [54] M.-C. Cha and S.-R. Eric Yang. *Phys. Rev. B*, 61:1720, 2000.
- [55] D. Ullmo and H.U. Baranger. *Phys. Rev. B*, 64:245324, 2001.
- [56] B. Reusch, W. Hausler, and H. Grabert. *Phys. Rev. B*, 63:113313, 2001.
- [57] M. Koskinen, M. Manninen, and S. M. Reimann. *Phys. Rev. Lett.*, 79:1389, 1997.
- [58] S. M. Reimann, M. Koskinen, J. Helgesson, P.E. Lindel of, and M. Manninen. *Phys. Rev. B*, 58:8111, 1998.
- [59] O. Steffens, U. Rossler, and M. Suhrke. *Europhys. Lett.*, 42:529, 1998.
- [60] K. Hirose and N. S. Wingreen. *Phys. Rev. B*, 59:4604, 1999.
- [61] C. A. Ullrich and G. Vignale. *Phys. Rev. B*, 61:2729, 2000.
- [62] K. Hirose, F. Zhou, and N. S. Wingreen. *Phys. Rev. B*, 63:075301, 2001.
- [63] K. Hirose and N. S. Wingreen. *Phys. Rev. B*, 65:193305, 2002.
- [64] D. Goldhaber-Gordon, H. Shtrikman, D. Mahalu, D. Abusch-Magder, U. Meirav, and M. A. Kastner. *Nature*, 391:156, 1998.

- [65] S. M. Cronenwett, T. H. Oosterkamp, and L. P. Kouwenhoven. *Science*, 281:540, 1998.
- [66] J. Schmid, J. Weis, K. Eberl, and K. von Klitzing. *Physica B*, 182:258, 1998.
- [67] H. Akera. *Phys. Rev. B*, 60:10683, 1999.
- [68] H. Imamura, H. Aoki, and P.A. Maksym. *Phys. Rev. B*, 57:R4257, 1998.
- [69] H. Imamura, P.A. Maksym, and H. Aoki. *Phys. Rev. B*, 59:5817, 1999.
- [70] J. Taylor, H. Guo, and J. Wang. *Phys. Rev. B*, 63:245407, 2001.
- [71] M. Di Ventura and N.D. Lang. *Phys. Rev. B*, 65:045402, 2001.
- [72] Y. Meir, N.S. Wingreen, and P.A. Lee. *Phys. Rev. Lett.*, 66:3048, 1991.
- [73] Y. Meir, N.S. Wingreen, and P.A. Lee. *Phys. Rev. Lett.*, 70:2601, 1993.
- [74] N.S. Wingreen, A.-P. Jauho, and Y. Meir. *Phys. Rev. B*, 48:8487, 1993.
- [75] A.-P. Jauho, N.S. Wingreen, and Y. Meir. *Phys. Rev. B*, 50:5528, 1994.
- [76] N.S. Wingreen and Y. Meir. *Phys. Rev. B*, 49:11040, 1994.
- [77] Y. Meir and N.S. Wingreen. *Phys. Rev. Lett.*, 68:2512, 1992.
- [78] J.M. Kinaret, Y. Meir, N.S. Wingreen, P.A. Lee, and Xiao-Gang Wen. *Phys. Rev. B*, 46:4681, 1992.
- [79] J.M. Kinaret, Y. Meir, N.S. Wingreen, P.A. Lee, and Xiao-Gang Wen. *Phys. Rev. B*, 46:9489, 1992.
- [80] N.B. Zhitenev, R.C. Ashoori, L.N. Pfeiffer, and K.W. West. *Phys. Rev. Lett.*, 79:2308, 1997.
- [81] M. Brodsky, N.B. Zhitenev, R.C. Ashoori, L.N. Pfeiffer, and K.W. West. *Phys. Rev. Lett.*, 85:2356, 2000.

- [82] L.P. Rokhinson, L.J. Guo, S.Y. Chou, and D.C. Tsui. *Phys. Rev. B*, 63:035321, 2001.
- [83] S. Luscher, T. Heinzl, K. Ensslin, W. Wegscheider, and M. Bichler. *Phys. Rev. Lett.*, 86:2118, 2001.
- [84] A. Lorke, R.J. Luyken, A.O. Govorov, J. Kotthaus, J.M. Garcia, and P.M. Petroff. *Phys. Rev. Lett.*, 84:2223, 2000.
- [85] T. Chakraborty and P. Pietilainen. *Phys. Rev. B*, 50:8460, 1994.
- [86] K. Varga, P. Navratil, J. Usukura, and Y. Suzuki. *Phys. Rev. B*, 63:205308, 2001.
- [87] A. Emperador, M. Barranco, E. Lipparini, M. Pi, and L. Serra. *Phys. Rev. B*, 59:15301, 1999.
- [88] A. D. Guclu, Q. F. Sun, H. Guo, and R. Harris. *Phys. Rev. B*, 66:195327, 2002.
- [89] P. Y. Yu and M. Cardona. *Fundamentals of semiconductors*. Springer. Verlag, 1996.
- [90] N. W. Ashcroft and N. D. Mermin. *Solid state physics*. Saunders College publishing, New York, 1976.
- [91] E. K. U. Gross, E. Runge, and O. Heinonen. *Many-particle theory*. Adam Hilger, Bristol, 1991.
- [92] D. C. Mattis. *The theory of magnetism*. Harper and Row, New York, 1965.
- [93] G. Arfken. *Mathematical methods for physicists*. Academic Press, San Diago, 1985.
- [94] J. D. Jackson. *Classical electrodynamics*. Wiley, New York, 1962.
- [95] J. K. Cullum and R. A. Willoughby. *Lanczos algorithms for large symmetric eigenvalue computations*. Birkhauser, Boston, 1985.

- [96] W. K. Millan. *Phys. Rev. A*, 138:442, 1965.
- [97] D. M. Ceperley, G. V. Chester, and M. H. Kalos. *Phys. Rev. B*, 16:3081, 1977.
- [98] M. H. Kalos. *J. Comp. Phys.*, 2:257, 1967.
- [99] N. Trivedi and D. M. Ceperley. *Phys. Rev. B*, 41:4552, 1980.
- [100] W. H. Press, B. P. Flannery, S. A. Teukolsky, and W. T. Vetterling. *Numerical recipes*. Cambridge University Press, Cambridge, 1986.
- [101] P. J. Reynolds, D. M. Ceperley, B. J. Alder, and W. A. Lester. *J. Chem. Phys.*, 77:5593, 1982.
- [102] R. C. Grimm and R. G. Storer. *J. Comp. Phys.*, 7:134, 1971.
- [103] M. H. Kalos, D. Levesque, and L. Verlet. *Phys. Rev. A*, 9:2178, 1974.
- [104] G. Ortiz, D. M. Ceperley, and R. Martin. *Phys. Rev. Lett.*, 71:2777, 1993.
- [105] C. J. Umrigar, M. P. Nightingale, and K. J. Runge. *J. Chem. Phys.*, 99:2865, 1993.
- [106] D. M. Ceperley, M. H. Kalos, and J. L. Lebowitz. *Macromolecules*, 14:1472, 1981.
- [107] G. D. Mahan. *Many-particle physics*. Plenum Press, New York, 1990.
- [108] S. Datta. *Electronic transport in mesoscopic systems*. Cambridge University Press, Cambridge, 1995.
- [109] L. P. Kadanoff and G. Baym. *Quantum statistical mechanics: Green's function methods in equilibrium and nonequilibrium problems*. Benjamin, New York, 1962.
- [110] C.W.J. Beenakker. *Phys. Rev. B*, 44:1646, 1991.
- [111] V. Fock. *Z. Phys.*, 47:446, 1928.

- [112] C. G. Darwin. *Proc. Cambridge Philos. Soc.*, 27:86, 1930.
- [113] L. Martin-Moreno, J.J. Palacios, J. H. Oaknin, and C. Tejedor. *Physica B*, 212:224, 1995.
- [114] K.H. Ahn, J.H. Oh, and K.J. Chang. *Phys. Rev. B*, 52:13757, 1995.
- [115] M. Ferconi and G. Vignale. *Phys. Rev. B*, 56:12108, 1997.
- [116] E. Goldmann and S. R. Renn. *Phys. Rev. B*, 60:16611, 1999.
- [117] H. L. Chiueh and D. S. Chuu. *Phys. Rev. B*, 60:15919, 1999.
- [118] A.D. Guclu and Hong Guo. *Unpublished*.
- [119] D. Weinmann, W. Haussler, and B. Kramer. *Phys. Rev. Lett.*, 74:984, 1995.
- [120] J.T. Nicholls, J.E.F. Frost, M. Pepper, D.A. Ritchie, M.P. Grimshaw, and G.A.C. Jones. *Phys. Rev. B*, 48:8866, 1993.
- [121] K.A. Matveev, L.I. Glazman, and H.U. Baranger. *Phys. Rev. B*, 54:5637, 1996.
- [122] T.H. Oosterkamp, S.F. Godijn, M.J. Uilenreef, Y.V. Nazarov, N.C. van der Vaart, and L.P. Kouvenhoven. *Phys. Rev. Lett.*, 80:4951, 1998.
- [123] C. Gould, P. Hawrylak, A.S. Sachrajda, Y. Feng, and Z. Wasilewski. *Physica B*, 141:256, 1998.
- [124] C. Gould, P. Hawrylak, A.S. Sachrajda, Y. Feng, P. Zawadzki, and Z. Wasilewski. *Physica E*, 6:461, 2000.
- [125] M. Pi, M. Barranco, f. Garcias, S. Tarucha, and D.G. Austing. *Phys. Rev. Lett.*, 87:66801, 2001.
- [126] P. Matagne, J.P. Leburton, D.G. Austin, and S. Tarucha. *Phys. Rev. B*, 65:85325, 2002.
- [127] J. Kondo. *Prog. Theor. Phys.*, 32:37, 1964.

- [128] T.K. Ng and P.A. Lee. *Phys. Rev. Lett.*, 61:1768, 1988.
- [129] L.I. Glazman and M.E. Raikh. *JETP Lett.*, 47:452, 1988.
- [130] R. Aguado and D.C. Langreth. *Phys. Rev. Lett.*, 85:1946, 2000.
- [131] K. Kang, S.Y. Cho, J.-J. Kim, and S.-C. Shin. *Phys. Rev. B*, 63:113304, 2001.
- [132] T.-S. Kim and S. Hershfield. *Phys. Rev. B*, 63:245326, 2001.

